UR-1282
ER-40685-732

Tests of Models for e^+e^- Annihilation into Hadrons and Leptons

by

Tetsuro Kumita

UNIVERSITY OF ROCHESTER

October 1992

DEPARTMENT OF PHYSICS AND ASTRONOMY

ROCHESTER, NEW YORK 14627

UR-1282
ER-40685-

Tests of Models for e^+e^- Annihilation into Hadrons and Leptons

by

Tetsuro Kumita

Submitted in Partial Fulfillment
of the
Requirements for the Degree

DOCTOR OF PHILOSOPHY

Supervised by Professor A. Bodek

Department of Physics and Astronomy
College of Arts and Science

University of Rochester
Rochester, New York

1992

Curriculum Vitae

The author was born in Tokyo, Japan. He spent his undergraduate study at the Physics Department of Tokyo Institute of Technology. He studied theoretical particle physics under the guidance of Prof. C. Iso and received a B.S. in March, 1987. His B.S. thesis was on the phenomenology of the Higgs boson. He then entered the Department of Physics and Astronomy of the University of Rochester, where he worked on the AMY experiment at the TRISTAN accelerator at KEK. His thesis adviser has been Prof. A. Bodek.

Acknowledgements

My thesis could not have been finished without the excellent work of all members of the AMY collaboration, and the TRISTAN and KEK staffs.

I would like to thank Prof. A. Bodek, my thesis adviser, for providing an opportunity to work on this experiment and guiding me.

I wish to express my deepest thank to Prof. T. Nozaki, who has been advising me during my stay at KEK.

I especially thank H. Sagawa and T. Mori, who prepared the nice procedure of hadronic event analysis. Their previous studies were always my guide lines.

I am quite thankful to S. Lusin for providing me the results of di-lepton analysis. The di-lepton analysis in this thesis is his work.

I thank J. Fujimoto for the discussions and information on radiative corrections.

I thank K. Maeshima for the information of Z' analysis at the CDF.

I especially thank the members of the CDC sub-group, K. Ueno, Young-kee, Dimitris, and Yuekuan. I enjoyed working with them.

I thank Xiao-chen Fan, who helped the most boring part of my analysis, scanning hadronic events.

I would like to thank all of the Oho-hall gang. I could relax and enjoy in the friendly atmosphere. The Oho office was like my living room. Sorry, guys. You are too many to list up here.

I also wish to thank secretaries of Rochester and KEK, Betty, Connie, Judy, Kusama-san, and Nasu-san. I always troubled them with my laziness.

I am especially grateful to Prof. S.L. Olsen, Prof. K. Abe, and Prof. A. Maki for providing an exciting environment for research.

Finally, I would like to thank my parents. They have always accepted my decisions and encouraged me.

Abstract

We report on tests of various gauge group models using data observed by the AMY detector at the TRISTAN e^+e^- collider. We present results of total hadronic cross section for $e^+e^- \rightarrow hadrons$ at 50 GeV $\leq \sqrt{s} \leq$ 64 GeV for an integrated luminosity of $\int Ldt = 95.5pb^{-1}$, and total cross sections and forward-backward asymmetries for $e^+e^- \rightarrow \mu^+\mu^-$ and $e^+e^- \rightarrow \tau^+\tau^-$ processes at 52 GeV $\leq \sqrt{s} \leq$ 61.4 GeV for $\int Ldt = 32.6pb^{-1}$.

We examine models of extra Z bosons, E_6, $SU(5)_c$, and $SU(2)_q \times SU(2)_l$ by fitting to these data and data from other e^+e^- experiments together.

We determined the QCD scale parameter by fitting the total hadronic cross sections for all e^+e^- data at $20 \leq \sqrt{s} \leq 64$ GeV to the formula to $O(\alpha_s^3)$ and obtained $\Lambda_{\overline{MS}}^{(5)} = 0.533^{+0.521+0.020}_{-0.334-0.029} \pm 0.09$ GeV. This result is high but consistent with the world average of $\Lambda_{\overline{MS}}^{(5)} = 0.175^{+0.041}_{-0.034}$ within errors.

Contents

Chapter 1 Introduction 1

Chapter 2 Theories of Gauge Bosons 3

2.1 Gauge Bosons in Glashow-Salam-Weinberg Model . . . 3
2.2 Cross Section Formulae in the Standard Model . . . 8
2.2.1 Di-lepton Cross Section . . . 8
2.2.2 Hadronic Cross Section . . . 10
2.3 Extra Z Bosons . . . 14
2.3.1 Cross Section Formulae . . . 14
2.3.2 E_6 model . . . 16
2.3.3 $SU(5)_c$ color model . . . 20
2.3.4 $SU(2)_q \times SU(2)_l \times U(1)_Y$ model . . . 21

Chapter 3 The Experimental Apparatus 23

3.1 The TRISTAN collider . . . 23
3.2 The AMY Detector . . . 25
3.2.1 The Charged Particle Tracking System . . . 28
3.2.2 The X-ray Detector . . . 33
3.2.3 The Electromagnetic Shower Counter . . . 33
3.2.4 The Superconducting Magnet . . . 35
3.2.5 The Muon Identification System . . . 35
3.2.6 The Endcap Detectors in AMY 1.0 . . . 36
3.2.7 The Endcap Detectors in AMY 1.5 . . . 36
3.2.8 Triggering . . . 37
3.2.9 Data Acquisition . . . 38

Chapter 4 Total Hadronic Cross Section 40

4.1 Luminosity Measurement . . . 40
4.2 Hadronic Event Selection . . . 42
4.2.1 Triggering . . . 42
4.2.2 Filter . . . 43
4.2.3 Track reconstruction . . . 45
4.2.4 Final Selection . . . 46
4.3 Background Estimates . . . 49
4.4 Detection Efficiency . . . 55
4.5 Radiative Corrections . . . 57
4.6 Systematic Errors . . . 68
4.7 Results . . . 68

Chapter 5 The Di-lepton Cross Section 74

5.1 The Di-muon Event Selection . . . 74
5.2 Di-muon Cross Section . . . 76
5.3 τ Decay Modes . . . 77
5.4 $\tau^+\tau^-$ Event Selection . . . 80
5.5 $\tau^+\tau^-$ Cross Section . . . 82
5.6 Results . . . 83

Chapter 6 Mass of the Extra Z Bosons 88

6.1 The Fitting Procedure . . . 88
6.2 Constraints from Other Experiments . . . 90
6.3 Results and Discussions . . . 91

Chapter 7 Determination of the QCD Coupling Strength 100

7.1 Parameterization of α_s . . . 100
7.2 Results and Discussions . . . 101

Chapter 8 Summary 106

Bibliography 108

Appendix A Summary of Data Used in the Fits 114

Appendix B List of the AMY Collaborators 128

List of Tables

2.1 Fermions in the **27** representations of E_6. 18
2.2 The extra hyper charge $Y'(\alpha)$ in E_6 model. 19
2.3 The vector and the axial coupling in E_6 model. 19
2.4 Quantum numbers in $SU(5)_c$ model. 21

4.1 A summary of the integrated luminosities measured with the PTC (AMY 1.0), ESC (AMY 1.5), and SHC. 41
4.2 A summary of the hadronic event trigger inefficiencies. 44
4.3 A summary of the calculations of $\epsilon(1+\delta)$ in three different ways. ZSHAPE is used with $O(\alpha^3)$ corrections. 67
4.4 A summary of the overall normalization systematic errors. 69
4.5 A summary of the point-to-point systematic errors. 70
4.6 A summary of R values. 72

5.1 The world average of τ branching ratio. Here, h is a charged hadron and N is a neutral particle. 79
5.2 The background rate for each source. 82
5.3 A summary of $R_{\mu\mu}$, $A_{\mu\mu}$, $R_{\tau\tau}$, and $A_{\tau\tau}$. Errors listed are the statistical (first) and the systematic (second). 85

6.1 Mass limits of extra Z bosons from other experiments. 94
6.2 Results of the fits. θ' is set to be 0 for the E_6 and $SU(2)_q \times SU(2)_l$ models. The quoted errors correspond to $\Delta\chi^2 = 1.0$. 95
6.3 Results of the fits. θ' is allowed to vary under the constraints of the standard model parameters. 95

A.1 Summary of the R_{hadron} data from AMY. 115

A.2 Summary of the R_{hadron} data from TOPAZ and VENUS. Data are adjusted for the radiative corrections. 116
A.3 Summary of the R_{hadron} data from PEP and PETRA (continued to the next page). 117
A.3 (continuing from the previous page) 118
A.4 Summary of the $R_{\mu\mu}$ data from TRISTAN. 119
A.5 Summary of the $R_{\mu\mu}$ data from PEP and PETRA (continued to the next page). 120
A.5 (continuing from the previous page) 121
A.6 Summary of the $R_{\tau\tau}$ data from TRISTAN. 122
A.7 Summary of the $R_{\tau\tau}$ data from PEP and PETRA. 123
A.8 Summary of the $A_{\mu\mu}$ data from TRISTAN. 124
A.9 Summary of the $A_{\mu\mu}$ data from PEP and PETRA. 125
A.10 Summary of the $A_{\tau\tau}$ data from TRISTAN. 126
A.11 Summary of the $A_{\tau\tau}$ data from PEP and PETRA. 127

List of Figures

2.1 The Interaction between current J_Y^μ and a gauge boson B_μ. 5
2.2 The lowest order diagrams for $e^+e^- \to l^+l^-$ processes. 9
2.3 Diagrams of multi-hadronic annihilations. (a) QED process; (b) with QCD corrections; (c) Weak interaction. 12

3.1 An overview of the TRISTAN collider at KEK. 24
3.2 A schematic view of the AMY 1.0 detector. 26
3.3 A schematic view of the AMY 1.5 detector. 27
3.4 Cross-sectional views of the ITC. 30
3.5 Overviews of the CDC. 31
3.6 Track residuals measured in the CDC. 32
3.7 An overview and the layer structure of the SHC. 34
3.8 A schematic diagram of AMY 1.5 data acquisition system. 39

4.1 A typical hadronic event observed by the AMY detector. 47
4.2 Diagrams for two-photon hadron production processes (a) QPM, (b) VMD, and examples of (c) 3-jet and (d) 4-jet multi-jet. 50
4.3 Distributions of the event cut variables: (a) N_{CDC}; (b) E_{SHC}; (c) E_{vis}/E_{CM}; and (d) $\sum P_z/E_{vis}$. Both the real data (points) and the LUND 7.3 MC data (histograms) are selected with all other cuts except the ones for the distributions. 51
4.4 A beam-wall event rejected by the scan. 52
4.5 A radiative Bhabha event rejected by the scan. 53
4.6 A cosmic ray event rejected by the scan. 54

4.7 Diagrams of (a) initial state radiation, (b) final state radiation, (c) initial state QED vertex corrections, (d) final state QED vertex corrections, (e) QED vacuum polarization, and (f) QED box diagrams. (continued to the next page) 59
4.7 (continuing from the previous page) Diagrams of (g) weak box diagrams, (h) electroweak vacuum polarization, (i) electroweak vertex corrections, and (j) higher order QED initial state corrections. . . . 60
4.8 Radiative correction factors for $k_{max} = 0.99$, calculated by BKJ (short-dashed line with $M_{Z^0} = 91.16$ GeV and $M_t = 150$ GeV, long-dashed line with $M_{Z^0} = 92$ GeV and $M_t = 45$ GeV); FS (solid line); and ZSHAPE (dot-dashed line for $O(\alpha^3)$, dotted line for higher order corrections and exponentiatons). 63
4.9 Detection efficiencies ($\epsilon_{det} \times \epsilon_{sel}$) as a function of k, the energy of the initial state radiative photon normalized to the beam energy, estimated with LUND 7.3 at $E_{CM} = 58$ GeV. 65
4.10 The differential radiative correction factors as a function of k, calculated by ZSHAPE with $O(\alpha^3)$ corrections. 66
4.11 The AMY results for R values (solid circles) together with previously reported results at lower energies. 73

5.1 The differential cross section for $e^+e^- \to \mu^+\mu^-$ process. Data for all energies are combined. 78
5.2 A Feynman diagram of τ lepton decays. 79
5.3 The differential cross section for $e^+e^- \to \tau^+\tau^-$ process. Data for all energies are combined. 84
5.4 The results of $R_{\mu\mu}$ and $R_{\tau\tau}$. 86
5.5 The results of $A_{\mu\mu}$ and $A_{\tau\tau}$. 87

6.1 Mass limits for four E_6 models, Z_ψ, Z_χ, Z_η, and Z_{LR}(not discussed in this thesis) from the direct production at CDF (95% CL), taken from Ref. [55]. 92
6.2 Cross sections for $p\bar{p} \to Z' \to e^+e^-$ at $\sqrt{s} = 1.8$ TeV in $SU(2)_q \times SU(2)_l$ model, taken from Ref. [61]. 93
6.3 The region of $\sin\phi$ -$M_{Z'}$ in the $SU(2)_q \times SU(2)_l$ model excluded (95% CL). 93

6.4 68% CL contour in the $\sin\phi$ -$M_{Z'}$ plain for the $SU(2)_q \times SU(2)_l$ model ($\Delta\chi^2 = 2.3$). 96
6.5 R_{hadron} with the theoretical predictions of the standard model (solid line) and the E_6 model with Z_η boson (dot-dashed line) for $M_{Z'} =$ 162 GeV, $\theta' = 0$. 97
6.6 $R_{\mu\mu}$ and $R_{\tau\tau}$ with the theoretical predictions of the standard model (solid line) and the E_6 model with Z_η boson (dot-dashed line) for $M_{Z'} = 162$ GeV, $\theta' = 0$. 98
6.7 $A_{\mu\mu}$ and $A_{\tau\tau}$ with the theoretical predictions of the standard model (solid line) and the E_6 model with Z_η boson (dot-dashed line) for $M_{Z'} = 162$ GeV, $\theta' = 0$. 99

7.1 Experimental R values together with the standard model predictions for $M_Z = 91.173$ GeV, $\sin^2\theta_W = 0.2259$, and $\Lambda^{(5)}_{\overline{MS}} = 0.175$ GeV (solid curve) or $\Lambda^{(5)}_{\overline{MS}} = 0.533$ GeV (dot-dashed curve). 104
7.2 Summary of measurements of $\alpha_s(M_Z)$. The dashed line indicates the world average value $\alpha_s(M_Z) = 0.1134$. 105

Chapter 1

Introduction

The standard model of particle physics, Glashow-Salam-Weinberg (GSW) model of electroweak interaction and quantum chromodynamics (QCD), the theory of the strong interaction, successfully describes all experimental data currently available. The fundamental of the standard model is that is described as the gauge group theory of $SU(3)_c \times SU(2)_L \times U(1)_Y$.

A number of gauge group theories, based on larger gauge groups which break into $SU(3)_c \times SU(2)_L \times U(1)_Y$, have also been proposed. These theories are associated with one or more additional neutral gauge boson(s) (extra Z bosons or Z''s), closely reproduce the standard model at low energy, but show deviations at high energy comparable with the mass of the extra Z bosons.

In this thesis, the standard model and several gauge group models with extra Z bosons are examined using data of $e^+e^- \to hadrons$, $e^+e^- \to \mu^+\mu^-$, and $e^+e^- \to \tau^+\tau^-$ processes observed by the AMY detector at the TRISTAN e^+e^- collider. The structure of this thesis is as follows:

In Chapt. 2, the GSW model and gauge group theories with extra Z bosons are reviewed. Theoretical formulae which will be compared with experimental data are also presented.

In Chapt. 3, the experimental apparatus, *i.e.*, the AMY detector and the TRISTAN collider are described.

In Chapt. 4, the procedure of hadronic event selection and the determination of the total hadronic cross section are explained.

In Chapt. 5, the procedure of di-lepton ($\mu^+\mu^-$ and $\tau^+\tau^-$) event selections is presented. The extraction of total cross sections and forward-backward asymmetries for these processes are described.

In Chapt. 6, Our experimental data and data of other experiments are compared to the predictions of models with extra Z bosons.

In Chapt. 7, the data for the total hadronic cross sections are fitted to extract the QCD coupling constant within the framework of the standard model.

In Chapt. 8, the analysis and conclusions are summarized.

Chapter 2

Theories of Gauge Bosons

2.1 Gauge Bosons in Glashow-Salam-Weinberg Model

In the quantum field theory of the particle physics, interactions are described in terms of exchanges of bosons, such as photon for the electromagnetic interaction, $W^{\pm}$and Z^0 for the weak interaction, gluon for the strong interaction, and graviton for the gravitational interaction. These bosons are called "Gauge Bosons" since they are essential for the gauge invariance of the theory. In this section, the gauge bosons in the Glashow-Salam-Weinberg model (GSW model) [1], the unified theory of the electromagnetic and the weak interactions, are discussed.

The gauge bosons in the GSW model are necessary so that the Lagrangian will be invariant under local weak hypercharge $U(1)_Y$ and weak isospin $SU(2)_L$ transformations. Here the "Y" in $U(1)_Y$ denotes the hypercharge and the "L" in $SU(2)_L$ denotes left-handed since $SU(2)$ transformations only apply to the left-handed states. The left-handed fermions form isospin doublets while right-handed fermions form isospin singlets. Namely, for leptons:

$$\begin{aligned} \psi_L &= \begin{pmatrix} \nu_e \\ e^- \end{pmatrix}_L \qquad & I = \frac{1}{2},\ \ Y = -1 \\ \psi_R &= e_R^- & I = 0,\ \ Y = -2 \end{aligned} \tag{2.1}$$

and for quarks:

$$\begin{aligned} \psi_L &= \begin{pmatrix} u \\ d \end{pmatrix}_L \qquad & I = \frac{1}{2},\ \ Y = \frac{1}{3} \\ \psi_R &= u_R & I = 0,\ \ Y = \frac{4}{3} \\ \psi_R &= d_R & I = 0,\ \ Y = -\frac{2}{3}\,. \end{aligned} \tag{2.2}$$

Here I is magnitude of the isospin and Y is the hypercharge. Only the first of the three generations of leptons and quarks is shown in eqs. (2.1) and (2.2). The third component of the isospin, I_3 and the hypercharge Y are related to the electric charge Q by the Gell-Mann-Nishijima formula [2]

$$Q = I_3 + \frac{Y}{2}\ , \tag{2.3}$$

where Q is in units of the positron charge.

We first discuss the $U(1)_Y$ invariance. The Lagrangian for a free fermion is written as

$$\mathcal{L}_{free} = \bar{\psi}(i\gamma^\mu\partial_\mu - m)\psi\ , \tag{2.4}$$

where ψ is assumed to be a Dirac field and m its mass. We require the Lagrangian to be invariant under a local gauge transformation

$$\begin{aligned} \psi(x) &\rightarrow e^{i\alpha(x)\cdot\frac{Y}{2}}\psi(x) \\ \bar{\psi}(x) &\rightarrow \bar{\psi}(x)e^{-i\alpha(x)\cdot\frac{Y}{2}} \end{aligned} \tag{2.5}$$

where $\alpha(x)$ is an arbitrary number with an arbitrary dependence on space-time coordinates. The set of phase transformations $e^{i\alpha(x)\cdot\frac{Y}{2}}$ defines the $U(1)_Y$ group and $Y/2$ is its generator. To modify the Lagrangian (2.4) to be invariant under (2.5), we need to introduce a gauge covariant derivative D_μ instead of the ordinary derivative ∂_μ. The transformation on the covariant derivative has to be

$$D_\mu\psi(x) \rightarrow e^{i\alpha(x)\cdot\frac{Y}{2}}D_\mu\psi(x)$$

in order to maintain local gauge invariance. By introducing a new vector field B_μ, which we assume to transform as

$$B_\mu(x) \rightarrow B_\mu(x) - \frac{1}{g'}\partial_\mu\alpha(x)\ , \tag{2.6}$$

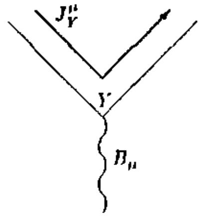

Figure 2.1: The Interaction between current J_Y^μ and a gauge boson B_μ.

we can define such a covariant derivative to be

$$D_\mu \equiv \partial_\mu + ig'\frac{Y}{2}B_\mu \ . \tag{2.7}$$

Thus, the local gauge invariant Lagrangian can be written as

$$\begin{aligned} \mathcal{L} &= \bar{\psi}(i\gamma^\mu D_\mu - m)\psi \\ &= \bar{\psi}(i\gamma^\mu\partial_\mu - m)\psi - g'\bar{\psi}\gamma^\mu\frac{Y}{2}\psi B_\mu \ . \end{aligned} \tag{2.8}$$

The vector field B_μ, which is introduced to satisfy the local gauge invariance, is a "Gauge Boson". The second term of the Lagrangian (2.8),

$$\begin{aligned} \mathcal{L}_{int} &= -g'\bar{\psi}\gamma^\mu\frac{Y}{2}\psi B_\mu \\ &\equiv -g' J_Y^\mu B_\mu \end{aligned} \tag{2.9}$$

describes the interaction between the weak hypercharge current J_Y^μ and the gauge boson B_μ as shown in Fig. 2.1. Here g' is the coupling constant or the strength of this interaction.

Next, let us consider the local $SU(2)_L$ gauge transformation of the form

$$\psi_L(x) \to \exp(i\sum_{k=1}^{3}\alpha_k(x)T_k)\psi_L(x) \equiv e^{i\boldsymbol{\alpha}(x)\cdot\boldsymbol{T}}\psi_L(x) \ , \tag{2.10}$$

where $\alpha_k(x)$'s are, as before, arbitrary parameters and T_k's are the generators of $SU(2)_L$. Here, ψ_L is the left-handed fermion which is an isospin doublet as

shown in (2.1) and (2.2). In this representation, we can express the $SU(2)$ isospin generators by the Pauli matrices

$$\boldsymbol{T} = \frac{1}{2}\boldsymbol{\sigma}$$

$$\sigma_1 = \begin{pmatrix} 0 & 1 \\ 1 & 0 \end{pmatrix}, \quad \sigma_2 = \begin{pmatrix} 0 & -i \\ i & 0 \end{pmatrix}, \quad \sigma_3 = \begin{pmatrix} 1 & 0 \\ 0 & -1 \end{pmatrix} . \tag{2.11}$$

The Lagrangian for a left-handed free fermion is

$$\mathcal{L}_{free} = \bar{\psi}_L(i\gamma^\mu\partial_\mu)\psi_L \ , \tag{2.12}$$

where the mass term $m\bar{\psi}_L\psi_L$ does not exist since the spinor combination $\bar{\psi}_L\psi_L$ is identically zero. Fermions get masses through interactions with the Higgs boson when symmetry is spontaneously broken. We need to introduce a covariant derivative

$$D_\mu \equiv \partial_\mu + ig\boldsymbol{T}\cdot\boldsymbol{W}_\mu \tag{2.13}$$

to modify the Lagrangian to be invariant under local $SU(2)_L$ transformations. Here three new gauge bosons W_μ^k ($k = 1,2,3$) appear. By following the argument for the $U(1)_Y$ case, we obtain the Lagrangian for the interaction between the fermion and the W bosons

$$\mathcal{L}_{int} = -g\bar{\psi}_L\gamma^\mu\boldsymbol{T}\cdot\boldsymbol{W}_\mu\psi_L \tag{2.14}$$

where g is the coupling constant of the $SU(2)_L$ gauge interaction. For the first generation leptons, $\bar{\psi}_L = (\bar{\nu}_L, \bar{e}_L)$, we can rewrite the interaction Lagrangian as

$$\begin{aligned} \mathcal{L}_{int} &= -\frac{g}{\sqrt{2}}\bar{\nu}_L\gamma^\mu e_L W_\mu^+ - \frac{g}{\sqrt{2}}\bar{e}_L\gamma^\mu\nu_L W_\mu^- \\ &\quad -\frac{g}{2}\bar{\nu}_L\gamma^\mu\nu_L W_\mu^3 + \frac{g}{2}\bar{e}_L\gamma^\mu e_L W_\mu^3 \ , \end{aligned} \tag{2.15}$$

where $W_\mu^\pm = \frac{1}{\sqrt{2}}(W_\mu^1 \mp iW_\mu^2)$. We identify these $W_\mu^\pm$ as the physical charged weak bosons. The physical neutral gauge bosons, A_μ of the electromagnetic interaction and Z_μ^0 of the weak interaction, can be expressed as linear combinations of B_μ and W_μ^3 as follows:

$$A_\mu = B_\mu\cos\theta_W + W_\mu^3\sin\theta_W \tag{2.16}$$

$$Z_\mu = -B_\mu\sin\theta_W + W_\mu^3\cos\theta_W \ , \tag{2.17}$$

where the mixing angle, θ_W, is called the "Weinberg angle".

Thus, the Lagrangian for the interactions due to the neutral gauge bosons (the neutral current Lagrangian) can be written as

$$\mathcal{L}_{NC} = -g'\bar{\psi}\gamma^\mu \frac{Y}{2}\psi B_\mu - g\bar{\psi}\gamma^\mu I_3\psi W^3_\mu \quad (2.18)$$

$$= -\bar{\psi}\gamma^\mu(g'\frac{Y}{2}\cos\theta_W + gI_3\sin\theta_W)\psi A_\mu$$
$$-\bar{\psi}\gamma^\mu(-g'\frac{Y}{2}\sin\theta_W + gI_3\cos\theta_W)\psi Z_\mu . \quad (2.19)$$

The first term of (2.19) has to be identical to the electromagnetic interaction of Quantum Electrodynamics (QED)

$$\mathcal{L}_{EM} = -eJ^\mu_{EM}A_\mu \equiv -e\bar{\psi}\gamma^\mu Q\psi A_\mu . \quad (2.20)$$

By using eq. (2.3), we obtain, therefore,

$$g\sin\theta_W = g'\cos\theta_W = e . \quad (2.21)$$

We can rewrite the neutral current Lagrangian as

$$\mathcal{L}_{NC} = -e\bar{\psi}\gamma^\mu Q\psi A_\mu - \frac{e}{\sin\theta_W\cos\theta_W}\bar{\psi}\gamma^\mu(I_3 - Q\sin^2\theta_W)\psi Z_\mu . \quad (2.22)$$

It is convenient to introduce a Dirac field for each flavor:

$$\Psi = \nu_L,\ e^-_L + e^-_R,\ u_L + u_R,\ \text{or}\ d_L + d_R\ .$$

Then the neutral current Lagrangian becomes

$$\mathcal{L}_{NC} = -e\bar{\Psi}\gamma^\mu Q\Psi A_\mu - \frac{e}{\sin\theta_W\cos\theta_W}\bar{\Psi}\gamma^\mu\frac{1}{2}(g_V - g_A\gamma_5)\Psi Z_\mu$$
$$\equiv -eJ^\mu_{EM}A_\mu - \frac{e}{\sin\theta_W\cos\theta_W}J^\mu_Z Z_\mu \quad (2.23)$$

with the vector coupling constant, g_V, and the axial coupling constant, g_A, given by:

$$g_V \equiv I^L_3 - 2Q\sin^2\theta_W$$
$$g_A \equiv I^L_3 , \quad (2.24)$$

where I^L_3 denotes the third component of the isospin for the left-handed state.

2.2 Cross Section Formulae in the Standard Model

The GSW model of the weak and electromagnetic interactions (electro-weak interaction for short) together with Quantum Chromodynamics (QCD) which describes the strong interaction, corresponding to $SU(3)$ color symmetry, is called the standard model. Therefore, the gauge group of the standard model is $SU(3)_c \times SU(2)_L \times U(1)_Y$, where the "c" in $SU(3)_c$ stands for color symmetry.

In the following section, the theoretical expressions for the cross sections for the processes, e^+e^- to di-leptons and e^+e^- to hadrons, are described.

2.2.1 Di-lepton Cross Section

Di-lepton reactions are processes such as $e^+e^- \to l^+l^-$ ($l = \mu$ or τ). The lowest order diagrams for these processes are shown in Fig. 2.2. If we neglect the contribution of the weak interaction (Fig. 2.2 (b)), the differential cross section at center-of-mass energy $\sqrt{s}$ is calculated in QED to be

$$\frac{d\sigma}{d\Omega} = \frac{\alpha^2}{4s}(1 + \cos^2\theta) \quad (2.25)$$

where $\alpha \equiv e^2/4\pi\hbar c$ is the fine structure constant and θ is the angle between directions of the e^- beam and the outgoing l^-. By integrating eq. (2.25) over θ and ϕ (the azimuthal angle about the beam direction) we obtain the total QED cross section

$$\sigma_0 = \frac{4\pi\alpha^2}{3s} . \quad (2.26)$$

In the TRISTAN energy range, 50 GeV $\leq \sqrt{s} \leq$ 64 GeV, the effect of the weak neutral currents can not be neglected. The standard model prediction of the differential cross section is

$$\frac{d\sigma}{d\Omega} = \frac{\alpha^2}{4s}\Big[\Big\{1 + 8g^e_V g^l_V Re(\chi) + 16\big((g^e_V)^2 + (g^e_A)^2\big)\big((g^l_V)^2 + (g^l_A)^2\big)|\chi|^2\Big\}(1 + \cos^2\theta)$$
$$+ (16g^e_A g^l_A Re(\chi) + 128 g^e_V g^e_A g^l_V g^l_A|\chi|^2)\cos\theta\Big] \quad (2.27)$$

where

$$\chi = \frac{1}{16\sin^2\theta_W\cos^2\theta_W}\frac{s}{s - M_Z^2 + iM_Z\Gamma_Z} . \quad (2.28)$$

Here g^f_V and g^f_A ($f = e, l$) are the vector- and the axial-coupling constants for the fermion f. The quantities M_Z and Γ_Z are the mass and the decay width of

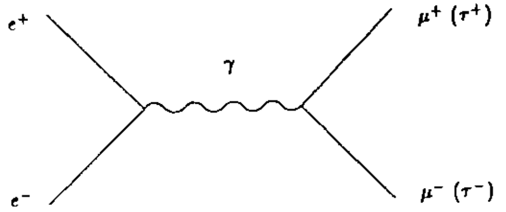

(a)

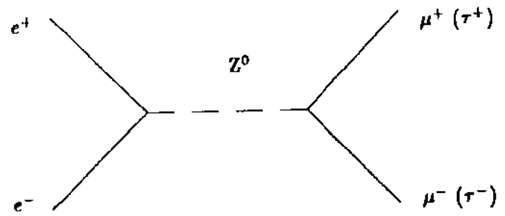

(b)

Figure 2.2: The lowest order diagrams for $e^+e^- \to l^+l^-$ processes.

Z^0 boson. In eq. (2.27), a term proportional to $\cos\theta$ appears from the interference between the QED and the weak interaction channels. It results in a forward-backward asymmetry, *i.e.*, l^-'s are populated at the forward region ($\theta < \pi/2$) differently from at the backward region ($\theta > \pi/2$). We define the forward-backward asymmetry A_{ll} for the l^+l^- process ($l = \mu$ or τ) as

$$A_{ll} \equiv \frac{\sigma_F - \sigma_B}{\sigma_F + \sigma_B} \tag{2.29}$$

where

$$\sigma_F = \int_{\theta=0}^{\theta=\pi/2}\int_{\phi=0}^{\phi=2\pi}\frac{d\sigma}{d\Omega}d\Omega, \quad \sigma_B = \int_{\theta=\pi/2}^{\theta=\pi}\int_{\phi=0}^{\phi=2\pi}\frac{d\sigma}{d\Omega}d\Omega \ ,$$

and the R value (R_{ll}), the total cross section normalized to σ_0, the theoretical dilepton QED cross section (given by eq. (2.26)), as

$$R_{ll} \equiv \frac{\sigma}{\sigma_0} \ . \tag{2.30}$$

Then the differential cross section can then be written as

$$\frac{d\sigma}{d\Omega} = \frac{\alpha^2}{4s}R_{ll}(1 + \cos^2\theta + \frac{8}{3}A_{ll}\cos\theta) \ . \tag{2.31}$$

By comparing eq. (2.31) to eq. (2.27), we obtain the standard model predictions for R_{ll} and A_{ll} to be:

$$R_{ll} = 1 + 8g_V^e g_V^l Re(\chi) + 16\Big((g_V^e)^2 + (g_A^e)^2\Big)\Big((g_V^l)^2 + (g_A^l)^2\Big)|\chi|^2 \tag{2.32}$$

and

$$A_{ll} = \Big[\ 6g_A^e g_A^l Re(\chi) + 48g_V^e g_A^e g_V^l g_A^l |\chi|^2\ \Big]\ /\ R_{ll}\ . \tag{2.33}$$

In the calculations above, the mass of the leptons was neglected, which is a good approximation at our energy range.

2.2.2 Hadronic Cross Section

Hadronic events are the reactions in which hadronic final states are produced. These processes are described by two steps as shown in Fig. 2.3. In the first step, a quark-antiquark pair (with gluons) is produced. In the second step, the partons are converted into hadrons. The second step proceeds at low momentum transfers, where perturbative QCD cannot be applied. Therefore, hadronization has to be described through phenomenological models. On the other hand, the total cross section for hadronic events is only dependent on the production of partons, which is quite well understood.

The total cross section for the production of hadronic events is also conventionally reported in terms of R value (R_{hadron}), the total hadronic cross section normalized to σ_0, the theoretical di-lepton QED cross section. In the QED diagram, shown in Fig. 2.3 (a), the difference between hadronic and di-lepton events is only the charge of quarks. Therefore, the R value is given as

$$R_{QED} = \frac{\sigma(e^+e^- \to q\bar{q})}{\sigma_0} = 3\sum_q Q_q^2 \tag{2.34}$$

where the summation is carried out over all quark flavors which can be pair-produced at the center-of-mass energy of the experiment (q=u,d,s,c,and b at TRISTAN). The factor of 3 originates from the 3 quark colors and Q_q's are the charge of the quark q in units of positron charge.

Hadronic final states are produced by not only $e^+e^- \to q\bar{q}$ process but also in $e^+e^- \to q\bar{q}g$ and other higher order QCD processes as shown in Fig. 2.3 (b). Their contributions can be calculated within perturbative QCD and the R value is modified to be

$$R_{QCD} = R_{QED}\Big[\,1 + C_1(\alpha_s/\pi) + C_2(\alpha_s/\pi)^2 + C_3(\alpha_s/\pi)^3 + O(\alpha_s^4)\,\Big] \tag{2.35}$$

to order $O(\alpha_s^3)$, where $\alpha_s \equiv \alpha_s(\sqrt{s})$ is the QCD coupling constant at the center-of-mass-energy $\sqrt{s}$. Here, the coefficients have been calculated in Ref. [3] for massless quarks and have the values:

$$\begin{aligned} C_1 &= 1 \\ C_2 &= 1.9857 - 0.1153N_f \\ C_3 &= -6.6368 - 1.2001N_f - 0.0052N_f^2 - 1.2395\frac{(\sum Q_q)^2}{3\sum Q_q^2} \end{aligned}$$

where N_f is the number of quark flavors. The third order coefficient was also calculated to be $C_3 = 70.985 - 1.200N_f - 0.005N_f^2 - 0.840(\sum Q_q)^2/2\sum Q_q^2$ in Ref. [4] and we have been using this value in our previous analyses [44]. However, it was found the calculation of Ref. [4] was uncorrect and the new calculation of

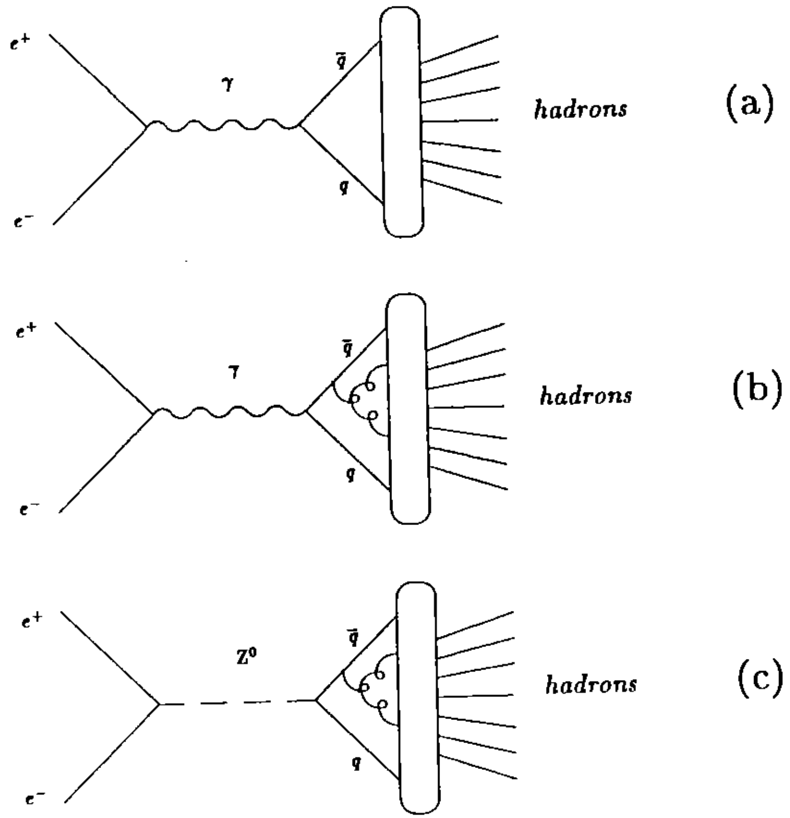

Figure 2.3: Diagrams of multi-hadronic annihilations. (a) QED process; (b) with QCD corrections; (c) Weak interaction.

Ref. [3] lowers the theoretical R values by about 0.4% at TRISTAN energies. The "running" strong coupling is given to $O(\alpha_s^2)$ by

$$\alpha_s(Q) = \frac{12\pi}{(33-2N_f)\ln(Q^2/\Lambda^2_{\overline{MS}}) + 6\frac{153-19N_f}{33-2N_f}\ln(\ln(Q^2/\Lambda^2_{\overline{MS}}))}, \qquad (2.36)$$

where Q is the four-momentum transfer. The quantity $\Lambda_{\overline{MS}}$ is the QCD scale parameter in the "modified minimal subtraction" scheme [5]. The $O(\alpha_s^3)$ formula and discussions on the QCD parameterizations appear in Chapt. 7.

Unlike in the di-lepton case, for hadronic events, the mass of heavier quarks is not negligible, when compared with the center-of-mass-energy. When one includes the effect of the weak interaction due to the Z^0 propagator (Fig. 2.3 (c)), QCD effect, and quark mass effect, the final formula for R_{hadron} as given in Ref. [6] is

$$R_{hadron} = 3\sum_q \left(\frac{1}{2}\beta_q(3-\beta_q^2)R^q_{VV}(1+C^V_{QCD}) + \beta_q^3 R^q_{AA}(1+C^A_{QCD})\right), \qquad (2.37)$$

where β_q is the quark velocity $\beta_q = \sqrt{1-4m_q^2/s}$. The contribution of the electroweak interaction is given in

$$\begin{aligned} R^q_{VV} &= Q_q^2 - 8Q_q g_V^e g_V^q Re(\chi) + 16\left((g_V^e)^2 + (g_A^e)^2\right)(g_V^q)^2|\chi|^2 \qquad (2.38)\\ R^q_{AA} &= 16\left((g_V^e)^2 + (g_A^e)^2\right)(g_A^q)^2|\chi|^2, \qquad (2.39)\end{aligned}$$

where g_V^q and g_A^q are the coupling constants for the quark q. The QCD correction

$$C^{V(A)}_{QCD} = C_1^{V(A)}(\alpha_s/\pi) + C_2^{V(A)}(\alpha_s/\pi)^2 + C_3^{V(A)}(\alpha_s/\pi)^3 \qquad (2.40)$$

is calculated including the quark mass effects in the $O(\alpha_s)$ in Ref. [7] as:

$$\begin{aligned} C_1^V &= \frac{4\pi}{3}\left(\frac{\pi}{2\beta_q} - \frac{3+\beta_q}{4}(\frac{\pi}{2} - \frac{3}{4\pi})\right),\\ C_1^A &= \frac{4\pi}{3}\left(\frac{\pi}{2\beta_q} - (\frac{19}{10} - \frac{22}{5}\beta_q + \frac{7}{2}\beta_q^2)(\frac{\pi}{2} - \frac{3}{4\pi})\right).\end{aligned}$$

We use the zero-quark-mass approximation

$$\begin{aligned} C_2^{V(A)} &= 1.9857 - 0.1153N_f,\\ C_3^{V(A)} &= -6.6368 - 1.2001N_f - 0.0052N_f^2 - 1.2395\frac{(\sum Q_q)^2}{3\sum Q_q^2}\end{aligned}$$

for the higher order corrections.

2.3 Extra Z Bosons

The predictions of the standard model are in excellent agreement with experimental data. However, there are some other gauge group theories that can closely reproduce the standard model predictions at low energy. In this section, three models that predict the existence of additional neutral gauge bosons (i.e., extra Z bosons or Z's) are discussed. If the mass of the Z' is heavier than the standard model Z^0, then only high energy hadron colliders such as the Tevatron can observe Z' by direct production. However, the effects of Z' can be seen at lower energy as deviations of the data from the standard model predictions. There has been several searches for Z's by comparing precise measurements of Z^0 parameters at LEP with low energy neutral current data. There are some range of parameters in these models where the peak of the Z^0 masks the effects of the Z' at LEP energies, while the deviations can still be seen at TRISTAN. In the following subsections, we discuss how the existence of Z's changes the cross section predictions at TRISTAN energies and review several Z' models.

2.3.1 Cross Section Formulae

In models with one extra Z boson, the neutral current Lagrangian in the standard model (2.23) is modified to be

$$\mathcal{L}_{NC} = -eJ^\mu_{EM}A_\mu - g_Z J_1^\mu Z_{0\mu} - g_{Z'}J_2^\mu Z'_{0\mu}, \qquad (2.41)$$

where A and Z_0 are the electromagnetic and Z^0 fields in the standard model, and Z'_0 is the extra Z field. The coupling constant g_Z and the current J_1 are

$$\begin{aligned} g_Z &= \frac{e}{\sin\theta_W\cos\theta_W}\\ J_1^\mu &= \bar{\Psi}\gamma^\mu\frac{1}{2}(g_{0V} - g_{0A}\gamma_5)\Psi,\end{aligned}$$

where g_{0V} and g_{0A} are the vector- and the axial-coupling constants in the standard model given as g_V and g_A in eq. (2.24). Similarly, we can write the extra weak neutral current J_2 as

$$J_2^\mu = \bar{\Psi}\gamma^\mu\frac{1}{2}(g'_{0V} - g'_{0A}\gamma_5)\Psi \qquad (2.42)$$

with the model dependent coupling constants g'_{0V} and g'_{0A}.

In the (Z_0, Z_0') representation basis, the Hermitian mass-squared matrix is

$$\mathcal{M}^2 = M_{Z_0}^2 \begin{pmatrix} 1 & b \\ b & a \end{pmatrix} , \tag{2.43}$$

where M_{Z_0}, the mass of the standard model Z^0 is related to the W boson mass and the Weinberg angle by

$$M_{Z_0} = M_W / \cos\theta_W \ . \tag{2.44}$$

The mass eigenstates of the neutral weak bosons are given by

$$\begin{aligned} Z &= Z_0 \cos\theta' + Z_0' \sin\theta' \\ Z' &= -Z_0 \sin\theta' + Z_0' \cos\theta' \end{aligned} \tag{2.45}$$

in terms of the current eigenstates Z_0 and Z_0' . The mass of the Z^0 which LEP experiments measure is the mass of Z above. The physical masses of the Z and Z' are expressed by diagonalizing the mass-squared matrix as

$$\begin{pmatrix} M_Z^2 & 0 \\ 0 & M_{Z'}^2 \end{pmatrix} = M_{Z_0}^2 \begin{pmatrix} \cos\theta' & \sin\theta' \\ -\sin\theta' & \cos\theta' \end{pmatrix} \begin{pmatrix} 1 & b \\ b & a \end{pmatrix} \begin{pmatrix} \cos\theta' & -\sin\theta' \\ \sin\theta' & \cos\theta' \end{pmatrix} . \tag{2.46}$$

The mixing angle between the Z_0 and Z_0' can be expressed in terms of M_{Z_0}, M_Z, and $M_{Z'}$ as

$$\tan^2\theta' = \frac{M_{Z_0}^2 - M_Z^2}{M_{Z'}^2 - M_{Z_0}^2} \ . \tag{2.47}$$

The existence of an extra Z boson modifies the standard model formula of R_{hadron}, given by eq. (2.37), to:

$$R_{hadron} = 3\sum_q \left(\frac{1}{2}\beta_q(3-\beta_q^2) R^q_{VV}(1 + C^V_{QCD}) + \beta_q^3 R^q_{AA}(1 + C^A_{QCD}) \right) , \tag{2.48}$$

where

$$\begin{aligned} R^q_{VV} = \ Q_q^2 \ & -8Q_q g_V^e g_V^q Re(\chi) + 16\left((g_V^e)^2 + (g_A^e)^2\right)(g_V^q)^2|\chi|^2 \\ & -8Q_q g_V^{\prime e} g_V^{\prime q} Re(\chi') + 16\left((g_V^{\prime e})^2 + (g_A^{\prime e})^2\right)(g_V^{\prime q})^2|\chi'|^2 \\ & +32(g_V^e g_V^{\prime e} + g_A^e g_A^{\prime e}) g_V^q g_V^{\prime q} Re(\chi\cdot\chi'^*) , \end{aligned} \tag{2.49}$$

$$\begin{aligned} R^q_{AA} = \ & 16\left((g_V^e)^2 + (g_A^e)^2\right)(g_A^q)^2|\chi|^2 + 16\left((g_V^{\prime e})^2 + (g_A^{\prime e})^2\right)(g_A^{\prime q})^2|\chi'|^2 \\ & +32(g_V^e g_V^{\prime e} + g_A^e g_A^{\prime e}) g_A^q g_A^{\prime q} Re(\chi\cdot\chi'^*) , \end{aligned} \tag{2.50}$$

and

$$\begin{aligned} \chi &= \frac{1}{16\sin^2\theta_W \cos^2\theta_W} \frac{s}{s - M_Z{}^2 + iM_Z\Gamma_Z} , \\ \chi' &= \frac{1}{16\sin^2\theta_W \cos^2\theta_W} \frac{s}{s - M_{Z'}{}^2 + iM_{Z'}\Gamma_{Z'}} . \end{aligned} \tag{2.51}$$

Here $g_{V(A)}$ and $g'_{V(A)}$ are the coupling constants to the mass eigen states, Z and Z', given by

$$\begin{aligned} g_{V(A)} &= g_{0V(A)} \cos\theta' + \lambda g'_{0V(A)} \sin\theta' \\ g'_{V(A)} &= -g_{0V(A)} \sin\theta' + \lambda g'_{0V(A)} \cos\theta' , \end{aligned} \tag{2.52}$$

where λ is the ratio of the Z_0' coupling to the Z^0 coupling, $\lambda \equiv g_{Z'}/g_Z$. The QCD correction factors C^V_{QCD} and C^A_{QCD} are same as which given in (2.40). $\Gamma_{Z'}$ in eq. (2.51) is the total decay width of Z'. We neglect this term in the following analysis because its effect is negligible unless center-of-mass energy is close to the Z' pole.

Similarly, the formulae for R_{ll} and A_{ll} given in eq. (2.32) and (2.33) in the standard model case are modified to be

$$\begin{aligned} R_{ll} = \ 1 \ & +8g_V^e g_V^l Re(\chi) + 16\left((g_V^e)^2 + (g_A^e)^2\right)\left((g_V^l)^2 + (g_A^l)^2\right)|\chi|^2 \\ & +8g_V^{\prime e} g_V^{\prime l} Re(\chi') + 16\left((g_V^{\prime e})^2 + (g_A^{\prime e})^2\right)\left((g_V^{\prime l})^2 + (g_A^{\prime l})^2\right)|\chi'|^2 \\ & +32(g_V^e g_V^{\prime e} + g_A^e g_A^{\prime e})(g_V^l g_V^{\prime l} + g_A^l g_A^{\prime l}) Re(\chi\cdot\chi'^*) , \end{aligned} \tag{2.53}$$

and

$$\begin{aligned} A_{ll} = \ & \Big[\ 6g_A^e g_A^l Re(\chi) + 48 g_V^e g_A^e g_V^l g_A^l |\chi|^2 \\ & + \ 6g_A^{\prime e} g_A^{\prime l} Re(\chi') + 48 g_V^{\prime e} g_A^{\prime e} g_V^{\prime l} g_A^{\prime l} |\chi'|^2 \\ & + \ 24(g_V^e g_A^{\prime e} + g_A^e g_V^{\prime e})(g_V^l g_A^{\prime l} + g_A^l g_V^{\prime l}) Re(\chi\cdot\chi'^*) \ \Big] \ / \ R_{ll} . \end{aligned} \tag{2.54}$$

2.3.2 E_6 model

The superstring theory [8] in ten dimensions is anomaly free only when the gauge group is $SO(32)$ or $E_8 \times E_8$. The group $E_8 \times E_8$ is more interesting because it allows for chiral fermions as in the standard model. The compactification of the additional six dimensions on a Calabi-Yau manifold [9] leads to E_6 as an "effective" group of the grand unified theory (GUT). In this subsection extra Z bosons in the superstring-inspired E_6 model are described [11].

E_6 is the next natural choice of anomaly-free GUT group after $SU(5)$ and $SO(10)$. In $SU(5)$ GUT, There are a total fifteen fermions in each generation as in the standard model and they are placed in the $\bar{\mathbf{5}}$ and $\mathbf{10}$ representations as

$$\bar{5} \;=\; (\mathbf{1},\mathbf{2})+(\bar{\mathbf{3}},\mathbf{1}) = \begin{pmatrix} \nu_e \\ e^- \end{pmatrix}_L + \bar{d}_L \qquad (2.55)$$

$$10 \;=\; (\mathbf{1},\mathbf{1})+(\bar{\mathbf{3}},\mathbf{1})+(\mathbf{3},\mathbf{2}) = e_L^+ + \bar{u}_L + \begin{pmatrix} u \\ d \end{pmatrix}_L , \qquad (2.56)$$

where (x,y) denotes decomposition into $(SU(3)_c, SU(2)_L)$. In $SO(10)$ GUT, a right-handed neutrino is added to each generation. *i.e.*, fermions are placed in the $\mathbf{16}(= \mathbf{1}+\bar{\mathbf{5}}+\mathbf{10}$ under $SU(5))$. Fermions form the $\mathbf{27}$ representation in E_6 GUT. Namely, eleven new fermions are added to sixteen fermions of $SO(10)$. The $\mathbf{27}$ decomposes as

$$\mathbf{27} = (\mathbf{16},\mathbf{10})+(\mathbf{16},\bar{\mathbf{5}})+(\mathbf{16},\mathbf{1})+(\mathbf{10},\mathbf{5})+(\mathbf{10},\bar{\mathbf{5}})+(\mathbf{1},\mathbf{1}) \qquad (2.57)$$

in terms of $(SO(10), SU(5))$. (For a review of E_6 and its subgroups see Ref. [10].) Table 2.1 shows fermions in the $\mathbf{27}$ representation of E_6 and their quantum numbers in the standard model.

The E_6 GUT can contain two extra $U(1)$ symmetries beyond the standard model. We consider a breaking pattern:

$$E_6 \to SO(10)\times U(1)_\psi \to SU(5)\times U(1)_\chi \times U(1)_\psi \ .$$

The lightest extra Z boson is generally a linear combination of Z_ψ and Z_χ, associated with $U(1)_\psi$ and $U(1)_\chi$. Namely,

$$Z_0'(\alpha) = Z_\psi \cos\alpha + Z_\chi \sin\alpha \ . \qquad (2.58)$$

We assume that if there are two extra Z bosons, one of them is sufficiently heavy and does not affect the physics in our energy range. The values of the extra hypercharge $Y'(\alpha)$, which is the generator of the extra $U(1)$ symmetry leading to

$SO(10)$	$SU(5)$	Fermion	Color	I_3^L	Y/2	Q
16	**10**	$\begin{pmatrix} u \\ d \end{pmatrix}_L$	$\mathbf{3}$	$\begin{pmatrix} 1/2 \\ -1/2 \end{pmatrix}$	1/6	$\begin{pmatrix} 2/3 \\ -1/3 \end{pmatrix}$
		$\bar{u}_L$	$\bar{\mathbf{3}}$	0	−2/3	−2/3
		e_L^+	$\mathbf{1}$	0	1	1
	$\bar{\mathbf{5}}$	$\begin{pmatrix} \nu_e \\ e^- \end{pmatrix}_L$	$\mathbf{1}$	$\begin{pmatrix} 1/2 \\ -1/2 \end{pmatrix}$	−1/2	$\begin{pmatrix} 0 \\ -1 \end{pmatrix}$
		$\bar{d}_L$	$\bar{\mathbf{3}}$	0	1/3	1/3
		$\bar{\nu}_L$	$\mathbf{1}$	0	0	0
10	$\bar{\mathbf{5}}$	$\begin{pmatrix} N_E \\ E^- \end{pmatrix}_L$	$\mathbf{1}$	$\begin{pmatrix} 1/2 \\ -1/2 \end{pmatrix}$	−1/2	$\begin{pmatrix} 0 \\ -1 \end{pmatrix}$
		$\bar{h}_L$	$\bar{\mathbf{3}}$	0	1/3	1/3
	5	$\begin{pmatrix} E^+ \\ \bar{N}_E \end{pmatrix}_L$	$\mathbf{1}$	$\begin{pmatrix} 1/2 \\ -1/2 \end{pmatrix}$	1/2	$\begin{pmatrix} 1 \\ 0 \end{pmatrix}$
		h_L	$\mathbf{3}$	0	−1/3	−1/3
1	**1**	n_L	$\mathbf{1}$	0	0	0

Table 2.1: Fermions in the **27** representations of E_6.

Left-handed state	$Y'(\alpha)$
$\bar{d},\ e^-,\ \nu_e$	$\frac{1}{2\sqrt{6}}\cos\alpha - \frac{3}{2\sqrt{10}}\sin\alpha$
$u,\ d,\ \bar{u},\ e^+$	$\frac{1}{2\sqrt{6}}\cos\alpha + \frac{1}{2\sqrt{10}}\sin\alpha$
$\bar{\nu}_e$	$\frac{1}{2\sqrt{6}}\cos\alpha + \frac{5}{2\sqrt{10}}\sin\alpha$
$\bar{h},\ E^-,\ \nu_E$	$-\frac{1}{\sqrt{6}}\cos\alpha + \frac{1}{\sqrt{10}}\sin\alpha$
$h,\ E^+,\ \overline{N_E}$	$-\frac{1}{\sqrt{6}}\cos\alpha - \frac{1}{\sqrt{10}}\sin\alpha$
n	$\frac{2}{\sqrt{6}}\cos\alpha$

Table 2.2: The extra hyper charge $Y'(\alpha)$ in E_6 model.

Fermion	g'_{0V}	g'_{0A}
u	0	$\frac{1}{\sqrt{6}}\cos\alpha + \frac{1}{\sqrt{10}}\sin\alpha$
d	$\frac{2}{\sqrt{10}}\sin\alpha$	$\frac{1}{\sqrt{6}}\cos\alpha - \frac{1}{\sqrt{10}}\sin\alpha$
e^-	$-\frac{2}{\sqrt{10}}\sin\alpha$	$\frac{1}{\sqrt{6}}\cos\alpha - \frac{1}{\sqrt{10}}\sin\alpha$
ν_e	$-\frac{4}{\sqrt{10}}\sin\alpha$	$\frac{1}{\sqrt{6}}\cos\alpha + \frac{1}{\sqrt{10}}\sin\alpha$

Table 2.3: The vector and the axial coupling in E_6 model.

$Z'_0(\alpha)$, are shown in Table 2.2. The vector- and the axial-coupling constants are given as $g'^f_{0V} = Y'_f(\alpha) - Y'_{\bar f}(\alpha)$ and $g'^f_{0A} = Y'_f(\alpha) + Y'_{\bar f}(\alpha)$ for the fermion, f. The values for up-type quarks, down-type quarks, and leptons are given in Table 2.3.

This model has four parameters: α — the mixing angle between Z_ψ and Z_χ; θ' — the mixing angle between Z^0 and Z'_0; $M_{Z'}$ — the mass of the extra Z boson; and $\lambda \equiv g_{Z'}/g_Z$ — the relative strength of the coupling to Z'_0. In general, the mixing angle α can take arbitrary values, but is determined for the specific choice of E_6 model. We discuss four such choices: Z_ψ; Z_χ; Z_η; and Z_ν, corresponding to $\alpha = 0$, $\pi/2$, $\tan^{-1}\sqrt{3/5}$, and $\tan^{-1}(-\sqrt{1/15})$, respectively. The ratio λ is given by the renormalization-group equations as $\lambda^2 \le \frac{5}{3}\sin^2\theta_W$. This value is fixed for a specific symmetry-breaking scheme and takes its maximum for the case when the extra $U(1)$ symmetry breaks at the same energy scale as does $SU(3)_c \times SU(2)_L \times U(1)_Y$. In the following analysis, we assume $\lambda^2 = \frac{5}{3}\sin^2\theta_W$. Using eq. (2.47), we can also eliminate θ' from the free parameters, leaving only one parameter, namely $M_{Z'}$.

2.3.3 $SU(5)_c$ color model

This model was recently proposed by Foot and Hernandez [12]. It assumes the color group is $SU(5)_c$ and an extra $U(1)$ symmetry comes out when this $SU(5)_c$ breaks to $SU(3)_c$. Namely:

$$SU(5)_c \times SU(2)_L \times U(1)_{Y'} \to SU(3)_c \times SU(2)_{c'} \times U(1)_{c'} \times SU(2)_L \times U(1)_{Y'}\ .$$

Here, two neutral gauge bosons, corresponding to the two $U(1)$ symmetries, $Z_{Y'}$ and $Z_{c'}$, are mixed as

$$\begin{pmatrix} B \\ Z' \end{pmatrix} = \begin{pmatrix} \cos\beta & \sin\beta \\ -\sin\beta & \cos\beta \end{pmatrix} \begin{pmatrix} Z_{Y'} \\ Z_{c'} \end{pmatrix}, \tag{2.59}$$

where B is the B boson of the standard model, which mixes with the W^0 to yield the γ and Z^0, and Z' is an extra Z boson. Table 2.4 gives the quantum numbers of T_1, T_2, and T_3, which are the generators of $U(1)_{c'}$, $U(1)_{Y'}$, and the third component of $SU(2)_L$. These are normalized as $Q = T_1 + T_2 + T_3$, where Q is the charge of the particle. In this table, $\tilde u$ and $\tilde d$ are exotic quarks which have electric charges of $\pm 1/2$. They are $SU(2)_{c'}$ doublets and form $\mathbf{5}$ representations of $SU(5)$ with $SU(3)_c$ triplets, such as $(u, \tilde u)$ and $(d, \tilde d)$.

	u_L	d_L	u_R	d_R	$\bar{u}_L$	$\bar{d}_L$	$\bar{u}_R$	$\bar{d}_R$	ν_L	e_L	e_R
T_1	$+\frac{1}{15}$	$+\frac{1}{15}$	$+\frac{1}{15}$	$+\frac{1}{15}$	$-\frac{1}{10}$	$-\frac{1}{10}$	$-\frac{1}{10}$	$-\frac{1}{10}$	0	0	0
T_2	$+\frac{1}{10}$	$+\frac{1}{10}$	$+\frac{3}{5}$	$-\frac{2}{5}$	$+\frac{1}{10}$	$+\frac{1}{10}$	$+\frac{3}{5}$	$-\frac{2}{5}$	$-\frac{1}{2}$	$-\frac{1}{2}$	-1
T_3	$+\frac{1}{2}$	$-\frac{1}{2}$	0	0	$+\frac{1}{2}$	$-\frac{1}{2}$	0	0	$+\frac{1}{2}$	$-\frac{1}{2}$	0

Table 2.4: Quantum numbers in $SU(5)_c$ model.

The Z' couplings to left-handed (right-handed) fermions are given by

$$g'_{0L(R)} = T_2^{L(R)} \sin\theta_W \cot\beta - T_1^{L(R)} \sin\theta_W \tan\beta \ . \tag{2.60}$$

The vector- and the axial-coupling constants are $g'_{0V} = g'_{0L} + g'_{0R}$ and $g'_{0A} = g'_{0L} - g'_{0R}$, respectively.

Since the $SU(3)_c$ group of QCD spins off from $SU(5)_c$ as $U(1)_{c'}$ does in the electroweak sector, we can get the relation between $g_s \equiv \sqrt{4\pi\alpha_s}$, the strong coupling constant, and $g_1 = g'/\cos\beta$, the $U(1)_{c'}$ coupling constant. At the energy scale at which $SU(5)_c$ breaks, $g_1^2 TrT_1^2 = g_s^2 Tr(\lambda_a/2)^2$, where λ_a is any of Gell-Mann $SU(3)$ matrices and the left side is traced over the 5 representation. Then we obtain $g_1^2/30 = g_s^2/2$ or

$$\cos^2\beta = \frac{1}{15\cos^2\theta_W}\frac{\alpha}{\alpha_s} \simeq 0.0063 \ . \tag{2.61}$$

In this model, $\lambda \equiv g_{Z'}/g_Z = 1$ and the off-diagonal element of the mass matrix (2.43) is given as

$$b = -\sin\theta_W \cdot \cot\beta \simeq -0.038 \ . \tag{2.62}$$

Hence, we can deduce the mixing angle θ' for given M_Z and $M_{Z'}$ from eq. (2.46). Therefore, we can choose only one free parameter, $M_{Z'}$.

2.3.4 $SU(2)_q \times SU(2)_l \times U(1)_Y$ model

This model was proposed recently by Georgi, Jenkins, and Simmons [13]. Its electroweak gauge group is $SU(2)_q \times SU(2)_l \times U(1)_Y$. Specifically, it has separate $SU(2)$ symmetries for the quark sector and the lepton sector. We denote the gauge

bosons corresponding to $SU(2)_q$ and $SU(2)_l$ as $W_q^{0,\pm}$ and $W_l^{0,\pm}$. They are mixed through an angle ϕ as

$$\begin{pmatrix} W_1^{0,\pm} \\ W_2^{0,\pm} \end{pmatrix} = \begin{pmatrix} \cos\phi & \sin\phi \\ -\sin\phi & \cos\phi \end{pmatrix} \begin{pmatrix} W_l^{0,\pm} \\ W_q^{0,\pm} \end{pmatrix} , \tag{2.63}$$

where $W_1^\pm$ is regarded as the standard model $W^\pm$. W_1^0 is mixed with B boson of $U(1)_Y$ through the Weinberg angle, θ_W and becomes the γ and Z^0 of the standard model. The remaining bosons, W_2^0 and $W_2^\pm$ are the extra Z and extra W bosons of this model.

The vector- and the axial-coupling constants of the extra Z boson are given by

$$g'_{0V} = g'_{0A} = \begin{cases} -I_3^L \tan\phi & \text{for leptons} \\ I_3^L \cot\phi & \text{for quarks} \end{cases} \tag{2.64}$$

where I_3^L is the third component of the isospin of the left-handed state in the standard model. The relative strength of the Z'_0 coupling to the Z^0 coupling is $\lambda = \cos\theta_W$. There are three parameters in this model, $M_{Z'}$, ϕ, and θ'. Eq. (2.44) is not correct in this model because the mass eigen state of the W is the mixture of the standard model W and the $W_2^\pm$. Thus, we cannot use eq. (2.47) to eliminate θ' as a free parameter.

Chapter 3

The Experimental Apparatus

The research described in this thesis is based on the data taken with the AMY detector at the TRISTAN e^+e^- collider. In this chapter, the TRISTAN collider and the AMY detector are described.

3.1 The TRISTAN collider

TRISTAN (Transposable Ring Intersecting STorage Accelerator in Nippon) [14] is an e^+e^- collider system at KEK, the National Laboratory for High Energy Physics in Japan. A overview of KEK and the TRISTAN complex is shown in Fig. 3.1. The TRISTAN complex consists of four accelerator systems: the positron generator, the Linear Accelerator (LINAC), the Accumulation Ring (AR), and the Main Ring (MR).

Positrons, generated by colliding 200 MeV electrons from a dedicated linear accelerator with a tantalum target, are injected into the 390 m long LINAC, where they are accelerated to an energy of 2.5 GeV and injected into the AR. In AR, which has a 377 m circumference, about 20 mA of positrons are accumulated in a single bunch and accelerated to 8 GeV and injected into the MR. This cycle is repeated 8 times until there is about 7 mA of positrons in two diametrically opposite bunches circulating counterclockwise in the 3 km circumference MR. Then electrons generated from a triode gun are injected into the same LINAC and a similar sequence is repeated producing two similar bunches of electrons ciculating clockwise in the MR. Finally, the electrons and positrons are accelerated up to

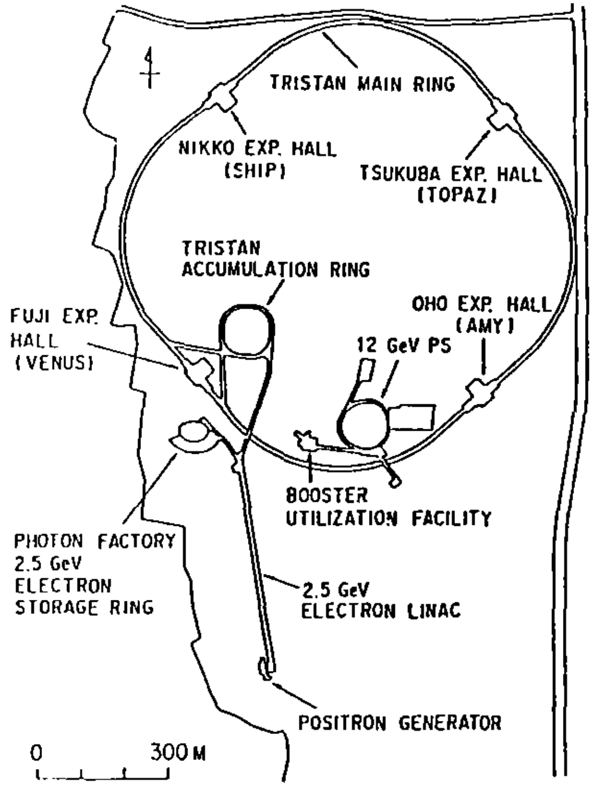

Figure 3.1: An overview of the TRISTAN collider at KEK.

the target energy and collided at four interaction points located in Oho, Tsukuba, Nikko, and Fuji experimantal halls.

The first collisions occured at a center-of-mass energy of 50 GeV in November, 1986. For the next three years, TRISTAN operated in the energy range $\sqrt{s} = 50 \sim 64$ GeV, which were the highest energy e^+e^- collisions in the world until the SLC at SLAC and LEP at CERN began operations in 1989. In 1990, TRISTAN stopped the quest for higher energies, and started operating for high luminosity at the fixed energy of $\sqrt{s} = 58$ GeV with the goal of accumulating enough data for precision measurements (TRISTAN phase II). For that purpose, pairs of superconducting quadrupole magnets "QCS" were installed at each collision point in 1990, providing the capabilty to operate with smaller beam sizes at the collison point and, thus, a higher luminosity. TRISTAN achieved luminosity levels of about $1 pb^{-1}$/day at each interaction point in 1992.

3.2 The AMY Detector

The AMY detector [15], located at the OHO experimental hall of the TRISTAN e^+e^- storage ring, is a general-purpose detector based on a 1.2 m radius, 3-Tesla superconducting solenoidal magnet that is coaxial to the e^+e^- beamline. Charged particles and γ−rays are detected by cylindrical tracking chambers and electromagnetic shower calorimeters located inside of the magnet. Drift chambers and scintillation counters located outside of the iron flux-return yoke of the magnet are used to identify muons.

A series of upgrades of the AMY detector was done from 1989 to 1991 for the sake of the TRISTAN phase II measurements. A synchrotron X-ray detector (XRD) for electron identification and and a precision vertex detector (VTX) were installed in the barrel part, and all the endcap region detector components were replaced. (Each detector component is described below.) We call the upgraded detector "AMY 1.5", while the original detector is called "AMY 1.0". Schematic views of the AMY 1.0 detector and the AMY 1.5 detector are shown in Fig. 3.2 and Fig. 3.3. In this section we give brief descriptions of the various detector components.

The space coordinate system of the AMY detector is defined in the following way: The origin of the coordinates is the nominal center of the beam interaction

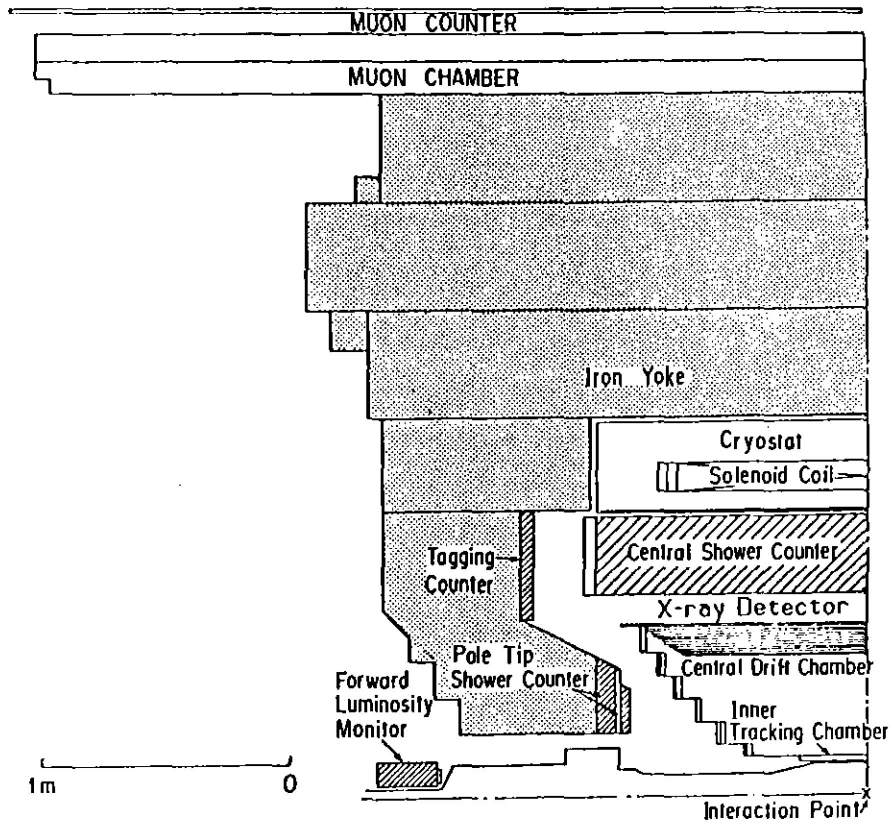

Figure 3.2: A schematic view of the AMY 1.0 detector.

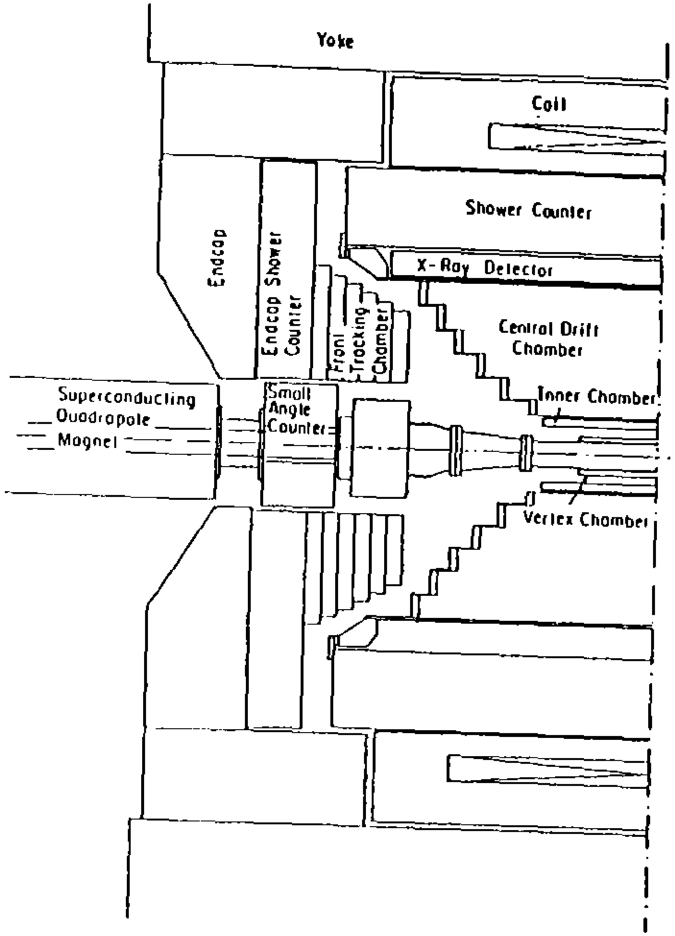

Figure 3.3: A schematic view of the AMY 1.5 detector.

point; the positive z-direction is the direction of the electron beam; the y-axis points vertically upward; and the x-axis points radially outward from the center of the TRISTAN MR. The polar coordinates r, θ and ϕ are defined in the standard way. Namely, r is the distance from the origin, θ is the angle from the positive z-axis, and ϕ is the projected angle in the xy plane measured counter-clockwise from the positive x-axis.

The electron beam in AMY comes from the direction of TRISTAN's Tsukuba interaction hall and heads toward the Fuji interaction hall. Thus, we call the positive z end of the detector the "Fuji" end, and the negative z end the "Tsukuba" end.

3.2.1 The Charged Particle Tracking System

The charged particle tracking system, which measures the trajectories of charged particles from which their momenta are determined, is composed of three coaxial cylindrical chambers. Surrounding the beam pipe, there are the Vertex Chamber (VTX) [16], the Inner Tracking Chamber (ITC) [17], and the Central Drift Chamber (CDC) [18].

The VTX, the innermost component of the AMY detector, was installed in December, 1990. It is a four-layer cylindrical drift chamber made of cathodes formed from aluminized mylar straws whose diameters range from 4.6 to 5.6 mm. Each layer consists of eighty 56 cm straws filled with HRS gas (Ar 89%, CO_2 10%, CH_4 1%) pressurized to two atmospheres with a 20 μm diameter Stableohm resistive anode wire strung along the axis. The single-wire resolution is expected to be 50 μm in $r-\phi$ plane. The z-coordinates of tracks are measured using charge division read-out from both ends of the wires, with the resolution of about 5 mm. The purpose of the VTX is to provide a precise measurement of secondary vertices from heavy particle decays. It also helps tracking in the small angle region because of its larger θ coverage ($13^\circ \leq \theta \leq 167^\circ$).

The ITC (Fig. 3.4) consists of four layers of drift tubes (aluminized plastic tubes with 16μm diameter anode wires stretched along their axes) ranging in diameter from 5.5 to 6 mm. Each layer provides a position measurement of trajectory coordinates in the plane perpendicular to the beam direction (the $r-\phi$ plane) with a spatial resolution of $\sigma \sim 80\mu$m. The gas in the ITC (50% Ar, 50% C_2H_6)

is pressurized to 1.46 atmospheres to improve the spatial resolution. The active region of the ITC extends from a radius of 12.2 cm to 14.2 cm and its fiducial length along the beam direction (the z axis) is 55 cm. The ITC is not only a tracking device but also an essential part of the trigger system. Signals from the ITC trigger system, which are independent from the main trigger system, are combined with triggers based on other detector elements and are also used alone. The ITC information is especially useful for suppressing cosmic ray induced triggers.

The CDC (Fig. 3.5), located just outside the ITC, has 40 cylinders of wire drift cells extending out to a radius of 65 cm. Twenty five of the cylinders, consisting of 5616 individual drift cells each approximately 6 mm in radius, have wires parallel to the z-axis for measuring the $r-\phi$ coordinates of trajectory points; the other 15 cylinders, consisting of 3432 cells, have wires at a small angle (typically 5°) relative to the beam direction to provide small angle stereo measurements of z-coordinates. For most of the results being reported here, the CDC was filled with HRS gas at atmospheric pressure. All of the data at $\sqrt{s} = 54, 61.4, 63.6, 64$ GeV and a portion of the $\sqrt{s} = 58$, 60 and 60.8 GeV data were taken with a 50:50 mixture of Neon and Ethane. Neon/Ethane gas was used to make the CDC more transparent to X-rays during the time that the XRD was being used.

The cylinders are arranged in six super-layers of increasing length. Each super-layer provides a local determination of the track vector (position and direction). This enables quick estimates of the multiplicity and momenta of charged particles for triggering the data acquisition system, and facilitates the recognition of tracks in the off-line analysis. The hexagonal shape of the cells automatically results in staggered cells, which simplifies the resolution of left/right ambiguities. The almost circular cell shape is helpful for achieving good spatial resolution in the presence of the 3 Tesla magnetic field, where the Lorentz angle of drifting electrons can be as large as 80°.

The average spatial resolution of the axial (stereo) cells of the CDC is $\sigma \sim 140$ (210) μm (Fig. 3.6). The overall resolution of the central tracking devices (ITC and CDC) is estimated from Bhabha scattering events ($e^+e^- \rightarrow e^+e^-$) to be $\Delta p_t/p_t \simeq 0.6\%\ p_t(\mathrm{GeV}/c)$ for high momentum tracks with $|\cos\theta| < 0.87$. The techniques used to calibrate the CDC are described in detail in Ref. [19], and the track finding algorithms are explained in Ref. [20].

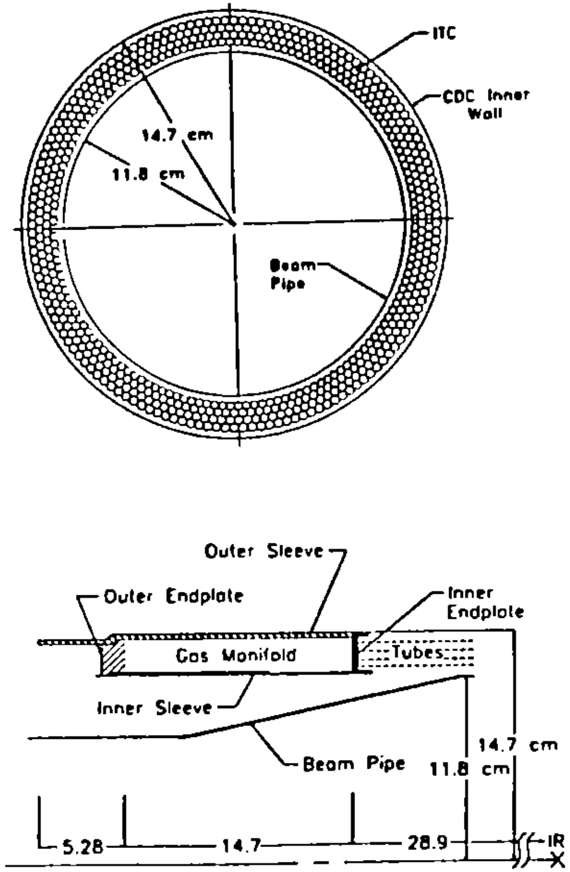

Figure 3.4: Cross-sectional views of the ITC.

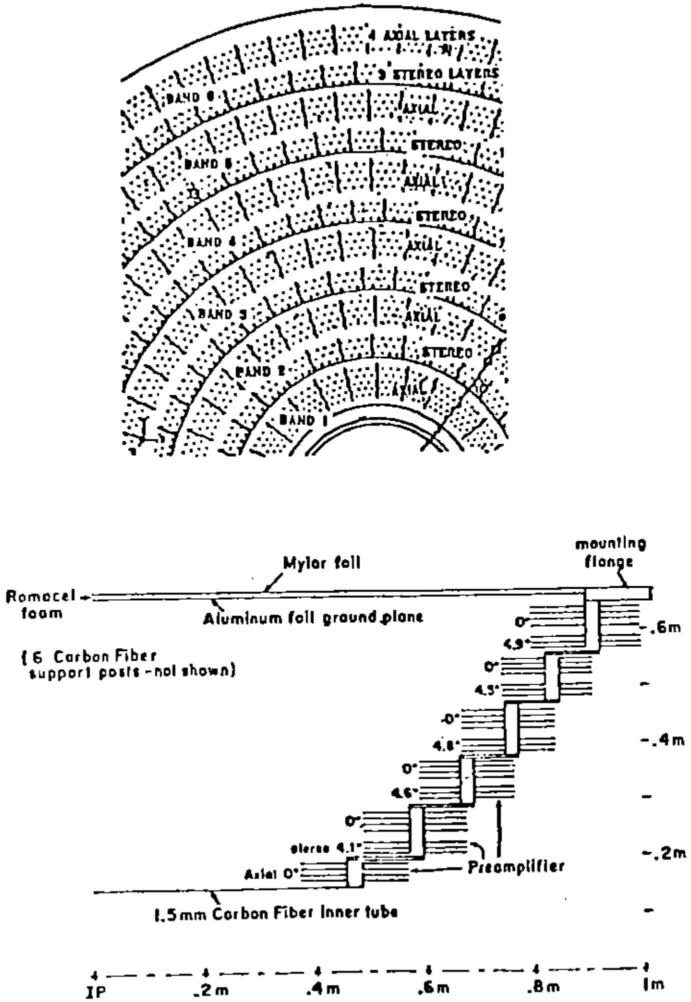

Figure 3.5: Overviews of the CDC.

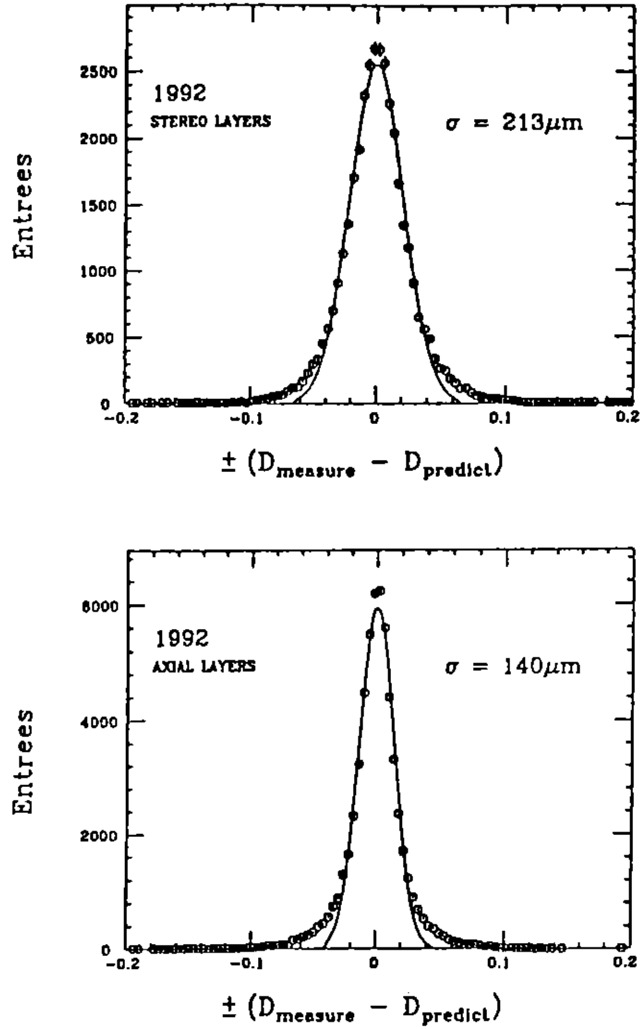

Figure 3.6: Track residuals measured in the CDC.

3.2.2 The X-ray Detector

The X-ray detector (XRD) [21] is a drift chambers filled with 95% Xe + 5% Propane that occupies the region between r = 67 cm and 79 cm. Sense wires, made of 20 μm diameter Stablohm 800, and field wires, made of 200 μm Cu/Be, are strung at r = 73 cm with a 2 mm spacing. The XRD detects synchrotron x-rays, radiated from electrons bent by 3 tesla magnetic field, which are used for electron identification. The XRD was used from May, 1989 to July, 1990. During this period, Neon/Ethane gas was used in the CDC.

3.2.3 The Electromagnetic Shower Counter

The barrel electromagnetic shower counter (SHC) [22] is a cylindrical device comprised of six sextants. Each sextant subtends an angle of 60° in ϕ, and occupies the region from 80 cm $\leq r \leq$ 110 cm and $|\cos\theta| \leq 0.75$. Each sextant consists of an alternation of 20 layers of proportional tubes and 19 layers of lead, totaling $14.5/|\sin\theta|$ radiation lengths. The detector is operated with a gas mixture of 49.3% Argon, 49.3% C_2H_6 and 1.4% alcohol at a voltage of 2150 volts. An overview and the layer structure of the SHC are shown in Fig. 3.7.

The individual cells consist of extruded resistive plastic tubes 222 cm in length with a 50μm anode wire stretched through its center. Facing the outer surfaces of each tube layer are double-sided printed circuit boards with rectangular cathode strips that are sensitive to induced signals from the anode wires. The boards provide segmentation in 14 mrad intervals in the θ and ϕ directions. The signals are joined into groups within the detector. In the case of the θ and ϕ signals, strip signals are combined in a tower arrangement into subgroups providing five measurements of the longitudinal shower development. In the case of the anode wires, signals from about ten adjacent tubes in a given layer are tied together. This arrangement results in a total of about 11,000 cathode and 960 anode channels.

Each sextant is a self-contained gas-tight unit including four monitor tubes containing radioactive ^{55}Fe sources. These tubes measure gain variations caused by changes in gas composition, atmospheric pressure and temperature.

Tests performed with prototype units and with actual sextants placed into a 1~5 GeV test beam demonstrate spatial resolutions for minimum ionizing particles of $\sigma \simeq 4$ mm, which translates into an angular resolution in AMY of $\sigma_{\theta,\phi} = 5$ mrads.

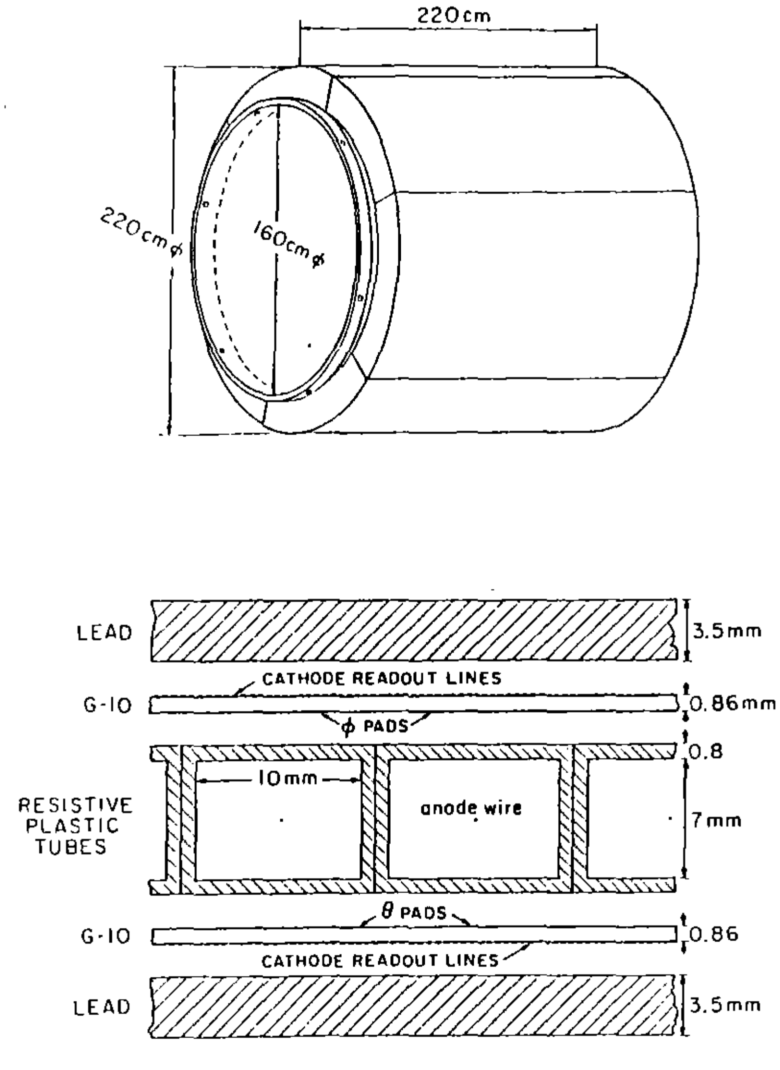

Figure 3.7: An overview and the layer structure of the SHC.

The energy resolution determined in the test beam agreed with expectations, based on the EGS4 Monte Carlo program,[23] of $\Delta E/E = 0.25/\sqrt{E(GeV)}$ with no magnetic field. We studied the detector's performance in the 3 Tesla field of the AMY detector using electrons from Bhabha events and from the two-photon process $e^+e^- \to e^+e^-e^+e^-$. The effects of the magnetic field degrade the energy resolution to $\Delta E/E = 0.23/\sqrt{E(GeV)} + 0.06$.

3.2.4 The Superconducting Magnet

The 3 Tesla magnetic field is produced by an eight-layer coil made of a Nb/Ti superconducting cable that contains both Cu and Al for stabilization. The coil is embedded in a hexagonal iron return yoke [24]. Because all of the detection devices, with the exception of the muon identification system, are inside the coil, no special efforts were made to minimize the coil thickness and a conventional pool-boiling cooling method is used. A 5000-ampere electric current provides the 3 Tesla field; the stored energy is 40 mega-joules.

We measured the magnetic field along the beam line with all the detector components in place and compared the result with a calculation done using the computer program POISSON [25]. The agreement was within $\pm 0.3\%$ after a proper normalization of the central field. The field strength elsewhere inside the detector is then estimated by POISSON, which is expected to give an error of less than 0.4% inside the tracking devices. There is sizable non-uniformity in the field strength; over the tracking volume of the CDC, the field strength varies from -18% to +5% of its value at the interaction point.

3.2.5 The Muon Identification System

The material of the SHC, the magnet coil, and the iron return yoke amounts to 1.3 kg/cm^2 (the equivalent of 1.6 m of iron) at normal incidence, which corresponds to about nine absorption lengths for strongly interacting particles. Particles penetrating this material are identified by the muon detection system (MUO), consisting of four layers of drift cells and one layer of plastic scintillator, situated outside of the iron return yoke and covering the angular region $|\cos\theta| < 0.74$. The cells have a 5×10 cm^2 cross-section and a spatial resolution that is typically 1 mm. Two layers of cells are 6.5 m long and have wires parallel to the beam axis; two layers of cells

range in length from 2.8 to 4.1 m and have wires perpendicular to the beam. The combined system has a track segment reconstruction efficiency that is greater than 98%. Scintillation counters, located just outside the drift chambers, measure the time of penetrating particles relative to the beam crossing time with a precision of about 3 ns, providing discrimination against backgrounds from cosmic rays which are randomly distributed in time.

3.2.6 The Endcap Detectors in AMY 1.0

Particles emitted at smaller angles are detected in the Pole Tip Counter (PTC) [26], which covers the region $15° < \theta < 27°$ and the Ring Shower Counter (RSC), covering $26° < \theta < 39°$ Each of these detection systems consists of two units placed on the endcaps of both ends (Fuji and Tsukuba).

Each PTC unit consists of two modules of lead/scintillator calorimeters with a plane of proportional tubes between them. The total thickness of the calorimeter modules is 14 radiation lengths. This device provides measurements of the energies and positions of electrons and photons and the positions of other charged particles incident on it. Its primary function is the determination of the luminosity by detecting Bhabha scattering events. Its energy resolution is $\Delta E/E = 29\%/\sqrt{E(GeV)} + 6\%$. The position resolution is about 4 mrad and 14 mrad for the θ and ϕ directions, respectively.

Each Ring Shower Counter (RSC) unit consists of two layers of lead and scintillator (1 cm thick lead and 1 cm thick scintillator for each layer) and signals the presence of showering particles (either electrons or photons). Charged tracks that enter the RSC are visible in a minimum of 15 CDC layers and electrons among these tracks can be identified by comparing the RSC measured energy with the CDC measured momentum. The RSC energy resolution is $\Delta E/E = \sqrt{29^2 + 39^2/E(GeV)}\%$.

In addition, there are the luminosity monitors (LUM) in the forward region ($4° < \theta < 6°$), which are counters used to measure the instantaneous luminosity and to monitor beam-related background radiation levels.

3.2.7 The Endcap Detectors in AMY 1.5

In the upgrade to AMY 1.5, the PTC and RSC of AMY 1.0 were replaced by the Endcap Shower Countesr (ESC) [27], which started operating in November,

1989. Each ESC unit has two modules ("front" and "back") of lead/scintillator calorimeters, which are 4.5 and 8.9 radiation lengths thick, with a resistive tube chamber between them for position measurement. Each calorimeter section is divided azimuthally into twelve wedge shape sections. The ESC covers the region $11^\circ < \theta < 37^\circ$ and its energy resolution is $\Delta E/E = 14.7/\sqrt{E(GeV)} + 6.2\%$.

The Small Angle Calorimeter (SAC) replaced the LUM of AMY 1.0. Each SAC unit consists of arrays of defining scintillators, silicon pad position detectors and a lead-scintillator calorimeter of 17.2 radiation length. The SAC covers the angular range $2^\circ < \theta < 11^\circ$ and its energy resolution is $\Delta E/E = 10.1\%/\sqrt{E(GeV)} + 1.6\%$.

The Forward Tracking Chamber (FTC), which was installed in September, 1990, is a set of two units of tracking chambers placed on the ESC. Each unit consists of 15 layers with approximately 60 cells in each layer. The FTC is filled with HRS gas and the electric field is shaped by 75 μm sheets of resistive Kapton ($10^{12}\Omega/cm^2$). The chambers planes are oriented to provide three views rotated by 120° each other with five planes for each view. The FTC covers the angular region $12^\circ < \theta < 27^\circ$, and provides tracking of charged particles in the small angle region.

3.2.8 Triggering

The frequency of beam crossings at TRISTAN is 200 kHz, and, in most cases, no small-distance electron-positron interactions occur. The task of the trigger system is to decide whether or not an "interesting" interaction occured in each beam crossing, a decision that is made in the 5μsec interval between beam crossings. In order to be sensitive to as many e^+e^- processes as possible, the trigger requirements for the detector are kept as loose as possible, but consistant with the capability of the AMY data acquisition system ($\sim$ 3 Hz). As a result, we typically record approximately 5,000 events/hour, of which only a few are actual hadronic events, di-muon events, or $\tau^+\tau^-$ events, used in this analysis. The bulk of events the AMY detector detects are "junk" events, induced by interactions of stray beam particles with the material in the walls of the vacuum chamber (beam-wall events), interactions of beam particles with atoms of the residual gas in the vacuum chamber (beam-gas events), cosmic rays, *etc.* We form about 20 kinds of triggers. Among them, those relevant to the detection of hadronic events are described in Chapt. 4, and those relevant to di-muon and $\tau^+\tau^-$ events are described in Chapt. 5.

3.2.9 Data Acquisition

A computer-controlled FASTBUS system of electronics digitizes analog signals and timing signals from each component of the detector for each event. Triggers and the high voltage status are recorded for each event by a CAMAC system. Environmental conditions and the SHC monitor tube gain are measured periodically. All the digitized data are read in to a VAX-11/780 computer, where they are temporarily stored. Here, various checks are made to monitor operation of the entire detector system. The data are then sent via an optical link to a FACOM M780 computer, where the data format is immediately rearranged for the convenience of later analyses. The data are stored in a cassette-tape library from which it is subsequently accessed for offline analyses. A schematic diagram of the data acquisition system is illustrated in Fig. 3.8.

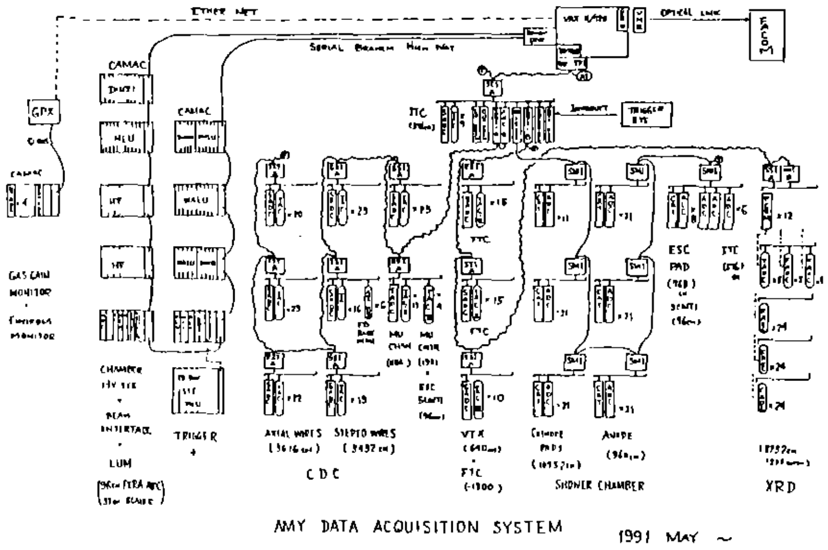

Figure 3.8: A schematic diagram of AMY 1.5 data acquisition system.

Chapter 4

Total Hadronic Cross Section

The total hadronic event cross section is conventionally reported in terms of the R value, the ratio of the total hadronic cross section to the lowest-order QED di-muon cross section, as discussed in **2.2.2**.

Experimentally, the R value is determined from the relation

$$R = \frac{N_{selected} - N_{bkg}}{eff \cdot (1+\delta) \int L dt \, \sigma_0}, \tag{4.1}$$

where $N_{selected}$ is the number of hadronic events selected experimentally, N_{bkg} is the estimated number of background events, eff is the detection efficiency, $1+\delta$ is the radiative correction, $\int L dt$ is the integrated luminosity, and σ_0 is the QED di-muon cross section given by eq. (2.26). In the following sections, we discuss how each term is determined.

4.1 Luminosity Measurement

Small-angle Bhabha scattering, where t-channel exchange dominates, is a well understood QED process. We measure luminosity by counting the number of Bhabha events detected in the endcap detector, *i.e.*, PTC in AMY 1.0 or ESC in AMY 1.5, and comparing with Monte Carlo simulations of events generated according to a calculation that includes diagrams up to $O(\alpha^3)$. The integrated luminosity for each run period is listed in Table 4.1. Also shown are independent luminosity determinations based on Bhabha events detected in the barrel region of the detector (CDC and SHC). They are in good agreement within errors.

AMY 1.0

Run Period	$\sqrt{s}$ (GeV)	PTC Bhabha $0.92 \leq \lvert\cos\theta\rvert \leq 0.96$ (pb^{-1})	SHC Bhabha $\lvert\cos\theta\rvert \leq 0.73$ (pb^{-1})
02	50.0	0.636 ± 0.016	0.64 ± 0.04
03	52.0	3.976 ± 0.080	3.88 ± 0.10
04	55.0	3.266 ± 0.039	3.42 ± 0.10
05	56.0	5.993 ± 0.053	6.06 ± 0.13
07	56.5	0.994 ± 0.022	1.05 ± 0.06
08	57.0	4.398 ± 0.046	4.44 ± 0.12
09	60.0	3.202 ± 0.042	—
10	58.5	0.801 ± 0.016	0.73 ± 0.05
11	ESCAN†	1.225 ± 0.020	—
	(59.0)	0.094 ± 0.006	—
	(59.05)	0.504 ± 0.013	0.46 ± 0.04
12	60.8	2.312 ± 0.058	2.48 ± 0.09
13	59.0	0.627 ± 0.020	0.63 ± 0.05
14	60.0	0.350 ± 0.013	0.35 ± 0.03
15	60.8	1.169 ± 0.029	1.20 ± 0.06
16	61.4	4.287 ± 0.060	4.17 ± 0.12
17	54.0	0.531 ± 0.017	0.43 ± 0.04

† energy scan run at $\sqrt{s} = 57.25 \sim 59.5$ GeV

AMY 1.5

Run Period	$\sqrt{s}$ (GeV)	ESC Bhabha $0.82 \leq \lvert\cos\theta\rvert \leq 0.98$ (pb^{-1})	SHC Bhabha $\lvert\cos\theta\rvert \leq 0.73$ (pb^{-1})
18	64.0	1.097 ± 0.017	—
19	63.6	0.440 ± 0.011	—
20	58.0	27.157 ± 0.076	26.64 ± 0.69
21	58.0	7.10 ± 0.04	6.96 ± 0.16
22	58.0	26.57 ± 0.07	26.03 ± 0.30

Total integrated luminosity is 95.50 pb^{-1}.

Table 4.1: A summary of the integrated luminosities measured with the PTC (AMY 1.0), ESC (AMY 1.5), and SHC. The point-to-point errors are listed for PTC and ESC luminosities, while only the statistical errors are listed for SHC luminosities. There is an additional overall normalization error of 2.4% (1.3%) for the PTC (ESC) luminosity.

The estimated contamination of the Bhabha sample from $e^+e^- \to \gamma\gamma(\gamma)$ and $e^+e^- \to e^+e^-\gamma$ events, which are not distinguished from Bhabha scattering because there is no charged-particle track information for small angles, is subtracted. The cross sections for these processes are calculated to $O(\alpha^3)$ and a systematic error on the background subtraction is estimated to be 0.2% for PTC and 0.04% for ESC. Systematic errors in the estimates of trigger efficiency, chamber efficiency, and detector acceptance are also taken into account. These are 0.2%, 0.1%. and 1.3% (0%, 0.05%, and 0.41%), respectively for the PTC (ESC) Bhabha event samples. Since there is no complete $O(\alpha^4)$ calculation of Bhabha scattering, we estimated its magnitude and included that in the error of the detector acceptance. The largest contribution to the systematic error comes from possible misalignments of the PTC and ESC. The uncertainty level of our survey of the position of these devices translates into an error that is estimated to be 2.0% for the PTC and 1.22% for the ESC. By adding all errors listed above in quadrature, we get total over-all error in the luminosity measurement of 2.4% for PTC and 1.3% for ESC.

There are other sources of errors which are dependent on run periods. These include statistical errors and systematic errors arising from corrections that are made for nonoperating sections of the detectors. These errors are treated as point-to-point errors. More details of the PTC luminosity measurement appear in Ref. [26].

4.2 Hadronic Event Selection

4.2.1 Triggering

For multihadron events, triggers are generated via three quasi-independent systems:

SHC total energy trigger This requires that an analog sum of the pulse heights from the 48 SHC anode towers exceed a threshold, which is typically $\sim$ 3 GeV, and adjusted to produce a trigger rate not exceeding $\sim$0.3 Hz.

CDC multi track trigger This requires the presence of four or more radial track segments in each of the outer five CDC disks.

ITC + CDC "loose" multi-track trigger This places a weak demand on the presence of CDC track segments and requires the detection of two or more track segments in the ITC.

All three systems render a decision in less than 2.0 μs, and the combined rate is much less than the 3.0 Hz capacity of the data-logging system. Typically, most events in the hadronic sample satisfied the requirements of all three trigger systems.

The SHC trigger is completely independent from other two, which enables us to estimate the trigger inefficiency for hadronic events as follows: In the final selected hadron sample, we estimated the inefficiency of:

- the SHC trigger **OR** the CDC trigger, as the fraction of events triggered by the CDC+ITC trigger but neither the SHC nor CDC triggers; and
- the SHC trigger **OR** the CDC+ITC trigger in an analagous way.

We take the smaller one as an upper limit on the inefficiency of the whole trigger system. The results are summarized in Table 4.2. Since hadronic events could also fire many of the other triggers, the actual inefficiency may be smaller. Therefore, we conclude the trigger inefficiency for hadronic events is negligible.

4.2.2 Filter

All of the recorded events are passed through an online filtering process. A fast CDC-track finding algorithm (ACE [20]) is applied to find charged particle tracks in the CDC and to estimate their momenta. An SHC cluster finder algorithm is also applied and the energy of each cluster is determined using a preliminary SHC calibration. Then, candidates of hadronic events ("pre-hadron" events) are selected by requiring the following conditions:

(i) The number of CDC tracks with $|R_0| < 5\ cm$, $|Z_0| < 10\ cm$, and $\chi^2 \leq 10000$, is more than two. Here R_0 and Z_0 are r- and z-component of the distance of closest approach of the track to the beam interaction point, respectively.

(ii) The total energy deposited in the SHC (E_{SHC}) is greater than 2.8 GeV

(iii) The total energy deposited in the ESC (E_{ESC}) is greater than 3.0 GeV
AND
{ The difference between E_{ESC}(Fuji) and E_{ESC}(Tsukuba) is less than E_{SHC}
OR E_{ESC}(Fuji) $<$ 10 GeV **OR** E_{ESC}(Tsukuba) $<$ 10 GeV }

(i) $\cap$ (ii) is used for AMY1.0, while (i) $\cap$ {(ii) $\cup$ (iii)} is used for AMY1.5 .

Run Period	$\sqrt{s}$ (GeV)	Trigger Inefficiency (%) SHC	CDC	CDC+ITC	Total
02	50.0	44.3	17.0	9.1	4.0
03	52.0	3.3	2.1	6.8	0.1
04	55.0	0.0	2.7	2.2	0.0
05	56.0	0.0	3.4	4.5	0.0
07	56.5	0.0	2.4	1.6	0.0
08	57.0	0.0	2.2	4.3	0.0
09	60.0	9.2	1.6	1.1	0.0
10	58.5	14.6	0.0	2.2	0.0
11	ESCAN	11.6	3.0	3.7	0.3
12	60.8	2.9	3.3	1.2	0.0
13	59.0	0.0	0.0	1.6	0.0
14	60.0	0.0	0.0	0.0	0.0
15	60.8	1.6	3.2	3.2	0.0
16	61.4	2.5	1.4	0.7	0.0
17	54.0	6.6	6.6	0.0	0.0
18	64.0	4.5	1.8	31.5	0.1
19	63.6	34.1	0.0	31.7	0.0
20	58.0	1.8	2.0	13.0	0.0
21	58.0	1.6	1.2	35.7	0.0
22	58.0	0.9	0.6	30.9	0.0

Table 4.2: A summary of the hadronic event trigger inefficiencies.

4.2.3 Track reconstruction

A more precice tracking algorithm for reconstructing tracks in ITC and CDC, based on the program DUET [28], is applied to the "pre-hadron" event samples. The energies of the SHC clusters are redetermined using a more accurate SHC calibration. Tracks and hits in the detector components that are not used for hadronic event selection are also analysed in this stage.

We define "good" CDC tracks and "good" SHC clusters as follows:

A "good" CDC track is a CDC track that:

- uses more than 8 axial wire hits and more than 5 stereo wires hits;
- extrapolates to a vertex position (R_0, Z_0) with $|R_0| \leq 5$ cm and $|Z_0| \leq 15$ cm;
- fits to a helix in $r\phi$ and z with $\chi^2_{r\phi} \leq 8.0$ and $\chi^2_z \leq 6.0$;
- has a polar angle θ in the angular region $|\cos\theta_{track}| \leq 0.85$, where θ_{track} is the angle between the CDC track and z-direction;
- and is not a "curler."
  A low transverse momentum track may reenter CDC and appear as many different reconstructed tracks. Such tracks are called "curlers" and are removed by means of an algorithm described in Ref. [29]. This cut is not applied to the data at $\sqrt{s}$ = 50, 52, 55, 56, 56.5, and 57 GeV.

There are additional conditions for high momenta tracks:
for tracks with $|P| > 0.5$ GeV,

- more than 12 axial wire hits or more than 10 stereo wire hits or $|R_0| \leq 2$ cm;

for tracks with $|P| > E_{beam}/4$,

- more than 12 axial wire hits or more than 10 stereo wire hits or $|R_0| \leq 1$ cm .

A "good" SHC cluster is a SHC cluster that:

- has an energy $E_{cluster} > 0.2$ GeV, where $E_{cluster}$ is the energy of the cluster;

- has no single layer with an energy the is more than 95 % of $E_{cluster}$ (for clusters with $E_{cluster} > 0.5$ GeV);
- does not overlap with CDC tracks or $E_{cluster} > 1$ GeV;
- is in the angular region $|\cos\theta_{cluster}| \leq 0.73$, where $\theta_{cluster}$ is the angle between the cluster and z-direction. This cut is not applied to the data at $\sqrt{s}$ = 50, 52, 55, 56, 56.5, and 57 GeV.

The CDC-SHC overlap cut is to eliminate SHC energy clusters produced by charged tracks.

4.2.4 Final Selection

In hadronic annihilation events, quark and gluon fragmentation results in many particle final states, where most of the initial center-of-mass energy is carried by those final state particles. Thus, hadronic annihilation events are charaterized by high particle multiplicities and a large visible energy. Fig. 4.1 shows an example of a typical hadronic event detected by AMY.

Sources of background events include:

1. Beam-Wall/Gas interactions, which are interactions between beam particles and the atomic nuclei of the material of the beam pipe, or with the residual gas molecules in the vacuum.
2. Radiative Bhabha events ($e^+ + e^- \rightarrow e^+ + e^- + \gamma$), where the photon is converted into an e^+e^- pair in the material of the beam pipe, VTX, or ITC.
3. $\tau^+\tau^-$ events ($e^+ + e^- \rightarrow \tau^+ + \tau^-$), where the final state τ's decay into hadrons.
4. Two-photon hadronic events ($e^+ + e^- \rightarrow e^+ + e^- + hadrons$), which produce hadrons via the process shown in Fig. 4.2.
5. Cosmic ray events that produce showers in the detector and fake high multiplicity events.

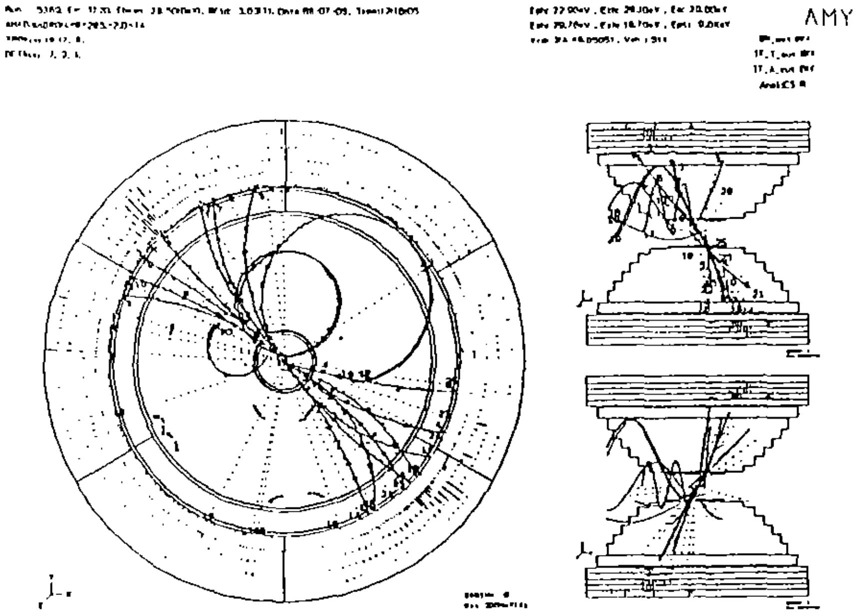

Figure 4.1: A typical hadronic event observed by the AMY detector.

To reject these background events, we defined the final hadronic selection criteria as follows:

(i) $N_{CDC} \geq 5$,
where N_{CDC} is the number of "good" CDC tracks. This cut rejects $\tau^+\tau^-$ and radiative Bhabha events, which always have low multiplicity.

(ii) $E_{vis}/\sqrt{s} > 0.5$,
where the visible energy, E_{vis}, is the sum of the absolute momenta of all "good" CDC tracks and the energies of all "good" SHC clusters. This cut rejects Beam-Wall/Gas events, where the energy cannot exceed $\sqrt{s}/2$, and most two-photon hadronic events.

(iii) $|\sum P_z|/E_{vis} < 0.4$,
where the momentum balance, $\sum P_z$, is the sum of the z-components of the momenta of all "good" CDC tracks and the z-components of the energies of all "good" SHC clusters ($E_{cluster} \cdot \cos\theta_{cluster}$). This cut rejects two-photon hadronic events, whose momentum is not balanced because the scattered electrons are rarely detected by the barrel detectors.

(iv)

$$E_{SHC} > \begin{cases} 3 \text{ GeV} & \text{for 50 and 52 GeV data} \\ 5 \text{ GeV} & \text{for other data ,} \end{cases}$$

where E_{SHC} is the total energy deposited in the SHC; energies of the "non-good" SHC clusters are included in the sum. This cut is to adjust the efficiency of the second cut of the filter, $E_{SHC} > 2.8$ GeV, which is done with a preliminary SHC calibration. We used a 3 GeV cut for 50 and 52 GeV data because when those data were filtered a more accurate SHC calibration was available.

We used slightly different set of cuts for different running periods. The differences and the run periods that they correspond to are summarized as:

HADCUT#1 $E_{SHC} > 3$ GeV, no $\cos\theta_{cluster}$ cut, no CDC curler cut
for run periods #02 and #03;

HADCUT#2 $E_{SHC} > 5$ GeV, no $\cos\theta_{cluster}$ cut, no CDC curler cut
for run periods #04 ~ #08;

HADCUT#4 $E_{SHC} > 5$ GeV, $|\cos\theta_{cluster}| < 0.73$, with CDC curler cut
for run periods #09 ~ #22 .

HADCUT#3 is HADCUT#4 with an additional cut on the jet invariant mass for rejecting $\tau^+\tau^-$ backgrounds more efficiently; we did not use HADCUT#3 because we found that it rejects some real hadronic events.

In Fig. 4.3, we show the distributions of the cut variables both for experimental and MC data. The data presented in the figure are selected with all cuts other than that for the variable being plotted. From these figures one can see that our choice of cut values eliminates background events with a minimal loss of hadronic events.

4.3 Background Estimates

Computer-generated event displays of all events that passed the final selection cuts were scanned by physicists to reject obvious backgrounds from beam-wall, radiative Bhabha, and cosmic ray events. Such background events are quite distinctive and easily identified in the scan; examples events corresponding to the three types of backgrounds listed above are shown in Fig. 4.4, Fig. 4.5, and Fig. 4.6, respectively. Low-energy charged tracks from beam-wall interactions are sometimes misreconstructed so that they appear as high-momentum tracks that come from the beam-interaction point; occasionally electronic noise results in fake high energy SHC clusters. The radiative Bhabha events that we removed have two high-momenta tracks overlapping the SHC clusters and low momenta tracks that often make curlers. The charged tracks in cosmic ray events actually can be seen to originate outside of the CDC. Typically less than 2% of events that pass the final selection criteria are rejected as backgrounds by the scan. We assign 10% of this fraction (*i.e.*, 0.2%) as the systematic error introduced by the scan.

Other types of background events: beam-gas interaction, $\tau^+\tau^-$ events, and two-photon hadronic events, are not always distinguishable from hadronic events by a visual scan. The fraction of these background events in the hadronic event sample are estimated and subtracted as described in the following.

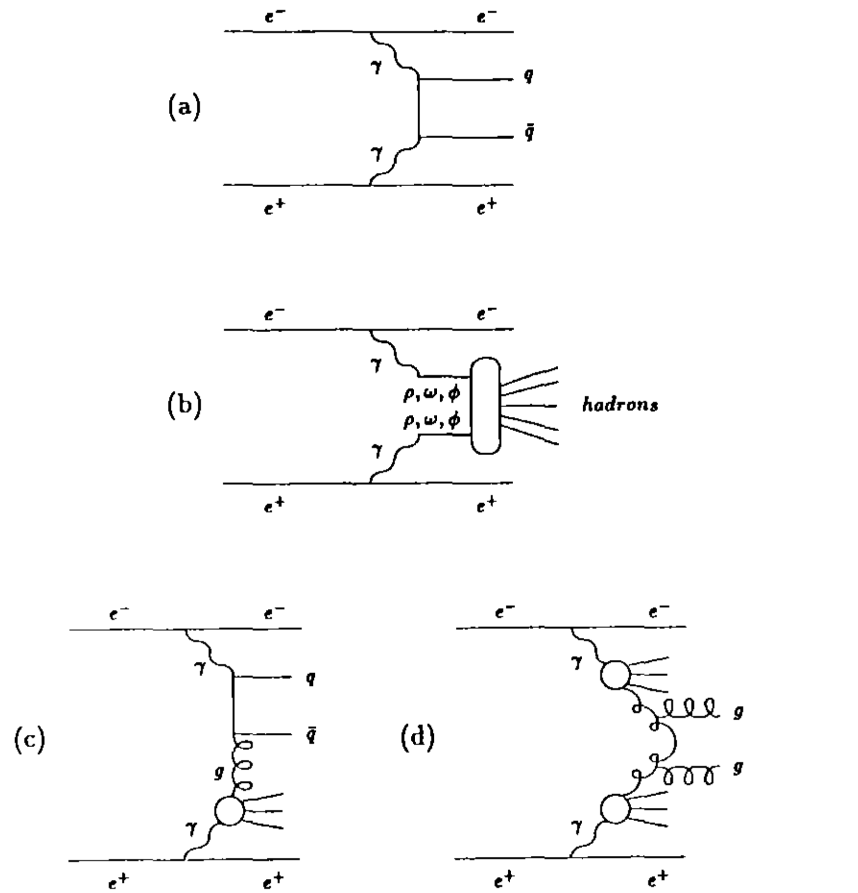

Figure 4.2: Diagrams for two-photon hadron production processes (a) QPM, (b) VMD, and examples of (c) 3-jet and (d) 4-jet multi-jet.

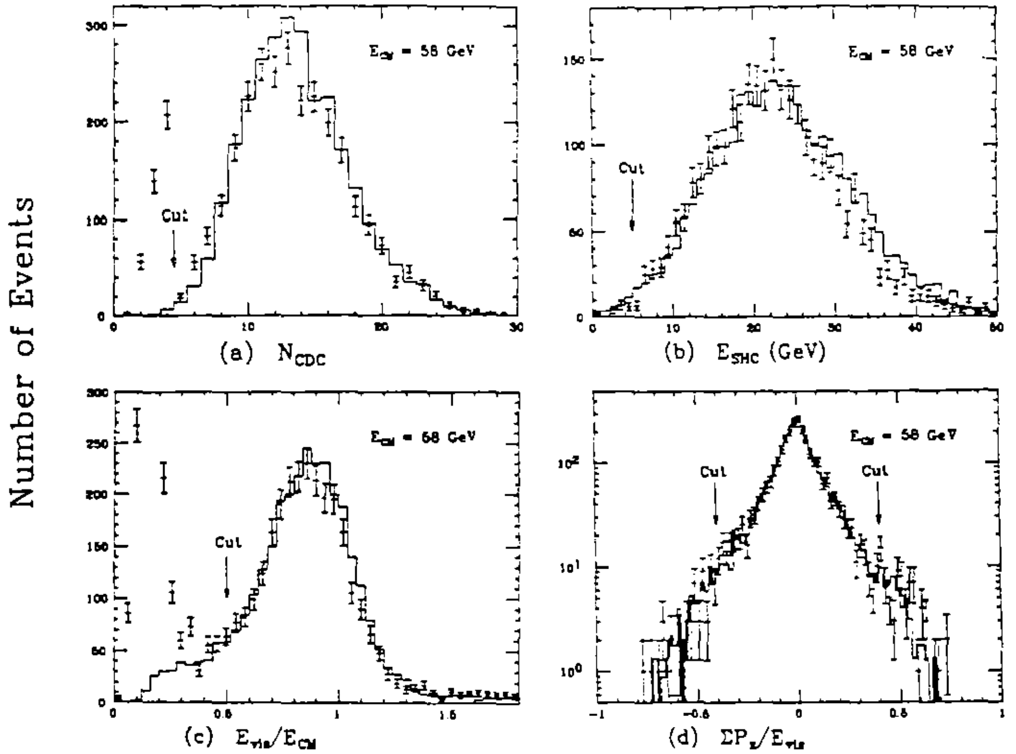

Figure 4.3: Distributions of the event cut variables: (a) N_{CDC}; (b) E_{SHC}; (c) E_{vis}/E_{CM}; and (d) $\sum P_z/E_{vis}$. Both the real data (points) and the LUND 7.3 MC data (histograms) are selected with all other cuts except the ones for the distributions.

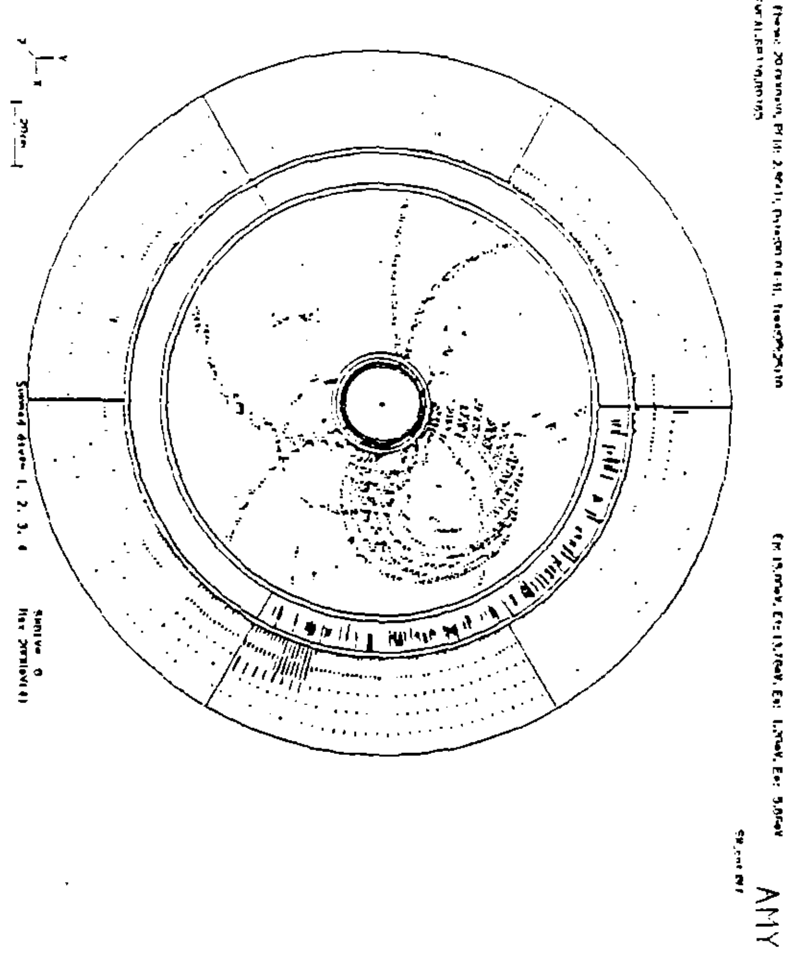

Figure 4.4: A beam-wall event rejected by the scan.

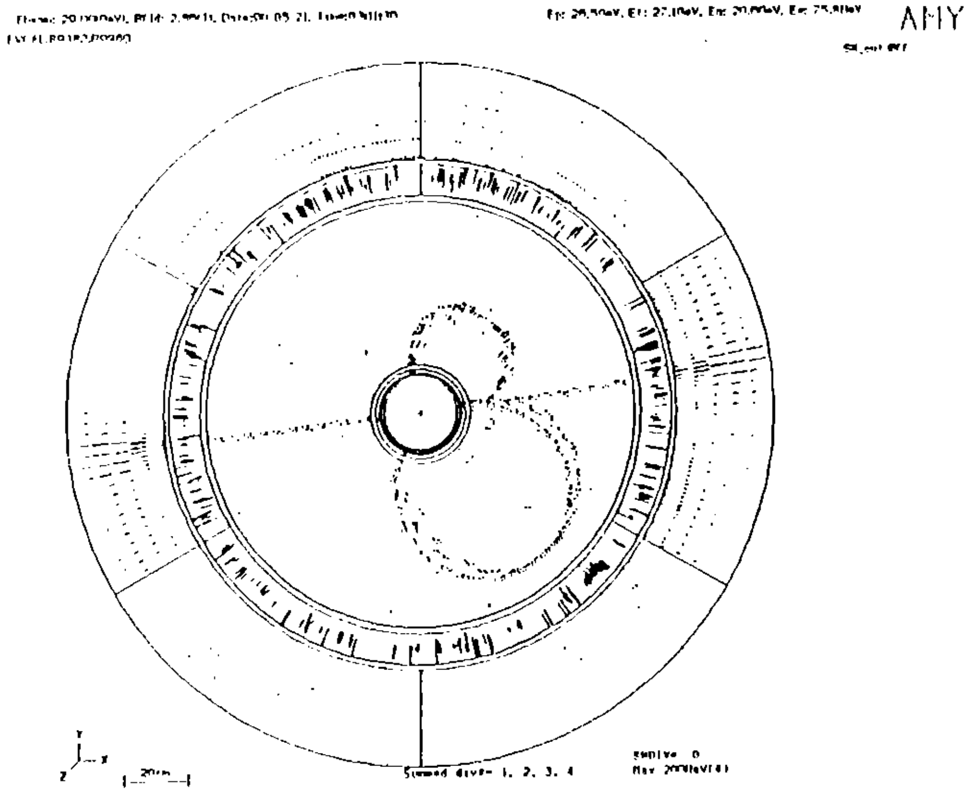

Figure 4.5: A radiative Bhabha event rejected by the scan.

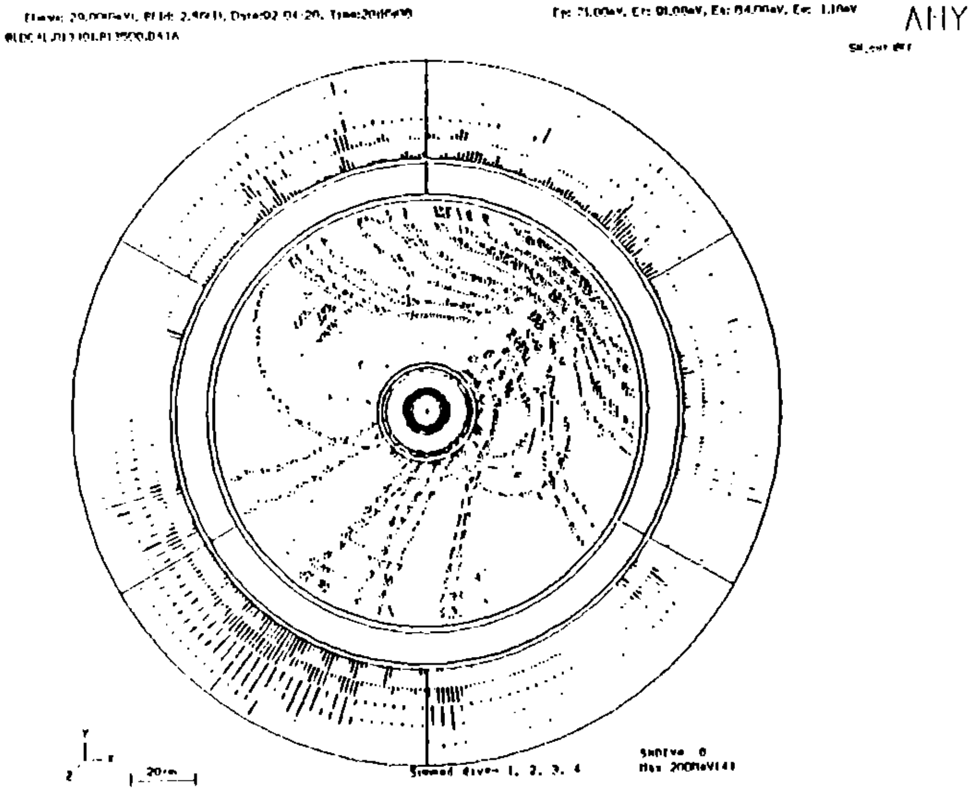

Figure 4.6: A cosmic ray event rejected by the scan.

Beam-gas interactions can occur up- and down-stream of the beam interaction point. We estimated the magnitude of this background by changing the vertex cut on CDC tracks in the final selection criteria to select tracks that originate from outside the interaction point, *i.e.*, region $15\ cm < |Z_0| < 30\ cm$. No events in the "pre-hadron" sample for $\int Ldt = 60.7pb^{-1}$ passed this "off-vertex" selection. The corresponding 95% confidence-level Poisson upper limit (3 events) gives a contamination of 0.05%. Thus, the contamination of beam-gas events in the final hadron sample is deemed to be negligible.

Background contaminations from $\tau^+\tau^-$ and two-photon hadronic events are estimated using Monte Carlo simulations. Monte Carlo simulations of fake multihadron events originating from the $e^+e^- \rightarrow \tau^+\tau^-$ process generated by the program of Fujimoto and Shimizu (FS) [30] indicate center-of-mass energy dependent contaminations of 0.7~0.9%. For two photon reactions, we consider three processes: hadronic (Vector Meson Dominance model) [31], $\gamma\gamma \rightarrow$ 2 jets (Quark Parton Model) [32] and $\gamma\gamma \rightarrow$ multi-jets [33]. Diagrams of these processes are shown in Fig. 4.2. These yield individual contaminations of 0.10~0.13%, 0.15~0.18%, and 0.07~0.08%, respectively. The background subtraction uncertainty for $\tau^+\tau^-$ production and two-photon processes is estimated to be 0.3%. This includes variation between different detector simulators, and the effects of the uncertainty of the total cross section for two-photon processes.

4.4 Detection Efficiency

The detection efficiency for multihadron annihilation events is the product of the detector acceptance (ϵ_{det}) and the efficiencies of the event selection criteria (ϵ_{sel}), the triggers (ϵ_{trig}), and the data acquisition system (ϵ_{data}).

The product of the detector acceptance and the efficiency of the event selection criteria ($\epsilon_{det} \times \epsilon_{sel}$) for multihadron annihilation events, hereafter referred to as ϵ, was determined by means of a Monte Carlo simulation. Hadronic events were generated with the LUND JETSET Ver. 7.3 (LUND 7.3) [34] Parton Shower program (PS). The PS program generates showers of quarks and gluons in a cascade process where each parton branches into two partons ($q \rightarrow qg$, $g \rightarrow gg$, $g \rightarrow q\bar{q}$) using branching probabilities calculated in the leading logarithm approximation of QCD, as given by the Altarelli-Parisi equations [36]. This cascade proceeds until

the parton virtual mass reaches a cut-off value (taken to be 1 GeV), at which stage hadrons are formed by means of the string fragmentation (SF) model [37]. In the SF model, hadrons are produced from partons via the breaking of color flux tubes that are stretched between opposite color charges. Studies of the charged multiplicity, global event shapes, inclusive charged particle spectra, and particle flow distributions for the same events used for the results reported here show quite good agreement with the predictions of the LUND PS program [38, 39].

Events produced by the generator are passed through a series of Monte Carlo computer programs that simulate the response of the AMY detector. Electromagnetic showers initiated by photons and electrons are modeled with the EGS4 program [23] and hadron showers are modeled by the GHEISHA7 program [40]. The drift chamber response is smeared with a resolution function determined by matching the track residual distributions for Monte Carlo events to those observed in the real data. The response of the detector elements is converted into a form identical to the actual data records. Simulated data and real data are subjected to the same analysis programs. We determine $\epsilon \equiv \epsilon_{det} \times \epsilon_{sel}$ from the fraction of simulated PS events that pass our event selection criteria. Approximately 2000 MC simulated multi-hadron events were scanned by physicists using the same acceptance criteria used for the actual data sample. None of the simulated events were rejected. Finally, the ϵ's are estimated to be $\epsilon = 0.649$ for HADCUT#1, $\epsilon = 0.644$ for HADCUT#2, and $\epsilon = 0.632$ for HADCUT#4, with almost no dependence on $\sqrt{s}$ in TRISTAN energy region.

The detection efficiency is also affected by data recording failures (ϵ_{data}). For example, poor running conditions of the storage ring occasionally caused high voltage trips that disabled the CDC for short periods of time without interrupting the luminosity measurement in the PTC or ESC. We have determined the number of Bhabha events in the SHC that have no corresponding CDC tracks because of these failures and also the number of Bhabha events in the PTC or ESC that occurred while the high voltage was off in more than 15 layers of the CDC. From these tallies we estimate that the detection efficiency should be decreased by 0.0~0.9% for data with center-of-mass energies other than 54, 63.6, 64 GeV. The fraction of data taking failures are estimated to be 5.0%, 6.0%, and 2.5% for 54 GeV, 63.6 GeV, and 64 GeV data respectively, which were taken under particularly poor beam conditions.

The trigger efficiency is estimated by comparing the response of different, redundant, triggering systems as described in 4.2.1. Since this is estimated to be better than 99.7%, no correction for trigger efficiency is applied to the detection efficiency. (*i.e.*, $\epsilon_{trig} = 1.00$.)

The estimation of the detection efficiency relies heavily on the MC simulations. As we mentioned above, we used LUND 7.3 with parton shower (PS) and string fragmentation (SF) for event generation. We also generated events with matrix element (ME) [35] + SF and PS + independent fragmentation (IF) [41] to estimate scheme and fragmentation dependence of ϵ. We got 0.7% difference in ME+SF and 0.9% difference in PS+IF from PS+SF. We assigned these differences as a systematic error.

Another source of systematic error in the determination of ϵ arises from differences between the detector simulation and the actual detector responses. For example, the energy distribution of SHC clusters in MC and real events has some discrepancy, even after careful calibrations. If we recalibrate the cluster energy in order to force agreement, which is rather unphysical since this results in a discrepancy in the energy of Bhabha events, ϵ changes by about 1.0%. We use this as the systematic error due to the modeling of the response of the SHC.

We also estimate the systematic error due to the choice of the selection criteria. We changed the cut values of the selection criteria (N_{CDC}, $E_{vis}/\sqrt{s}$, $|\sum P_z|/E_{vis}$, and E_{SHC}), applied them to both real events and MC events, and determined how it changed the R-values. By summing up the variations due to the changes of four variables, we estimated the error due to the selection criteria to be 1.5%.

4.5 Radiative Corrections

As described in Chapt. 2, the R value is defined to contain only the Born-term cross section in electro-weak sector, but includes all higher-order QCD processes. Experimentally, we cannot separate higher-order processes involving radiative photons ($e^+e^- \to q\bar{q} + \gamma(+\gamma...)$) and/or virtual effects (loop diagrams) from the tree level processes. Thus, we need to determine the radiative correction factor $1+\delta$, which relates the full, measured, cross section σ_{full}, which includes all higher-order

processes, to the Born cross section σ_{Born} as

$$\sigma_{full} = \sigma_{Born} \cdot (1+\delta) \ . \tag{4.2}$$

The radiative corrections are calculated order-by-order. Complete calculations have been performed up to $O(\alpha^3)$, *i.e.*, first order corrections to the tree level process. $O(\alpha^4)$ cross sections are also calculated for some special diagrams.

The radiative corrections can be categorized into two parts, photon bremsstrahlung and virtual corrections. The bremsstrahlung diagrams are obtained by adding a real photon to the external lines of the lowest-order diagrams as shown in Fig. 4.7 (a) and (b). These diagrams and interference between them give $O(\alpha^3)$ contributions. The virtual corrections are obtained by adding loops to the internal lines (vacuum polarization), or adding internal gauge boson lines to external lines (vertex corrections and box diagrams) as shown in Fig. 4.7 (c)~(i). These diagrams are of $O(\alpha^4)$ but their interference with the lowest order diagrams give $O(\alpha^3)$ contributions.

Virtual QED corrections with an additional virtual photon line added to the lowest-order diagrams diverge as $k \equiv E_\gamma/E_{beam} \to 0$, where E_γ is energy of the photon and E_{beam} is the beam energy. Photon bremsstrahlung corrections also diverge both at $k \to 0$ and $k \to 1$. Soft photons with $k \simeq 0$ are not detectable because they are emitted along electron or positron beam and escape to the beam pipe, and/or have energies which are below the detectable level. Therefore, the bremsstrahlung corrections are split into two parts, an infrared divergent/non-detectable "soft" photon part, and a finite/detectable "hard" photon part. The divergences from the virtual corrections are exactly cancelled with the $k \to 0$ divergences from photon bremsstrahlung. Thus, only the divergence as $k \to 1$ in the hard photon bremsstrahlung remains. This divergence occurs because the effective center-of-mass energy squared, $s' = s(1-k)$, approaches zero, where the hadronic cross section diverges as $1/s'$. Since hadronic events must have at least two pions in the final state, the maximum value of k is $1 - 4m_\pi^2/s$, and there is, in fact, no divergence. Moreover, events with $k \simeq 1$ cannot pass the hadronic selection criteria because of the large amount of energy carried by the radiative photon. Therefore, the hard photon radiative corrections also remains finite. We set k_{max}, the maximum value of k, to 0.99 since the probability for events with $k > 0.99$ to pass the hadronic event selection cuts is negligible.

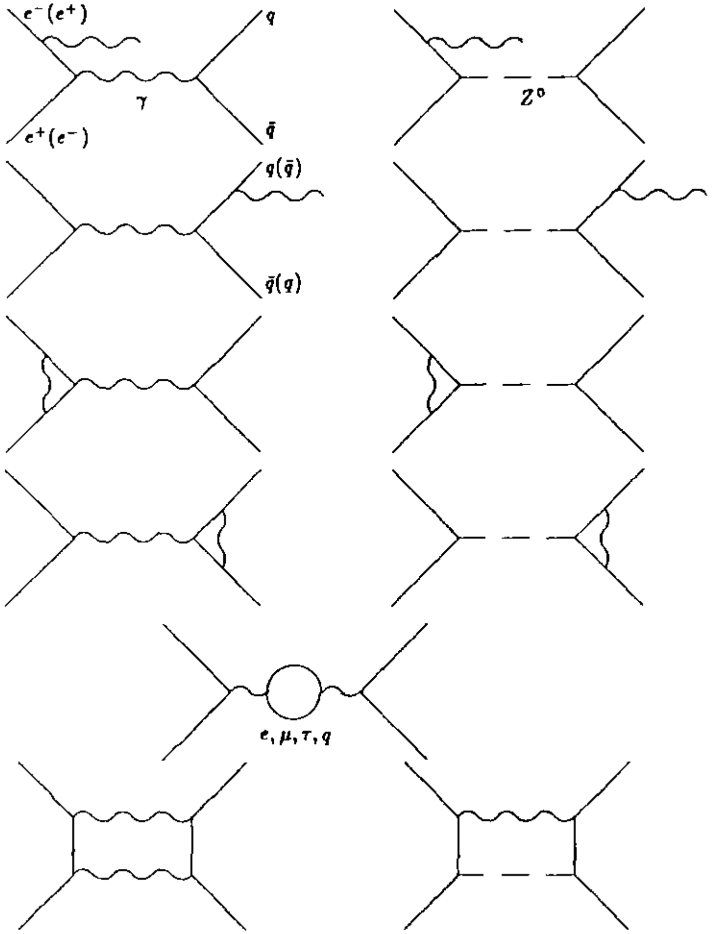

(a)

(b)

(c)

(d)

(e)

(f)

Figure 4.7: Diagrams of (a) initial state radiation, (b) final state radiation, (c) initial state QED vertex corrections, (d) final state QED vertex corrections, (e) QED vacuum polarization, and (f) QED box diagrams. (continued to the next page)

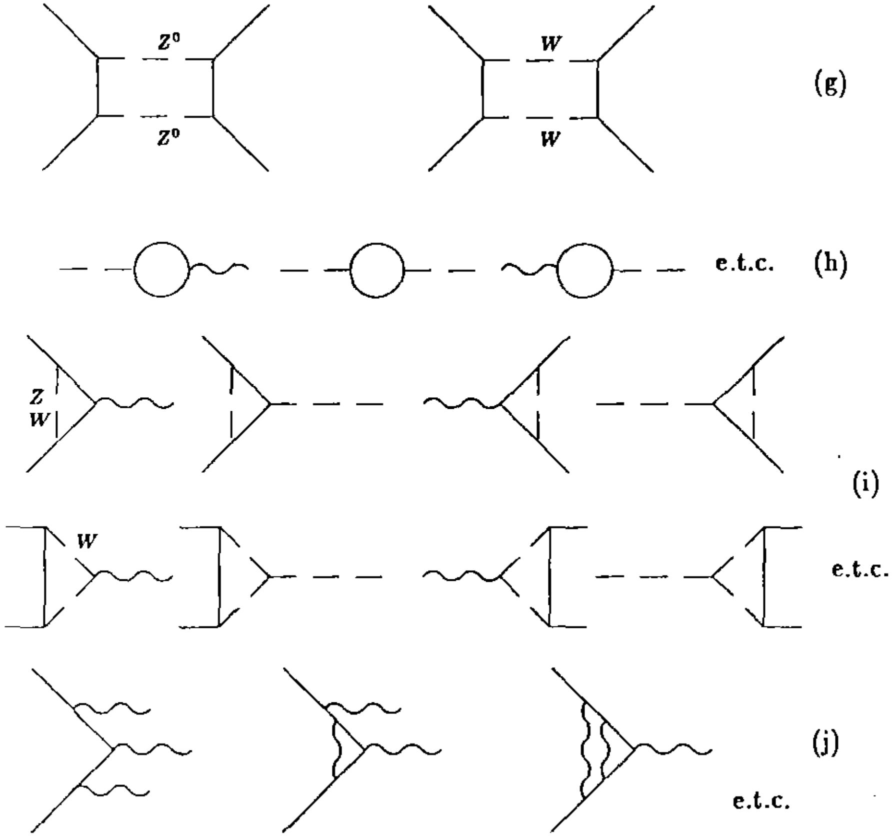

(g)

(h)

(i)

(j)

Figure 4.7: (continuing from the previous page) Diagrams of (g) weak box diagrams, (h) electroweak vacuum polarization, (i) electroweak vertex corrections, and (j) higher order QED initial state corrections.

We compared the results of three programs for calculating radiative corrections: LUND JETSET Ver. 6.3 (LUND 6.3), Fujimoto-Shimizu (FS) [30], and ZSHAPE [42]. LUND 6.3 includes radiative corrections using methods developed by Berends, Kleiss and Jadach (BKJ) [43] as well as LUND 7.3, which is used to determine the detection efficiency. The BKJ calculation includes initial state radiation, initial state vertex corrections for both γ and Z^0 propagators, and QED vacuum polarization terms ((a),(c), and (e) in Fig. 4.7), but does not include all box diagrams, nor the full electroweak vertex corrections and vacuum polarization terms. The BKJ calculations have been widely used by many PEP and PETRA experiments. The FS program includes complete electroweak radiative corrections of $O(\alpha^3)$ ((a)~(i) in Fig. 4.7). We used the FS calculation in our previous analyses [44].

ZSHAPE omits box diagrams and interferences of real photon bremsstrahlung[1] but includes some of higher order corrections. In ZSHAPE, radiative corrections are categorized into two parts, QED corrections (δ_{QED}) and electroweak corrections (δ_{EW}). The QED corrections consist of real photon bremsstrahlung and vertex corrections for virtual photons ((a)~(d) in Fig. 4.7), while the electroweak corrections consist of vertex corrections for weak propagators and vacuum polarizations of both γ and Z^0 propagators ((e),(h),and (i) in Fig. 4.7). Then ZSHAPE program calculates radiative corrections as

$$1+\delta_{ZSHAPE} = (1+\delta_{QED})(1+\delta_{EW}) \ , \tag{4.3}$$

while FS calculates them as

$$1+\delta_{FS} = 1+\delta_{QED}+\delta_{EW} \ . \tag{4.4}$$

The cross term, $\delta_{QED}\cdot\delta_{EW}$, corresponding to higher order corrections, results in a few percent difference between ZSHAPE and FS. Additionally, ZSHAPE includes $O(\alpha^2)$ corrections to initial state (Fig. 4.7(j)) and exponentiated expressions for initial and final radiation. The exponentiation is a technique to handle the infrared divergences of both real and virtual QED corrections. In soft photon limit, infinite number of real and virtual photons are emitted. These contributions can be "exponentiated" by summing up leading term of each order without explicit higher order calculations [45].

[1] The authors of ZSHAPE claim their contribution is order of 0.1%~0.2% in the energy range of PEP, PETRA, TRISTAN, and LEP. We assign 0.2% as a systematic error

The radiative corrections are strongly dependent on the Z^0 boson mass (M_{Z^0}), the top quark mass (M_t), and the Higgs boson mass (M_{H^0}). We chose these masses as M_{Z^0} = 91.16 GeV, M_t = 150 GeV, and M_{H^0} = 100 GeV, respectively.

Calculations of the radiative correction factor for k_{max} = 0.99 by the three programs described above are shown in Fig. 4.8 as functions of center-of-mass energy. ZSHAPE is used in two different ways. One is for $O(\alpha^3)$ including the cross term $\delta_{QED}\cdot\delta_{EW}$. The other is for the higher order corrections including initial state QED corrections of $O(\alpha^2)$ and exponentiations of both initial and final state QED corrections. BKJ is also used with two different set of parametrizations, the default one and M_{Z^0} = 92 GeV, M_t = 45 GeV, and M_{H^0} = 100 GeV, a typical set of values in pre-LEP days; publications from PEP and PETRA used similar parametrizations. This figure shows that ZSHAPE gives results for $1+\delta$ that are higher than those from FS by 2.1 ~ 2.5% (for $O(\alpha^3)$) or 2.7 ~ 3.3% (for higher order corrections).

Therefore, the R value results are lower by a few percent if ZSHAPE is used instead of FS. However, what is really needed for the R value calculation is not $1+\delta$ itself but the quantity $\epsilon(1+\delta)$. Even if $1+\delta$ is large at very high k, where ϵ is small, $\epsilon(1+\delta)$ does not change. To see this effect clearly, we introduce the new k-dependent variables $\epsilon(k)$, the product of detector acceptance and efficiency of the selection criteria, and $\partial(1+\delta)/\partial k = \sigma(k)/\sigma_{Born}$, the differential radiative correction, for events with radiative photon energy $k\cdot E_{beam}$. These are related to ϵ and $1+\delta$ as

$$\epsilon = \frac{\int_0^{k_{max}} \epsilon(k)\sigma(k)dk}{\int_0^{k_{max}} \sigma(k)dk}, \tag{4.5}$$

$$1+\delta = \int_0^{k_{max}} \frac{\partial(1+\delta)}{\partial k}dk = \int_0^{k_{max}} \frac{\sigma(k)}{\sigma_{Born}}dk \ . \tag{4.6}$$

Figs. 4.9 and 4.10 show $\epsilon(k)$ determined using LUND7.3 and $\partial(1+\delta)/\partial k$ calculated by ZSHAPE. In the determination of the R value we make the replacement

$$\epsilon(1+\delta) \Rightarrow \int_0^{k_{max}} \epsilon(k)\frac{\partial(1+\delta)}{\partial k}dk. \tag{4.7}$$

Hereafter we refer to the two forms as $\epsilon\cdot(1+\delta)$ and $\int\epsilon(1+\delta)$. They are identical when we use same radiative corrections to determine ϵ and $1+\delta$. However, in our case, we use LUND7.3, which adopts BKJ calculation, to estimate ϵ but ZSHAPE for calculating $1+\delta$, and we need to use $\int\epsilon(1+\delta)$ as $\epsilon(1+\delta)$. In our previous

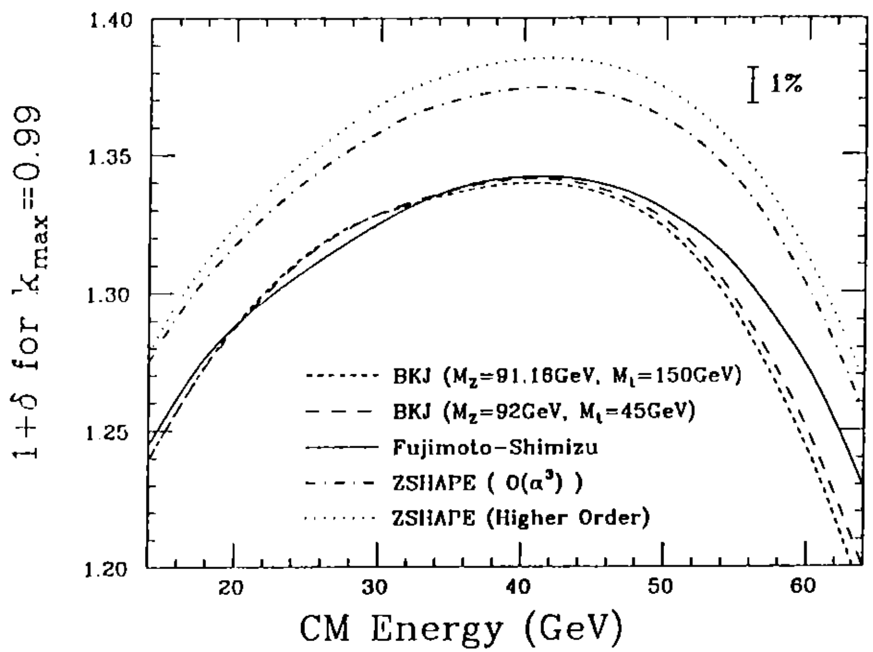

Figure 4.8:
Radiative correction factors for $k_{max} = 0.99$, calculated by BKJ (short-dashed line with $M_{Z^0} = 91.16$ GeV and $M_t = 150$ GeV, long-dashed line with $M_{Z^0} = 92$ GeV and $M_t = 45$ GeV); FS (solid line); and ZSHAPE (dot-dashed line for $O(\alpha^3)$, dotted line for higher order corrections and exponentiatons).

analyses [44], we used LUND6.3 for ϵ and FS for $1+\delta$ but simplly multiplied them to get $\epsilon \cdot (1+\delta)$ as $\epsilon(1+\delta)$.

The results of the calculation of $\epsilon(1+\delta)$ are shown in Table 4.3 for different center-of-mass energies. One can see that the $\int\epsilon(1+\delta)$ values are lower than $\epsilon \cdot (1+\delta)$ values at $\sqrt{s} < 63.6$ GeV, almost canceling the differences between FS and ZSHAPE at energies around 58 GeV, where most of our data are taken. In this study, we assumed that $\epsilon(k)$ only depends on k and not on the virtual corrections because virtual corrections do not change the topology of events. This assumption insures the validity of using LUND7.3 to estimate $\epsilon(k)$. It is, in fact, not true when we consider the higher order corrections of ZSHAPE, which includes multiple real photon emission. We use $\int\epsilon(1+\delta)$ for $O(\alpha^3)$ to calculate R values and assign the difference from the higher order corrections ($\simeq 0.2\%$) as a systematic error.

In the following chapters, we use published data from other experiments in PEP, PETRA, and TRISTAN. Their radiative corrections are not calculated as same as we did above. We correct data of other TRISTAN groups, TOPAZ and VENUS, by assuming the shapes of their $\epsilon(k)$'s are same as that for the AMY detector. We also need to correct PEP and PETRA data using radiative corrections calculated by ZSHAPE. However, we need to have simulators of their detectors to follow the procedures that we used for AMY. Fig. 4.8 shows that the differences between BKJ and FS are small in their energy range even if pre-LEP parameters are used. Additionally, the difference between FS and ZSHAPE tends to be canceled when we calculate $\epsilon(1+\delta)$ as we have seen in the case of AMY. Thus, we decided not to correct PEP and PETRA data for ZSHAPE's radiative corrections. We verified this by simulating hadronic events in AMY detector at PEP and PETRA energies.

To calculate $1+\delta$, we use a top quark mass of 150 GeV; if we use M_t = 100(200)GeV, the results change by +0.4%(−0.6%) at $\sqrt{s} = 60$ GeV. For the Higgs-boson mass we use 100 GeV; if we take it to be 50 (1000) GeV, the results change by −0.1%(+0.3%) at $\sqrt{s} = 60$ GeV. These variations are smaller for the lower center-of-mass energies. We assign 0.7% as a systematic error due to uncertainty of M_t and M_H.

There is another uncertainty in the calculation of the hadronic vacuum polarization due to the unknown masses of the light quarks (u and d). We varied the light quark masses over a reasonable range and estimated the systematic error to be 0.4%.

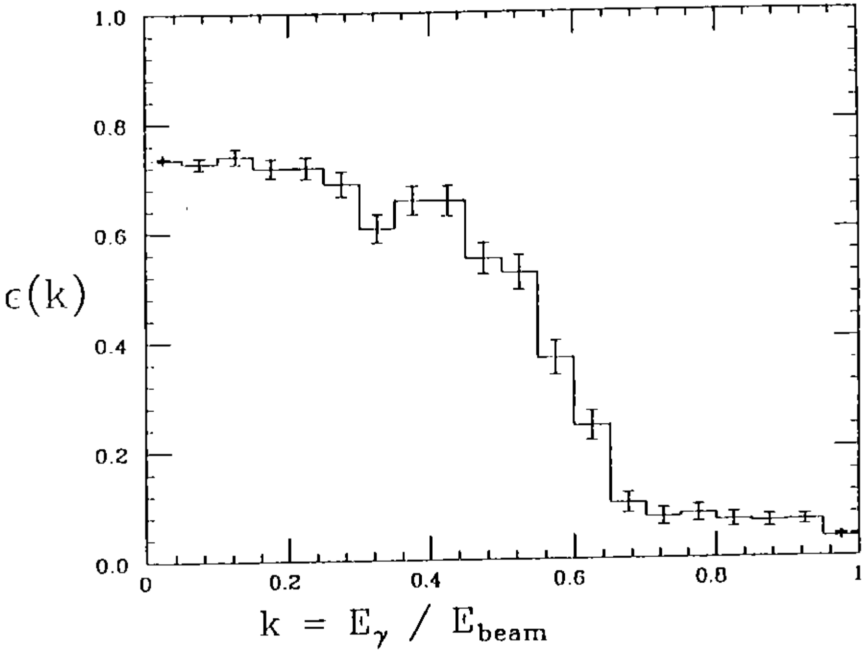

Figure 4.9: Detection efficiencies ($\epsilon_{det} \times \epsilon_{sel}$) as a function of k, the energy of the initial state radiative photon normalized to the beam energy, estimated with LUND 7.3 at $E_{CM} = 58$ GeV.

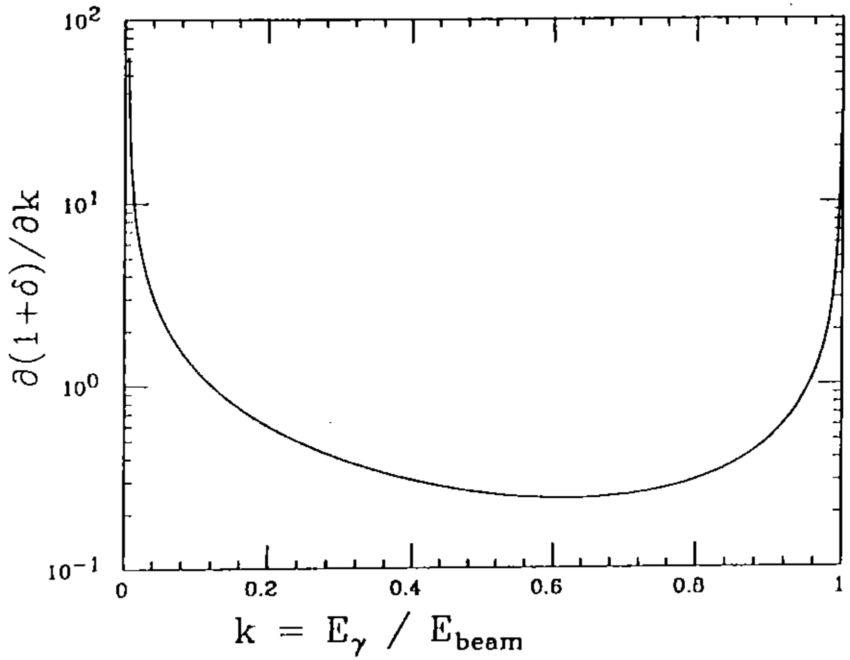

Figure 4.10: The differential radiative correction factors as a function of k, calculated by ZSHAPE with $O(\alpha^3)$ corrections.

$\sqrt{s}$		FS		ZSHAPE		
(GeV)	ϵ	$1+\delta$	$\epsilon\cdot(1+\delta)$	$1+\delta$	$\epsilon\cdot(1+\delta)$	$\int\epsilon(1+\delta)$
50	0.649	1.336	0.867	1.365	0.885	0.856
52	0.649	1.329	0.862	1.357	0.880	0.853
54	0.632	1.320	0.834	1.346	0.851	0.829
55	0.644	1.314	0.847	1.340	0.864	0.842
56	0.644	1.307	0.843	1.333	0.859	0.840
56.5	0.644	1.304	0.841	1.329	0.857	0.839
57	0.644	1.300	0.838	1.325	0.854	0.837
58	0.632	1.293	0.817	1.316	0.832	0.818
58.5	0.632	1.288	0.814	1.312	0.829	0.817
59	0.632	1.284	0.811	1.307	0.826	0.815
59.05	0.632	1.283	0.811	1.306	0.826	0.815
60	0.632	1.274	0.805	1.296	0.819	0.811
60.8	0.632	1.266	0.800	1.287	0.814	0.808
61.4	0.632	1.260	0.796	1.280	0.809	0.806
63.6	0.632	1.233	0.779	1.251	0.791	0.795
64	0.632	1.228	0.776	1.245	0.787	0.793

Table 4.3: A summary of the calculations of $\epsilon(1+\delta)$ in three different ways. ZSHAPE is used with $O(\alpha^3)$ corrections.

We set $k_{max} = 0.99$ instead of $1 - 4m_\pi^2/s \simeq 0.99998$, mainly to save computer time. To check the validity, we simulated 1,000 events for $0.99 < k < 0.999$ and determined ϵ for these events to be 0.016 ± 0.004. Radiative corrections for $0.99 < k < 1 - 4m_\pi^2/s$ are calculated to be

$$\int_{0.99}^{1-4m_\pi^2/s} \frac{\partial(1+\delta)}{\partial k} dk = 0.1562 \tag{4.8}$$

by ZSHAPE at $\sqrt{s} = 58$ GeV. Thus, $\Delta\epsilon(1+\delta)$ is estimated to be

$$\int_{0.99}^{1-4m_\pi^2/s} \epsilon(k)\frac{\partial(1+\delta)}{\partial k} dk < 0.0025, \tag{4.9}$$

since $\epsilon(k)$ is even smaller for $k > 0.999$. This contribution is about 0.3% of $\epsilon(1+\delta)$ for $k_{max} = 0.99$. We include this in the systematic error as well.

4.6 Systematic Errors

All energy-independent systematic errors mentioned above are listed in Table 4.4. By adding them in quadrature, we estimate the overall normalization error to be $\pm 3.5\%$ for AMY 1.0 and $\pm 2.8\%$ for AMY 1.5.

The energy-dependent systematic errors (point-to-point systematic errors) consist of the errors associated with the luminosity measurement and the data-recording failures (ϵ_{data}). The luminosity errors are due to the statistics of the number of Bhabha events and the systematic error for correction of dead sections of PTC and ESC. The error of ϵ_{data} is due to the statistics of Bhabha events detected by SHC, PTC, or ESC, we used to estimate ϵ_{data}. The point-to-point systematic errors are summarized in Table 4.5 for each run period.

4.7 Results

The results of the R measurements are summarized in Table 4.6. The errors listed with the R values are point-to-point errors, *i.e.*, the statistical errors and the point-to-point systematic errors. There is additional overall normalization error of 3.5% for AMY 1.0 and 2.8% for AMY 1.5. The R_{theory} values are the theoretical predictions for $M_{Z^0} = 91.173$ GeV, $\sin^2\theta_W = 0.2259$, and $\Lambda_{\overline{MS}}^{(5)} = 0.175$ GeV [47]. The R values for the 50~61.4 GeV data (except 58 GeV data) are slightly different

Systematic Errors	(%)	
(Luminosity)	(AMY 1.0)	(AMY 1.5)
rad. correction, acceptance	1.3	0.41
background	0.2	0.04
trigger efficiencies	0.2	0
chamber efficiencies	0.1	0.05
alignment	2.0	1.22
(Radiative Corrections)		
k_{max} dependence	0.3	
interference, box diagrams	0.2	
higher order corrections	0.2	
M_t, M_H dependence	0.7	
quark mass dependence	0.4	
(Detecion Efficiency)		
MC statistics	0.8	
MC scheme	0.7	
fragmentation	0.9	
event selection cut	1.5	
SHC response	1.0	
(Background)		
$\tau\tau$, two-photon	0.3	
visual scan	0.2	
Total	3.5	2.8

Table 4.4: A summary of the overall normalization systematic errors.

$\sqrt{s}$ (GeV)	point-to-point systematic errors (%) Luminosity Statistics	Luminosity Dead Section	Data Recording Failure	Total
50	2.5	0.0	$^{+0.94}_{-0.00}$	2.8
52	1.1	1.7	0.13	2.2
54	3.2	0.8	0.56	3.4
55	1.2	0.0	0.17	1.4
56	0.9	0.0	0.15	1.1
56.5	2.2	0.0	0.90	2.5
57	1.1	0.0	0.34	1.3
58	0.2	0.01	0.01	0.2
58.5	2.0	0.0	0.08	2.0
59	2.8	0.0	0.11	2.8
59.05	2.6	0.0	$^{+0.15}_{-0.00}$	2.6
60	1.2	0.0	0.08	1.3
60.8	1.5	1.1	0.07	1.9
61.4	1.2	0.6	0.09	1.4
63.6	2.4	0.0	0.41	2.4
64	1.6	0.0	0.18	1.6

Table 4.5: A summary of the point-to-point systematic errors.

from previously reported results [44], reflecting the different scheme of calculating $\epsilon(1+\delta)$.

The R measurements are shown in Fig. 4.11, where the solid line is the theoretical prediction. Here, the error bars in the figure represent total statistical, point-to-point systematic, and overall normalization errors added in quadrature.

$\sqrt{s}$	$\int Ldt$		N_{bkg}				$\sigma_{\mu\mu}$		
(GeV)	(pb^{-1})	$N_{selected}$	$\tau\tau$	2γ	ϵ_{data}	$\epsilon(1+\delta)$	(pb)	R	R_{theory}
50	0.636	88	0.7	0.3	1.000	0.856	34.7	4.60 ± 0.51	4.21
52	3.976	482	4.3	1.6	0.997	0.853	32.1	4.38 ± 0.22	4.32
54	0.531	61	0.5	0.2	0.950	0.829	29.8	4.84 ± 0.65	4.47
55	3.266	368	3.0	1.3	0.997	0.842	28.7	4.62 ± 0.25	4.56
56	5.993	727	5.4	2.4	0.996	0.840	27.7	5.18 ± 0.20	4.65
56.5	0.994	123	0.9	0.4	0.997	0.839	27.2	5.38 ± 0.51	4.71
57	4.398	492	3.9	1.8	0.997	0.837	26.7	4.96 ± 0.24	4.77
58	60.826	6053	51.1	23.1	0.998	0.818	25.8	4.66 ± 0.06	4.89
58.5	0.801	89	0.7	0.3	0.998	0.817	25.4	5.31 ± 0.58	4.96
59	0.721	80	0.6	0.3	0.997	0.815	25.0	5.41 ± 0.63	5.03
59.05	0.504	68	0.4	0.2	1.000	0.815	24.9	6.59 ± 0.82	5.04
60	3.551	405	2.8	1.4	0.993	0.811	24.1	5.81 ± 0.30	5.20
60.8	3.481	368	2.7	1.3	0.995	0.808	23.5	5.53 ± 0.31	5.34
61.4	4.287	431	3.3	1.6	0.991	0.806	23.0	5.40 ± 0.27	5.46
63.6	0.440	41	0.3	0.2	0.940	0.795	21.5	5.74 ± 0.92	6.00
64	1.097	111	0.8	0.4	0.975	0.793	21.2	6.11 ± 0.59	6.12

Table 4.6: A summary of R values. Here R_{theory} is the prediction of the standard model with $M_{Z^0} = 91.173$ GeV, $\sin^2\theta_W = 0.2259$, and $\Lambda^{(5)}_{\overline{MS}} = 0.175$ GeV. Only statistical errors and point-to-point systematic errors are shown with R values. Overall normalization error is 2.8% for 58 GeV, 63.6 GeV, and 64 GeV, 3.5% for data at other energies.

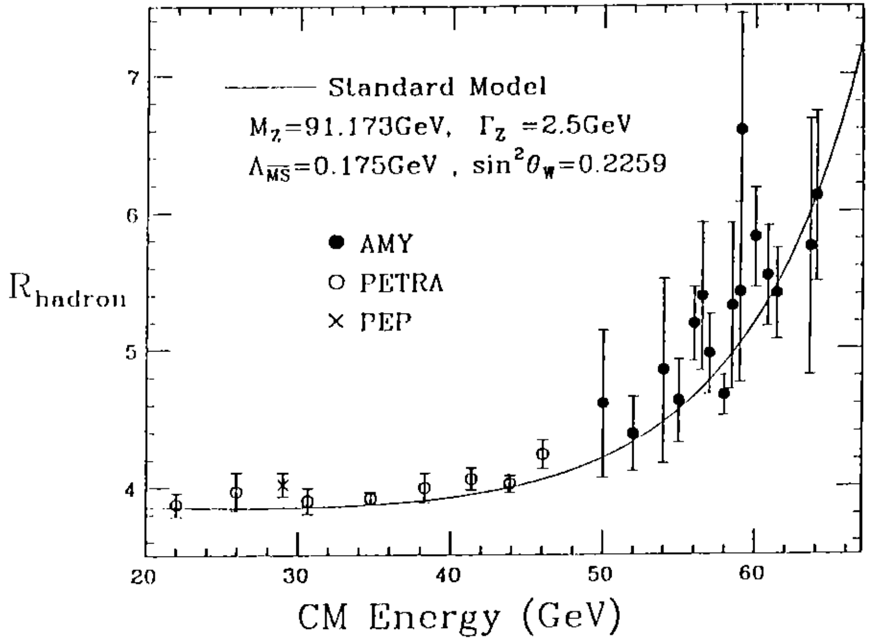

Figure 4.11: The AMY results for R values (solid circles) together with previously reported results at lower energies. The error bars include statistical and systematic errors. The data from the other experiments are combined for display purposes. The solid curve is the standard model prediction for $M_{Z^0} = 91.173$ GeV, $\sin^2\theta_W = 0.2259$, and $\Lambda^{(5)}_{\overline{MS}} = 0.175$ GeV.

Chapter 5

The Di-lepton Cross Section

In this chapter, the experimental techniques for selecting di-lepton events ($e^+e^- \to \mu^+\mu^-$ and $e^+e^- \to \tau^+\tau^-$) and determining their cross sections are summarized. Details of this analysis are provided in Ref. [46]

5.1 The Di-muon Event Selection

Di-muon events detected by the AMY detector have a simple topology, namely two back-to-back high momenta tracks, each with approximately the beam energy. The SHC energy signals should be consistent with minimum ionizing particles, and the hits in the muon chambers consistent with the extrapolated locations of the CDC tracks. Events are triggered by various combinations of ITC track segments, CDC track segments, and SHC energy signals. The triggers are enabled during the beam crossing time (Beam Gate), and for an equal time interval starting midway between the beam crossing (Cosmic Ray Gate). The gate during which the event occurs is recorded in the data record. Events that occur during the Cosmic Ray Gate are treated as same as those that occur during the e^+e^- crossing time and provide a direct measurement of the level of cosmic ray induced backgrounds.

In addition to cosmic rays, possible sources of backgrounds include: Bhabha events, two photon processes $e^+e^- \to e^+e^-\mu^+\mu^-$ of which the final state e^+e^- are not detected, $\tau^+\tau^-$ events where the τ's decay into muons, and radiative processes $e^+e^- \to \mu^+\mu^-\gamma$. To eliminate these backgrounds, we apply the following selection criteria:

(i) $N_{CDC} \leq 10$, $N_{good\ CDC} \geq 2$
where N_{CDC} is the number of CDC tracks and $N_{good\ CDC}$ is the number of "good" CDC tracks which satisfy $|R_0| \leq 0.5\ cm$, $|Z_0| \leq 3.0\ cm$, and $p \geq 0.2E_{CM}$. Note, the definition is different than that for the hadronic event selection.

(ii) $Max\text{-}p > 0.25E_{CM}$,
where $Max\text{-}p$ is the momentum of the most energetic track.

(iii) $\theta_{acol} \geq 170°$,
where θ_{acol} is the opening angle between two tracks.

(iv) $E_{SHC} \leq 0.5E_{CM}$, $E^{chg}_{clus} \leq 0.1E_{CM}$, $Max\text{-}E^{neut}_{clus} \leq 0.5E_{CM}$,
where E_{SHC} is the total energy deposited in the SHC, E^{chg}_{clus} is the energy of each shower cluster matching to the CDC track, and $Max\text{-}E^{neut}_{clus}$ is the energy of the most energetic shower cluster not matched to the CDC tracks.

(v) $N_\mu \geq 2$,
where N_μ is the number of the muon chamber hits matching to the CDC tracks.

(vi) 0 ns < T_μ < 35 ns,
where T_μ is the time of the muon counter hits relative to the beam crossing time.

(vii) −14 ns < ΔT_μ < 20 ns,
where ΔT_μ is the time difference between the two muon counter hits.

(viii) −25 ns < T_{ITC} < 25 ns,
where T_{ITC} is the time of the ITC hits relative to the beam crossing time.

Most Bhabha-induced backgrounds are rejected by criteria (iv) and (v); two photon and $\tau^+\tau^-$ events are eliminated by criteria (ii) and (iii), radiative di-muon events are rejected by criterion (iii), and cosmic ray events are reduced by crieria (i), (vi), (vii), and (viii). All events satisfying these selection criteria are visually scanned by physicists to remove obvious background events. Of all selected di-muon candidates, events satisfy $|\cos\theta| < 0.7071$ are used for the following analysis.

The fraction of background events that survive all selection criteria in the sample of the di-muon candidates is estimated as follows. The fraction of cosmic ray events is measured directly from the number of events passing the selection cuts that occured during the Cosmic Ray Gate. This corresponds to 4.9% of the final event sample that occured during the Beam Gate. We estimated the level of Bhabha backgrounds by checking the probability for tracks in the final selected Bhabha sample to match to muon chamber hits. This shows that the probability for Bhabha events to fake di-muon events is negligible. The background fraction due to each of $\tau^+\tau^-$ and $e^+e^-\mu^+\mu^-$ processes is estimated to be about 0.2% from Monte Carlo simulations of these processes. The radiative processes $e^+e^- \rightarrow \mu^+\mu^-\gamma$ can not be separated from the Born process in the soft photon limit. This effect is treated by the radiative corrections.

After the selection cuts, 510 events are selected for the integrated luminosity of $\int Ldt = 32.60\ pb^{-1}$. 5.4% of these events are estimated to be backgrounds.

5.2 Di-muon Cross Section

The differential cross section for the tree-level di-muon process is obtained from the relation

$$\frac{d\sigma}{d\Omega} = \frac{N_{selected} - N_{bkg}}{2\pi \cdot \Delta\cos\theta \cdot eff \cdot (1+\delta) \cdot \int Ldt}, \tag{5.1}$$

where the definitions of variables are same as in eq. (4.1) for the hadronic cross section, except that here the number of selected events $N_{selected}$, the number of backgrounds N_{bkg}, the detection efficiency eff, and the radiative corrections $1+\delta$ are determined separately for each $\cos\theta$ bin. We divide the range $|\cos\theta| < 0.7071$ into 12 bins, which results the bin size of $\Delta\cos\theta = 0.1178$.

The detection efficiency is the product of the selection efficiency which can be estimated with Monte Carlo simulations (ϵ_{sel}) and the trigger efficiency (ϵ_{trig}), the efficiency of the vertex cut (ϵ_{vertex}), and the efficiency of the muon chambers and counters (ϵ_{MUO}). The efficiency of the data acquisition system (ϵ_{data} in hadronic selection efficiency) is accounted in ϵ_{trig}. ϵ_{sel} is the efficiency for real events to pass the selection criteria (ii) through (v), which can be reproduced in the MC simulation. This is estimated to be about 0.75 for $|\cos\theta| < 0.7071$ using MC events generated by the FS program with full $O(\alpha^3)$ electroweak radiative corrections.

The trigger efficiency is calculated with Bhabha events that are triggered by SHC triggers that are totally independent of the triggers used for di-muon events. These events have the same charged track topology as di-muon events and can be used to monitor the efficiency of the charged track triggers. In this way, we measure $\epsilon_{trig} = 94.4\% \sim 98.7\%$ for $|\cos\theta| < 0.7071$ for differnet center-of-mass energies. Bhabha events are also used to determine that the vertex cut efficiency is 94.9% for $|\cos\theta| < 0.7071$. Cosmic ray events satisfying $|R_0| \leq 0.5\ cm$, $|Z_0| \leq 1.0\ cm$, and $P_{track} \geq 1\ GeV$, are used to estimate ϵ_{MUO}. We obtained the chamber efficiency of 0.990~0.995 for different $\cos\theta$ bins and the counter efficiency of about 0.967 for outer-most bins ($0.5893 < |\cos\theta| < 0.7071$) and 0.998 for other bins.

The radiative correction factors $1 + \delta$'s are also calculated by the FS program. In the case of di-muon events, the cross term $\delta_{QED} \cdot \delta_{EW}$ and the higher order corrections discussed in Section 4.5 are negligible because the 170° opening-angle cut rejects most hard-photon radiative processes.

The di-muon differential cross sections for the combined data for all energies are shown in Fig. 5.1.

5.3 τ Decay Modes

Final state τ leptons produced in the reaction $e^+e^- \rightarrow \tau^+\tau^-$ decay into light leptons or quarks via the weak interaction processes shown in Fig. 5.2 with a lifetime of $\sim 3 \times 10^{-13}$sec. In this figure, d_c is the Cabibbo-rotated down quark

$$d_c = d\ \cos\theta_c + s\ \sin\theta_c, \tag{5.2}$$

where θ_c is the Cabibbo angle. Note that only the production of u-, d-, and s-quarks is energetically allowed. Therefore, what we observe in our experiment are the decay products of τ's ($e^{\pm}$, $\mu^{\pm}$, or hadrons) collimated in the direction of flight of the parent τ's.

The branching ratios for various decay channels are listed in Table 5.1 [47]. It is useful to classify the decay channels by the number of charged particles among the decay products. A decay into n charged particles and an arbitrary numbers of neutral particles is called a "n-prong" decay. The branching ratio for 1-prong, 3-prong, and 5-prong decays are expected to be [47] :

$$BR(\text{1-prong}) = 85.94 \pm 0.23\ \%$$

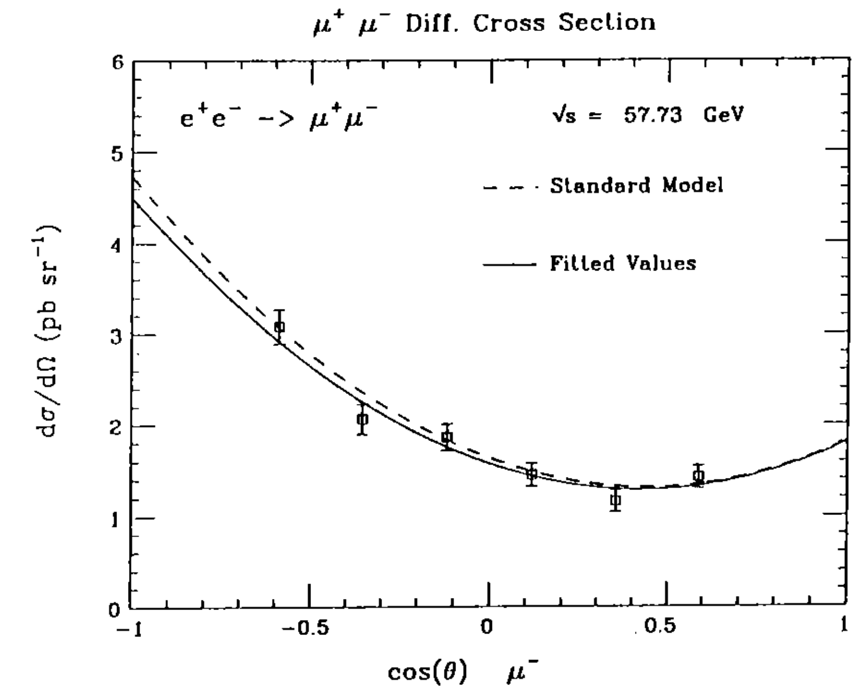

Figure 5.1: The differential cross section for $e^+e^- \rightarrow \mu^+\mu^-$ process. Data for all energies are combined.

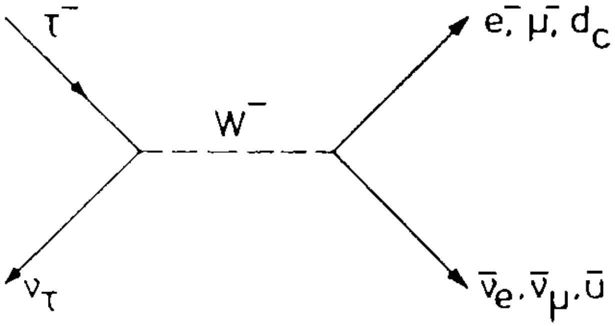

Figure 5.2: A Feynman diagram of τ lepton decays.

Decay Channel	BR (%)
$\tau \to e\bar{\nu}_e\nu_\tau$	17.85 ± 0.29
$\tau \to \mu\bar{\nu}_\mu\nu_\tau$	17.45 ± 0.27
$\tau \to h^-\nu_\tau$	12.47 ± 0.35
$\tau \to h^-\pi^0\nu_\tau$	23.4 ± 0.6
$\tau \to h^-2\pi^0\nu_\tau$	9.0 ± 0.6
$\tau \to h^-n\pi^0\nu_\tau (n \geq 3)$	1.8 ± 0.6
$\tau \to 2h^-h^+\nu_\tau$	8.0 ± 0.3
$\tau \to 2h^-h^+nN\nu_\tau (n \geq 1)$	5.2 ± 0.4

Table 5.1: The world average of τ branching ratio. Here, h is a charged hadron and N is a neutral particle.

$$\begin{aligned} BR(\text{3-prong}) &= 14.06 \pm 0.20\ \% \\ BR(\text{5-prong}) &= 0.11 \pm 0.03\ \%\ . \end{aligned} \tag{5.3}$$

The number of 5-prong decays is negligible and we concentrate on detecting 1-prong and 3-prong τ lepton decays.

5.4 $\tau^+\tau^-$ Event Selection

As we saw above, the final states for $\tau^+\tau^-$ events have low charged multiplicity (typically, less than seven) and the charged tracks tend to have high momentum. To separate these events topologically from hadronic events, which have high charged multiplicities, we select only 1-vs.-1 topology events, in which both of two τ leptons decay into 1-prong's, and 1-vs.-3 topology events, in which one τ decays into a 1-prong while the other τ decays into a 3-prong. Two-photon hadronic events have low charged multiplicities but can also be separated from $\tau^+\tau^-$ events because their tracks have low momenta. However, 1-vs.-1 topology events are difficult to separate from radiative electroweak processes, such as $e^+e^- \to e^+e^-\gamma$ and $e^+e^- \to \mu^+\mu^-\gamma$, where the radiated photons are undetected, or two-photon no-tag lepton pair productions, such as $e^+e^- \to e^+e^-e^+e^-$, $e^+e^- \to e^+e^-\mu^+\mu^-$, and $e^+e^- \to e^+e^-\tau^+\tau^-$. We do not attempt to select 1-vs.-1 topology events in which both τ's decay into same species of lepton in order to reduce these backgrounds. These topological cuts result 91.8% coverage of all $\tau^+\tau^-$ events.

The criteria we applied to select $\tau^+\tau^-$ events are as follows:

(i) $N_{CDC} \leq 10$, $N_{good\ CDC} \geq 2$, $N_{CDC} - N_{good\ CDC} \leq 2$,
where N_{CDC} and $N_{good\ CDC}$ are the numbers of CDC tracks and "good" CDC tracks, respectively. The conditions of good CDC tracks are $|R_0| \leq 2.0\ cm$, $|Z_0| \leq 5.0\ cm$ with the momenta $p \geq 0.5\ GeV$. For the case where there are only 2 tracks in the event, tighter conditions $|R_0| \leq 0.5\ cm$, $|Z_0| \leq 3.0\ cm$, and $p \geq 2.5\ GeV$ are applied.

(ii) $Max{\cdot}p \geq 1.0\ GeV$,
where $Max{\cdot}p$ is the momentum of the most energetic good CDC track.

(iii) $|\sum Q| \leq 2$,
where $\sum Q$ is the sum of charges of good CDC tracks in the event.

(iv) $E_{SHC} \leq 0.8E_{CM}$, $Max \cdot E_{clus} \leq 0.45E_{CM}$, $\sum E_{clus}^{chg} \leq 0.6E_{CM}$,
where E_{SHC} is the total energy deposited in the SHC, $Max \cdot E_{clus}$ is the energy of the most energetic cluster in the SHC, and $\sum E_{clus}^{chg}$ is the energy sum of the clusters matched with the CDC tracks.

(v) $E_{vis}/\sqrt{s} \geq 0.2$,
where E_{vis} is the visible energy defined in 4.2.4. Momenta of the good CDC tracks and energies of the "neutral" SHC clusters, which do not match with the CDC tracks, are used.

(vi) $|\sum P_z|/E_{vis} < 0.4$,
where $\sum P_z$ is the momentum balance defined in 4.2.4. Also, only the good CDC tracks and the neutral SHC clusters are used.

(vii) $N_e(jet) \leq 1$,
where $N_e(jet)$ is the number of jets containing one or more tracks identified as electrons by overlap of the CDC tracks and the SHC clusters.

(viii) $N_\mu(jet) \leq 1$,
where $N_\mu(jet)$ is the number of jets containing one or more tracks identified as muons.

(ix) $N_{jet} = 2$, $N_{stray\ track} = 0$,
where N_{jet} is the number of jets in the events and $N_{stray\ track}$ is the number of "stray" tracks which are good CDC tracks falling outside the 30 degree jet cones.

(x) The event must have 2 tracks or jets with $|\cos\theta| \leq 0.73$.

(xi) $160° \leq \theta_{jet-jet} \leq 179.5°$,
where $\theta_{jet-jet}$ is the opening angle between the two jets.

Backgrounds from hadronic events are rejected by criteria (i) and (ix). Criteria (v), (vi), and (xi) remove two-photon events. Di-muon events as well as cosmic rays are eliminated by criteria (viii) and (xi). Bhabha events, which are the most serious source of backgrounds, are rejected by criteria (iv), (vii), and (xi). After all selection criteria, a visual scan is carried out to remove obvious backgrounds.

Source	Rate (%)
hadronic event	0.4
Bhabha	0.3
di-muon	0.4
$e^+e^-e^+e^-$	0.7
$e^+e^-\mu^+\mu^-$	0.2
$e^+e^-\tau^+\tau^-$	0.9
cosmic ray	0.7
Total	3.6

Table 5.2: The background rate for each source.

Of all selected $\tau^+\tau^-$ event candidates, events satisfy $|\cos\theta| < 0.7071$ are used for the following analysis.

In the data sample for the integrated luminosity of $\int Ldt = 32.60\ pb^{-1}$, 380 events passed all of the selection criteria and the visual scan. The fractions of the background events that remain in the final sample are estimated using Monte Carlo simulations of the various processes and cosmic rays events triggered in the Cosmic Ray Gate. The results are shown in Table 5.2. The sum of all backgrounds is estimated to be 3.6% of the selected $\tau^+\tau^-$ events.

5.5 $\tau^+\tau^-$ Cross Section

The differential cross section for $e^+e^- \rightarrow \tau^+\tau^-$ is calculated in the same way as di-muon process using eq. (5.1). We also use the same $\cos\theta$ bin size (*i.e.*, $\Delta\cos\theta = 0.1178$).

The detection efficiency for $\tau^+\tau^-$ events is the product of ϵ_{sel} and ϵ_{trig} as defined in Section 5.2.

The detection efficiency of the selection criteria is small compared to that for hadronic and di-muon events because of the severe criteria that are applied to suppress backgrounds. ϵ_{sel} is estimated to be about 0.45~0.47 for $|\cos\theta| < 0.7071$ using Monte Carlo simulated events generated by the FS program. Triggers for $\tau^+\tau^-$ events are primarily generated by two independent trigger sources: combinations of ITC and CDC track triggers, and SHC energy triggers. The trigger efficiency (ϵ_{trig}) is estimated using the selected $\tau^+\tau^-$ event sample by

$$\epsilon_{trig} = \frac{S}{A} + \frac{X}{A}\left(1 - \frac{S \cap X}{X}\right), \tag{5.4}$$

where A, S, X, and $S \cap X$ are the numbers of all events, events triggered by the SHC, events triggered by the ITC and CDC, and events triggered by both of the two sets of triggers, respectively. We measure ϵ_{trig} = 99.2% ~ 100% for $|\cos\theta| < 0.7071$ for different center-of-mass energies.

The radiative correction factor, $1+\delta$, is calculated by the FS program. As in the di-muon case, the effects of higher order terms are negligible.

The differential cross sections for $e^+e^- \to \tau^+\tau^-$ for the combined data from all energies are shown in Fig. 5.3.

5.6 Results

The R values (R_{ll}'s) and the forward-backward charge asymmetries (A_{ll}'s) for di-muon and $\tau^+\tau^-$ processes are calculated by fitting the differential cross sections to formula (2.31). The results are listed in Table 5.3 together with the predictions of the standard model. The two errors listed are the statistical error and systematic error. The systematic errors in R_{ll}'s are dominated by the uncertainty in the luminosities, background estimations, and detection efficiencies. The systematic errors in A_{ll}'s are dominated by the uncertainty in θ dependence on the detection efficiencies and background estimations.

Fig. 5.4 and Fig. 5.5 shows plots of $R_{\mu\mu}$, $R_{\tau\tau}$, $A_{\mu\mu}$, and $A_{\tau\tau}$ together with standard model predictions. The error bars represent the statistical and systematic errors added in quadrature.

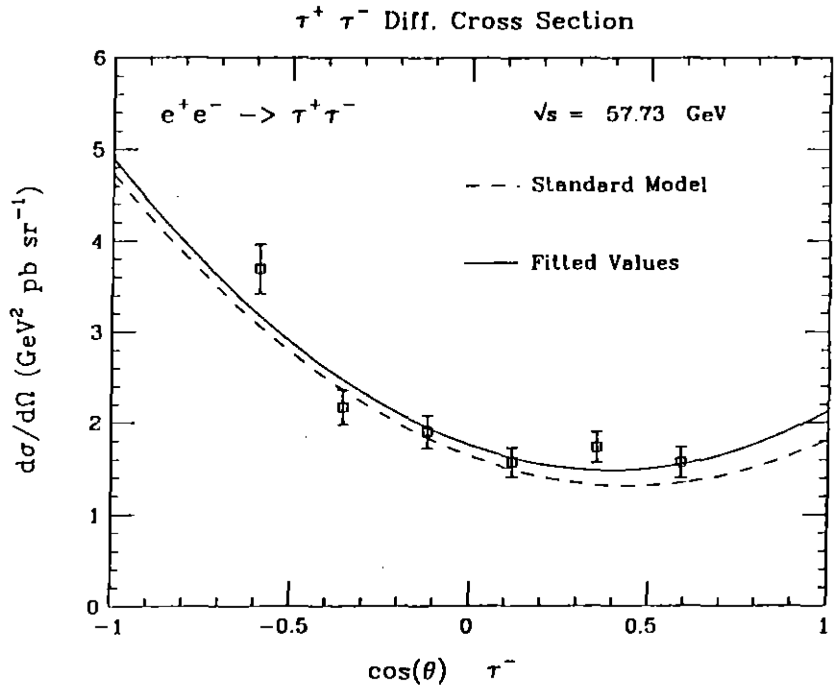

Figure 5.3: The differential cross section for $e^+e^- \to \tau^+\tau^-$ process. Data for all energies are combined.

$\sqrt{s}$ (GeV)	$\int L dt$ (pb^{-1})	$N_{selected}$	$R_{\mu\mu}$	R_{theory}	$A_{\mu\mu}$	A_{theory}
52	3.98	80	1.11±0.13±0.03	1.027	−0.465 ± 0.083 ± 0.004	−0.250
55	3.27	49	0.88±0.13±0.02	1.039	−0.149 ± 0.166 ± 0.001	−0.294
56	5.99	106	1.11±0.11±0.02	1.044	−0.391 ± 0.090 ± 0.003	−0.309
56.5	0.99	26	1.70±0.35±0.04	1.046	+0.035 ± 0.272 ± 0.000	−0.317
57	4.40	74	1.11±0.14±0.02	1.049	−0.403 ± 0.093 ± 0.003	−0.326
58.73	2.66	41	1.05±0.17±0.02	1.061	−0.177 ± 0.165 ± 0.001	−0.356
60	3.55	50	0.99±0.15±0.02	1.071	−0.448 ± 0.103 ± 0.003	−0.380
60.8	3.48	57	1.21±0.17±0.03	1.078	−0.521 ± 0.081 ± 0.004	−0.395
61.4	4.29	53	0.91±0.14±0.02	1.084	−0.217 ± 0.170 ± 0.002	−0.407

$\sqrt{s}$ (GeV)	$\int L dt$ (pb^{-1})	$N_{selected}$	$R_{\tau\tau}$	R_{theory}	$A_{\tau\tau}$	A_{theory}
52	3.98	64	1.36±0.17±0.04	1.027	−0.179 ± 0.130 ± 0.002	−0.250
55	3.27	40	1.15±0.20±0.03	1.039	−0.108 ± 0.184 ± 0.002	−0.294
56	5.99	67	1.11±0.14±0.03	1.044	−0.263 ± 0.127 ± 0.003	−0.309
56.5	0.99	8	0.75±0.25±0.02	1.046	−0.917 ± 0.545 ± 0.011	−0.317
57	4.40	56	1.27±0.18±0.03	1.049	−0.562 ± 0.063 ± 0.007	−0.326
58.73	2.66	28	1.13±0.22±0.03	1.061	−0.113 ± 0.209 ± 0.002	−0.356
60	3.55	37	1.14±0.20±0.03	1.071	−0.517 ± 0.130 ± 0.006	−0.380
60.8	3.48	41	1.35±0.22±0.03	1.078	+0.029 ± 0.190 ± 0.001	−0.395
61.4	4.29	39	1.06±0.18±0.03	1.084	−0.411 ± 0.140 ± 0.005	−0.407

Table 5.3: A summary of $R_{\mu\mu}$, $A_{\mu\mu}$, $R_{\tau\tau}$, and $A_{\tau\tau}$. Errors listed are the statistical (first) and the systematic (second).

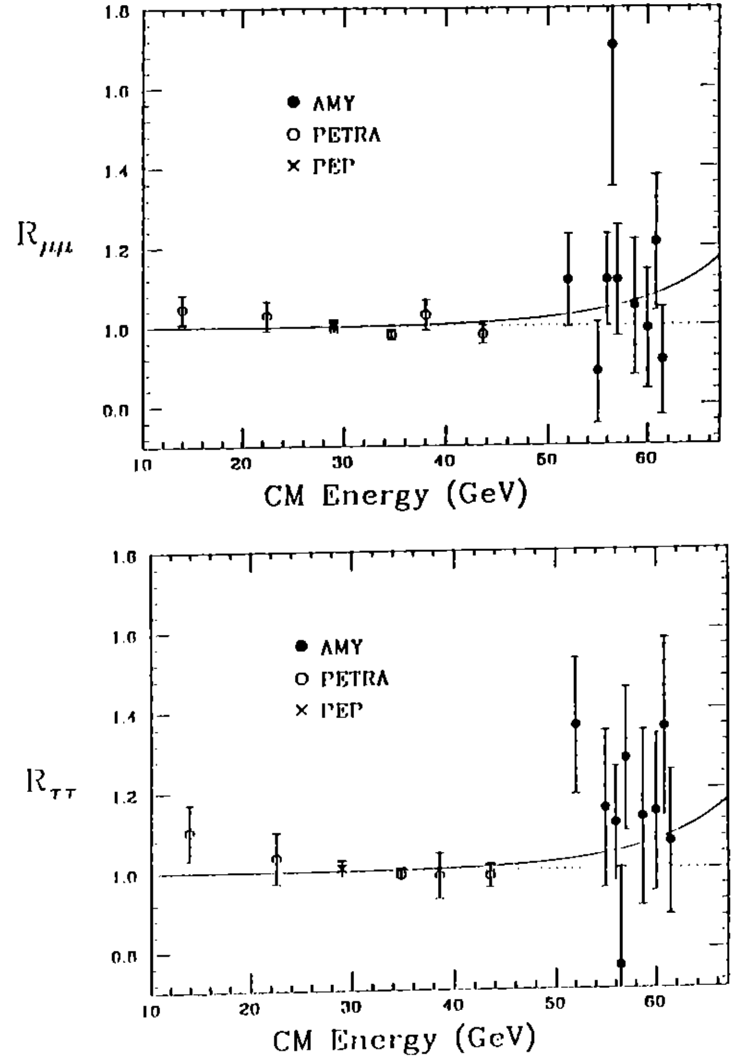

Figure 5.4: The results of $R_{\mu\mu}$ and $R_{\tau\tau}$. The error bars include the statistical and the systematic errors added in quadrature. The lower energy data from other experiments are combined for display purposes. The solid curves are the standard model predictions for $M_Z = 91.173$ GeV and $\sin^2\theta_W = 0.2259$.

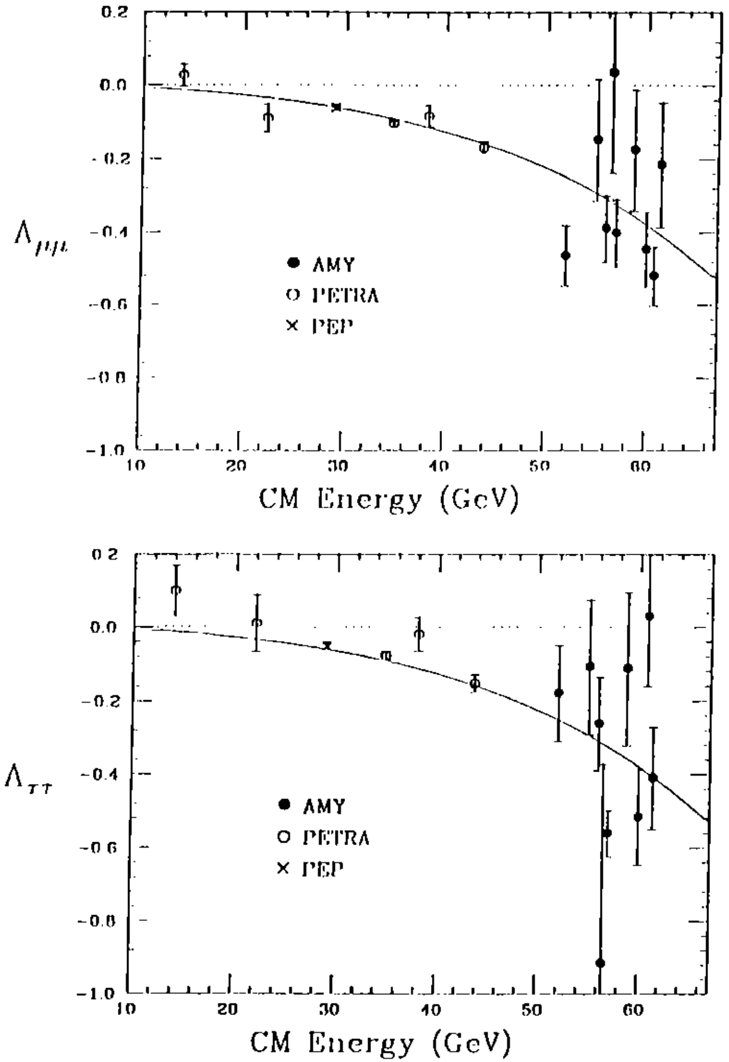

Figure 5.5: The results of $A_{\mu\mu}$ and $A_{\tau\tau}$. The error bars include the statistical and the systematic errors added in quadrature. The lower energy data from other experiments are combined for display purposes. The solid curves are the standard model predictions for $M_Z = 91.173$ GeV and $\sin^2\theta_W = 0.2259$.

Chapter 6

Mass of the Extra Z Bosons

The measurements of R_{hadron}, $R_{\mu\mu}$, $A_{\mu\mu}$, $R_{\tau\tau}$, and $A_{\tau\tau}$ are described in the previous chapters. In this chapter, we fit these data together with results from other experiments of TRISTAN, PEP, and PETRA to the theoretical formulae discussed in Chapter 2 to look for evidence of extra Z bosons.

6.1 The Fitting Procedure

The data sample used for fitting consists of 103 measurements of R_{hadron} [48], 67 measurements of $R_{\mu\mu}$, 51 measurements of $A_{\mu\mu}$ [49], 54 measurements of $R_{\tau\tau}$, and 42 measurements of $A_{\tau\tau}$ [50], spanning the energy range, 12GeV $\leq \sqrt{s} \leq$ 64GeV. The sample includes unpublished results from AMY. We only use R_{hadron} measurements for $\sqrt{s} \geq 20$ GeV to avoid the effects of possible $b\bar{b}$ resonances. As discussed in Chapter 4, we adjusted the R_{hadron} values from TOPAZ and VENUS for the effects of higher-order radiative corrections; we did not make any adjustments to the PEP and PETRA measurements.

For R_{hadron}, we incorporate the systematic errors from different experiments by means of the χ^2 vector defined by CELLO group (the last of Ref. [48]). The error on R_{hadron} measurement is divided into three categories: the statistical error σ_{stat}, the point-to-point systematic error σ_{ptp}, and an overall normalization error σ_{norm} which is common to all of the measurements of each particular experiment. We define an $n \times n$ error matrix V_{ij} for n data points: the diagonal element V_{ii} is the sum of the squares of σ_{stat}, σ_{ptp}, and σ_{norm} for the data point i; the correlation in the errors between data points i and j are included in the off-diagonal element V_{ij}. If the data points i and j are from different experiments, V_{ij} is set to be zero; this is equivalent to assuming that there are no correlation in the normalization errors of the different experiments. If the data points i and j are from the same experiment, their normalization errors are correlated and V_{ij} is set to be the square of the common normalization error σ^2_{norm}. Some experiments give different normalization errors for different run periods; we split these errors into a normalization error common for all run periods (σ_{norm1}) and an additional error common for to specific run periods (σ_{norm2}). We use the common part for the data points i and j for V_{ij}. The χ^2 expression to be minimized is

$$\chi^2 = \Delta^T V^{-1} \Delta, \tag{6.1}$$

where Δ is the $n-$vector representing the n residuals $R_i - R_{fit}$.

For the di-lepton results, where most groups did not separately specify their overall systematic errors, we use a simple scalar χ^2 analysis, adding all systematic errors to the statistical error in quadrature.

The data from all experiments are shown in Appendix A with the errors presented in the format described above.

For the standard model parameters, we use $M_Z = 91.173 \pm 0.020$ GeV [47], $\sin^2\theta_W = 0.2259 \pm 0.0029$ [47], $\Lambda^{(5)}_{\overline{MS}} = 0.175^{+0.041}_{-0.034}$ GeV [47], and $M_W = 80.13 \pm 0.31$ GeV [51]. To check how extra Z bosons improve the fit, we determine the χ^2 for the standard model alone to be $\chi^2_{SM} = 283.4$ for 317 degrees of freedom ($N_{DF} = 317$) and see if fits to the data including possible Z' 's improve on this significantly. The confidence level (CL) of a fit with large N_{DF} is approximately given by

$$\mathrm{CL} \simeq \frac{1}{\sqrt{2\pi}} \int_y^\infty e^{-x^2/2} dx\ , \tag{6.2}$$

where $y = \sqrt{2\chi^2} - \sqrt{2N_{DF} - 1}$ [62]. The $\chi^2/N_{DF} = 283.4/317$ for the standard model case corresponds to CL=90.8%, which is already a good fit.

We treat $M_{Z'}$ as the only free parameter for the E_6 and $SU(5)_c$ models, and $\sin\phi$ as the other free parameter for the $SU(2)_q \times SU(2)_l$ model. We take the central values of the standard model parameters. The Z_0 and Z'_0 boson mixing angle, θ' is calculated from M_Z and $M_{Z'}$ in the $SU(5)_c$ model and is fixed to be $\theta' = 0$ in the E_6 and $SU(2)_q \times SU(2)_l$ models, i.e., we assume no mixing. For the

E_6 model, we try an alternative approach. We allow the electroweak parameters (M_Z, $\sin^2\theta_W$, and M_W) to vary within their quoted errors subject to the constraint $M_W/\cos\theta_W \geq M_Z$ and use eq. (2.47) to determine θ'.

6.2 Constraints from Other Experiments

Experimental constraints on Z' masses have been derived from a variety of measurements, such as precise measurements of the Z^0 parameters [52, 58], low energy neutral-current measurements [53, 54], searches for evidence of Z' production in hadron collider experiments [55, 59], and fits to e^+e^- measurements of R_{had}, R_{ll}, and A_{ll} (including TRISTAN's [56]). The analysis in this chapter is based on the last method.

The constraints on E_6 Z''s (Z_ψ, Z_χ, and Z_η) from cross section limits for $p\bar{p} \to Z' \to e^+e^-(\mu^+\mu^-)$ at the CDF experiment, taken from Ref. [55], are shown in Fig. 6.1. Reference [54] gives a 90% CL mass limit for the Z_ν boson of 180 GeV, based on low energy neutral-current neutrino scattering experiments. An analysis of energy emission from the supernova SN 1987A [57] gives a much higher mass limit than other techniques ($M_{Z'} > 1 \sim 2$ TeV).

Reference [58] gives a mass limit of the $SU(5)_c$ model as $M_{Z'} > 102$ GeV based on a comparison of LEP and TRISTAN data to the model. Since the Z' in this model couples very weakly to leptons, we cannot see its direct production in e^+e^- or $\mu^+\mu^-$ final states at hadron colliders. An analysis by R. Foot *et al.* in Ref. [59] gives a mass limit from a study of two jet production at UA2 [60] of $M_{Z'} > 280$ GeV for the $SU(5)_c$ model. Note that this analysis was not performed by the UA2 collaboration and the details of the analysis were not published.

For the $SU(2)_q \times SU(2)_l$ model, Ref. [61] presents a calculation of the cross section for $p\bar{p} \to Z' \to e^+e^-$ at Tevatron energies as shown in Fig. 6.2. By comparing it to the CDF group's cross section limit, shown in Fig. 6.1 [55], we can deduce mass limits for this model: the excluded region in $\sin\phi$ -$M_{Z'}$ plain is shown in Fig. 6.3.

The mass limits of Z''s from other experiments are summarized in Table 6.1.

6.3 Results and Discussions

The results from our analysis are shown in Tables 6.2 and 6.3. The errors on the $M_{Z'}$ values in Table 6.2 correspond to the 68% CL fitting error, *i.e.*, $\Delta\chi^2 = 1.0$. The error of the $SU(2)_q \times SU(2)_l$ model is shown as a 68% CL contour ($\Delta\chi^2 = 2.3$) in the $\sin\phi$-$M_{Z'}$ plain in Fig. 6.4. The $\Lambda^{(5)}_{\overline{MS}}$ error has a negligible effect on the results. As an example, the results of the best-fit to the E_6 η model for $\theta' = 0$ are shown in Figures 6.5~6.7. The tables show that the best-fit Z' mass values from our experiment have already been excluded by other experiments for all models tested except the E_6 ν model. The mass limit of the Z_ν boson is lower compared with other models because it is not based on newer results from LEP and CDF.

For the case of the E_6 models, there is another parameter λ^2 that we have fixed at $\frac{5}{3}\sin^2\theta_W$ (**2.3.2**). The results from other experiments cannot exclude rather light Z''s ($M_{Z'} < 150$ GeV) for the case where λ^2 is very small. However, we would not see any effects at TRISTAN, either.

We conclude that although extra Z bosons would improve the agreement between e^+e^- data and theory, the best fit values for the masses have been ruled out by $p\bar{p}$ production data from other experiments.

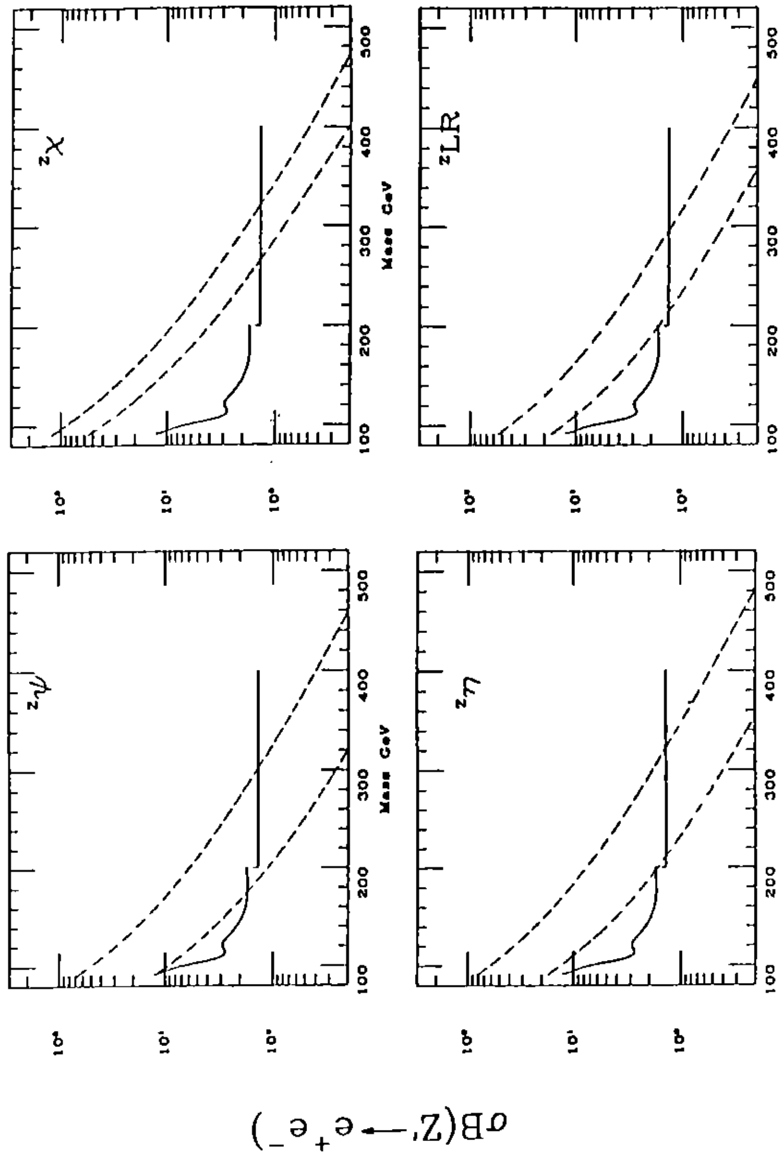

Figure 6.1: Mass Limits for four E_6 models, Z_ψ, Z_χ, Z_η, and Z_{LR} (not discussed in this thesis) from the direct production at CDF (95% CL), taken from Ref. [55]. In each plot, the solid curve is the upper limit of $\sigma \cdot B$. The upper dashed curves are predicted $\sigma \cdot B$ for the case where the Z' decays into only known fermions and the lower dashed curves are for the case where the Z' decays into all fermions and s-fermions in the E_6 model.

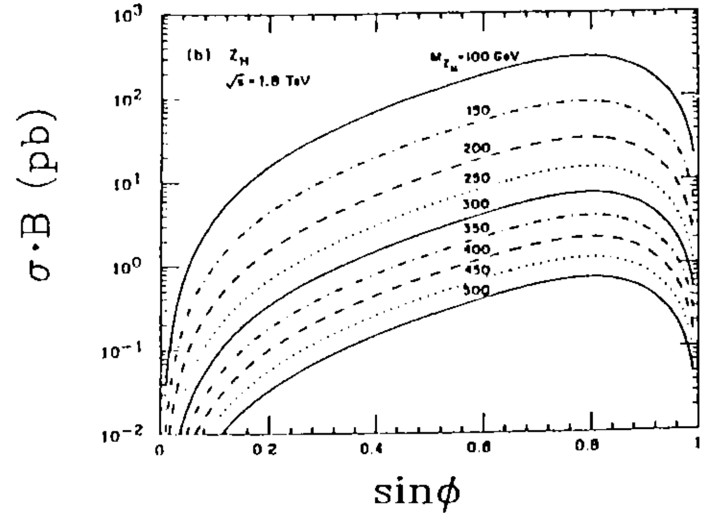

Figure 6.2: Cross sections for $p\bar{p} \to Z' \to e^+e^-$ at $\sqrt{s} = 1.8$ TeV in $SU(2)_q \times SU(2)_l$ model, taken from Ref. [61].

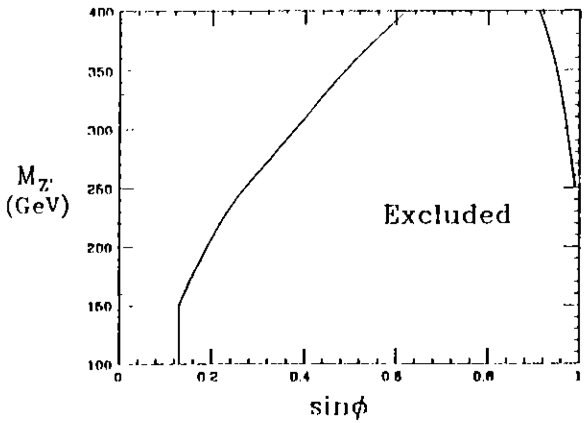

Figure 6.3: The region of $\sin\phi$ - $M_{Z'}$ in the $SU(2)_q \times SU(2)_l$ model excluded (95% CL). This limit is obtained from the comparison between Fig. 6.1 and Fig. 6.2.

model of Z'		$M_{Z'}$ (GeV)	confidence level (%)
E_6	ψ	175 [a], 300 [b]	95
	χ	265 [a], 320 [b]	95
	η	210 [a], 320 [b]	95
	ν	180 [c]	90
$SU(5)_c$		280 [d]	90
$SU(2)_q \times SU(2)_l$		See Fig. 6.3 [e]	95

a. Ref. [55] (CDF) exotic decay channels are open
b. Ref. [55] (CDF) exotic decay channels are closed
c. Ref. [54] (low energy NC data)
d. Ref. [59] Analysis of UA2 data [60] by Foot *et al.*
e. Our analysis of CDF data [55] with the calculation in Ref. [61]

Table 6.1: Mass limits of extra Z bosons from other experiments.

Model of Z'		Results of the Fits		
		$M_{Z'}$ (GeV)	χ^2/N_{DF} †	CL (%)
E_6	ψ	$267^{+\infty}_{-96}$	283.0 / 316	90.8
	χ	250^{+98}_{-42}	279.3 / 316	93.1
	η	162^{+62}_{-26}	279.5 / 316	93.0
	ν	$269^{+\infty}_{-82}$	282.7 / 316	91.0
$SU(5)_e$		92^{+296}_{-7}	282.4 / 316	91.2
$SU(2)_q \times SU(2)_l$		277 ($\sin\phi = 0.610$)	277.4 / 315	93.7

† $\chi^2/N_{DF} = 283.4/317$ for the standard model (90.8% CL)

Table 6.2: Results of the fits. θ' is set to be 0 for the E_6 and $SU(2)_q \times SU(2)_l$ models. The quoted errors correspond to $\Delta\chi^2 = 1.0$.

Model of Z'		Results of the Fits			
		$M_{Z'}$ (GeV)	θ'	χ^2/N_{DF}	CL (%)
E_6	ψ	176	0.026	282.6 / 316	91.1
	χ	249	0.012	278.9 / 316	93.3
	η	157	0.014	279.2 / 316	93.2
	ν	240	0.000	282.3 / 316	91.3

Table 6.3: Results of the fits. θ' is allowed to vary under the constraints of the standard model parameters.

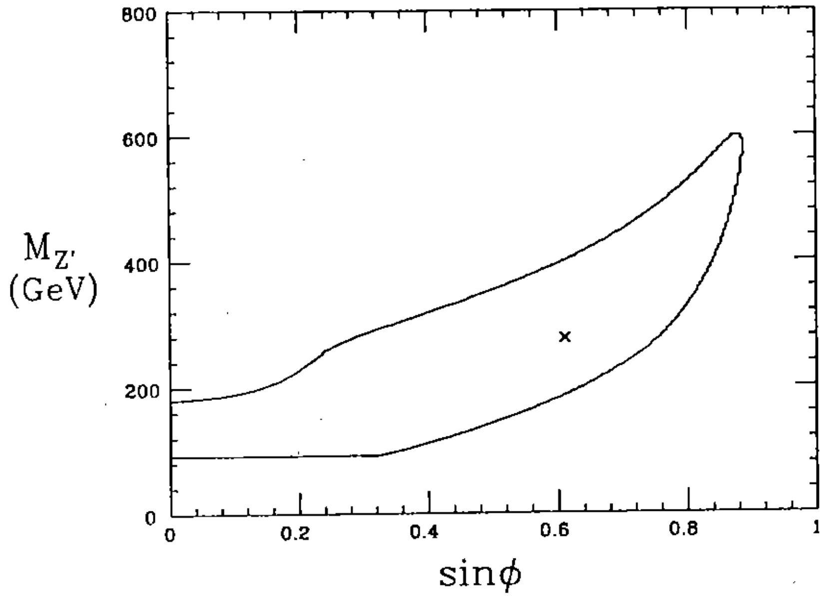

Figure 6.4: 68% CL contour in the $\sin\phi$ -$M_{Z'}$ plain for the $SU(2)_q \times SU(2)_l$ model ($\Delta\chi^2 = 2.3$).

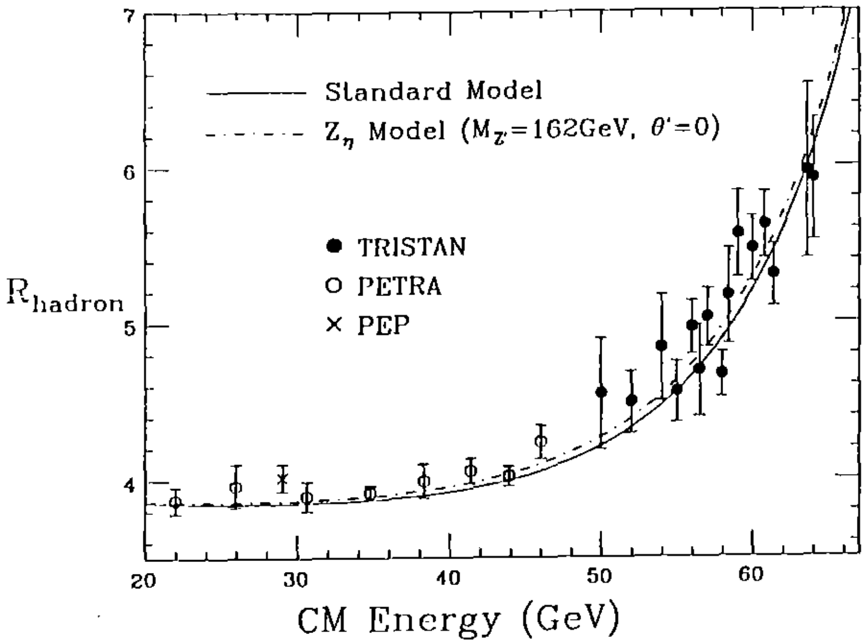

Figure 6.5: R_{hadron} with the theoretical predictions of the standard model (solid line) and the E_6 model with Z_η boson (dot-dashed line) for $M_{Z'} = 162$ GeV, $\theta' = 0$.

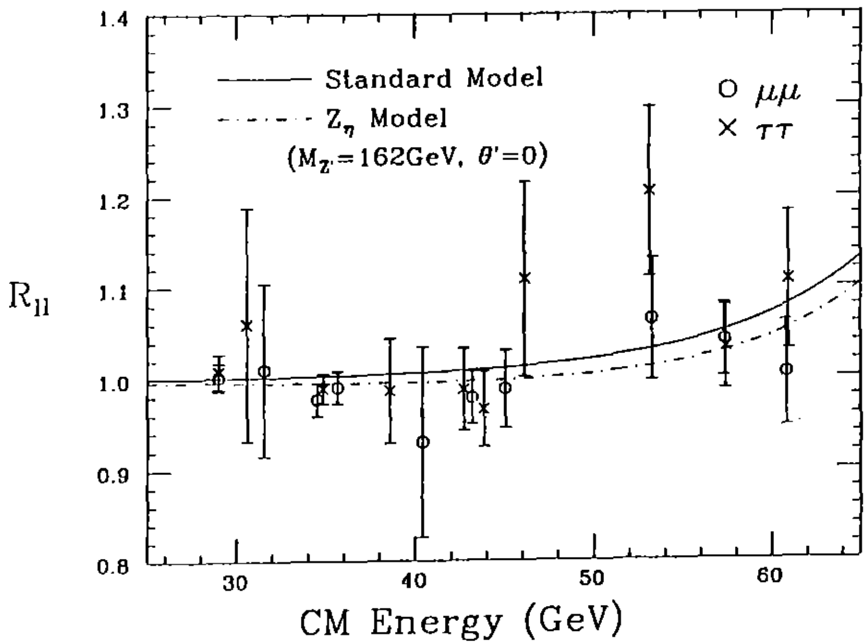

Figure 6.6: $R_{\mu\mu}$ and $R_{\tau\tau}$ with the theoretical predictions of the standard model (solid line) and the E_6 model with Z_η boson (dot-dashed line) for $M_{Z'} = 162$ GeV, $\theta' = 0$.

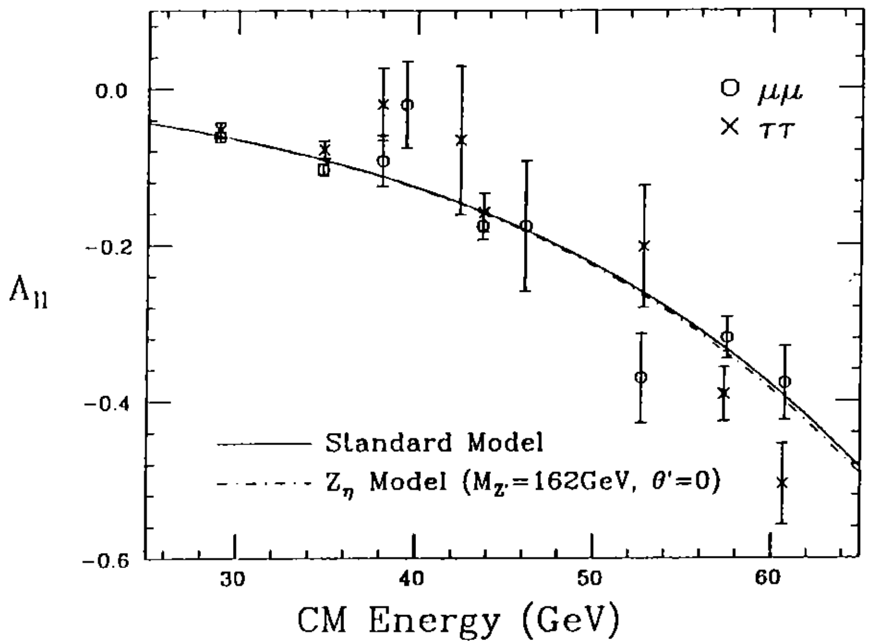

Figure 6.7: $A_{\mu\mu}$ and $A_{\tau\tau}$ with the theoretical predictions of the standard model (solid line) and the E_6 model with Z_η boson (dot-dashed line) for $M_{Z'} = 162$ GeV, $\theta' = 0$.

Chapter 7

Determination of the QCD Coupling Strength

In this chapter we compare our results for the total hadronic cross section to the standard model prediction given in eq. (2.37). This relation is a function of M_Z, $\sin^2\theta_W$, and α_s; since M_Z and $\sin^2\theta_W$ are determined precisely by other experiments, we concentrate on extracting the QCD coupling constant α_s from fitting the formula to the R value measurements.

The advantage of using R value measurements for determining α_s is that there is no dependence on non-perturbative processes (e.g. fragmentation models, jet algorithms, etc.) and the QCD correction is calculated up to $O(\alpha_s^3)$, while only $O(\alpha_s^2)$ calculations are available for most other processes. However, since in the TRISTAN energy range the QCD contributions are only about 4% of the total R value, the sensitivity to α_s is limited; precision measurements of R are required for a reasonable determination of α_s.

7.1 Parameterization of α_s

To fit R values in the energy range of 20 GeV $\leq \sqrt{s} \leq$ 64 GeV, we have to assume an s dependence for the "running" coupling constant α_s.

In QCD, α_s obeys the β-function

$$\mu^2 \frac{\partial a}{\partial \mu^2} = -\beta_0 a^2 - \beta_1 a^3 - \beta_2 a^4 \cdots \qquad (7.1)$$

$$= -\beta_0 a^2(1 + c_1 a + c_2 a^2 \cdots),$$

for a four-momentum transfer value μ. In the modified minimal subtraction ($\overline{MS}$) scheme [5], $a = \alpha_s(\mu)/\pi$, $\beta_0 = \frac{1}{4}(11 - \frac{2}{3}n_f)$, $\beta_1 = \frac{1}{16}(102 - \frac{38}{3}n_f)$, and $\beta_2 = \frac{1}{64}(\frac{2857}{2} - \frac{5033}{18}n_f + \frac{325}{54}n_f^2)$, where n_f is the number of quark flavors. Integrating eq. (7.1) over μ from the cut-off μ_0 to Q, we obtain the relation

$$\begin{aligned} \frac{1}{\alpha_s(Q)} &= \frac{1}{\alpha_s(\mu_0)} + \frac{2}{\pi}\beta_0 \ln\left(\frac{Q}{\mu_0}\right) - \frac{\beta_1}{\pi\beta_0}\ln\left[\frac{\alpha_s(Q)}{\alpha_s(\mu_0)}\right] \\ &- \frac{1}{\pi^2\beta_0^2}(\beta_2\beta_0 - \beta_1^2)[\alpha_s(Q) - \alpha_s(\mu_0)] + O(\alpha_s^2). \end{aligned} \tag{7.2}$$

From eq. (7.2), one can determine $\alpha_s(Q)$ for arbitrary momentum transfer (or mass scale) Q, given $\alpha_s(\mu_0)$ at the reference mass scale μ_0. Here, n_f is chosen to be the number of quark flavors with mass $m_q \leq Q$. It is convenient to introduce a dimensional parameter $\Lambda_{\overline{MS}}$ instead of $\alpha_s(\mu_0)$, where $\alpha_s(Q)$ and $\Lambda_{\overline{MS}}$ are related as

$$\begin{aligned} \ln\frac{Q^2}{\Lambda_{\overline{MS}}^2} &= \frac{1}{\beta_0 a} - \frac{c_1}{\beta_0}\ln\frac{c_1}{\beta_0} + \frac{c_1}{\beta_0}\ln\frac{c_1 a}{1 + c_1 a} + \frac{c_1}{2\beta_0}\ln\frac{(1 + c_1 a)^2}{1 + c_1 a + c_2 a^2} \\ &+ \frac{2c_2 - c_1^2}{\sqrt{\Delta}\beta_0}\left[\tan^{-1}\frac{c_1 + 2c_2 a}{\sqrt{\Delta}} - \tan^{-1}\frac{c_1}{\sqrt{\Delta}}\right] \end{aligned} \tag{7.3}$$

where $\Delta = 4c_2 - c_1^2$ [4]. For a given value of $\Lambda_{\overline{MS}}$, one can determine $\alpha_s(Q)$ by solving the above equation iteratively.

In the conventional definition of the $\overline{MS}$ scheme, $\Lambda_{\overline{MS}}$ changes for different n_f to insure the continuity of $\alpha_s(Q)$. In the TRISTAN energy range, $n_f = 5$. We choose the energy independent parameter $\Lambda_{\overline{MS}}$ for $n_f = 5$ ($\equiv \Lambda_{\overline{MS}}^{(5)}$) as the free parameter for fitting rather than α_s itself. The mass scale Q in eq. (2.40) is taken to be the center-of-mass energy $\sqrt{s}$.

7.2 Results and Discussions

The fitting is done using the procedure described in Chapt. 6. We fit R_{hadron} measurements for 20 GeV $< \sqrt{s} \leq$ 64 GeV to eq. (2.37), with $\Lambda_{\overline{MS}}^{(5)}$ as a free parameter and the other parameters set to the values given in Section 6.1. The results of the fit are:

$$\Lambda_{\overline{MS}}^{(5)} = 0.533^{+.521}_{-.334}\ \text{GeV} \qquad \chi^2/N_{DF} = 88.9/102, \tag{7.4}$$

where the error quoted is the fitting error at $\Delta\chi^2 = 1.0$, corresponding to a 68% confidence level (CL) error. The CL of the best fit value of χ^2/N_{DF} is 82.0%, which is a slight improvement over the χ^2 obtained using the world average value of $\Lambda_{\overline{MS}}^{(5)} = 0.175$ GeV [47]. The latter yields $\chi^2/N_{DF} = 90.1/103$ corresponding to 81.4% CL, which is also an acceptable fit.

There are additional systematic errors due to uncertainties of the standard model parameters M_Z and $\sin^2\theta_W$. Fixing $M_Z = 91.173$ GeV and allowing $\sin^2\theta_W$ to vary over the range $\sin^2\theta_W = 0.2259 \pm 0.0029$ gives:

$$\Lambda_{\overline{MS}}^{(5)} = \begin{array}{lll} 0.553\ \text{GeV} & (\chi^2/N_{DF} = 89.4/102) & \text{for } \sin^2\theta_W = 0.2230, \\ 0.533\ \text{GeV} & (\chi^2/N_{DF} = 88.9/102) & \text{for } \sin^2\theta_W = 0.2259, \\ 0.504\ \text{GeV} & (\chi^2/N_{DF} = 88.4/102) & \text{for } \sin^2\theta_W = 0.2288; \end{array} \tag{7.5}$$

fixing $\sin^2\theta_W = 0.2259$ and allowing M_Z to vary over the range $M_Z = 91.173 \pm 0.020$ GeV yields values of $\Lambda_{\overline{MS}}^{(5)}$ and χ^2 which are unchanged.

The truncation of the series in the β-function (7.1) results ambiguity in the choice of the mass scale Q. Additionally, expressions to $O(\alpha_s^3)$ are renormalization scheme (RS) dependent, because β_2 in eq. (7.1) depends on the chosen RS. To gauge the level of theoretical uncertainty due to the choice of the mass scale and RS, we repeat the same fit for $O(\alpha_s^2)$. The scale-scheme dependences reflect the uncertainties from uncalculated higher order terms and the difference between the $O(\alpha_s^3)$ calculation and the $O(\alpha_s^2)$ calculation gives some measure of size of the higher order contributions, which must be small if the perturbation theory behaves well. Setting $C_3^{V(A)} = 0$ in eq. (2.40) and using eq. (2.36) instead of eq. (7.3), we obtained

$$\Lambda_{\overline{MS}}^{(5)} = 0.446^{+0.413}_{-0.271}\ \text{GeV} \quad (\chi^2/N_{DF} = 88.9/102) \quad \text{for } O(\alpha_s^2). \tag{7.6}$$

Therefore, the size of the theoretical uncertainty is estimated to be about 0.09 GeV, which is much smaller than the experimental error.

The results are summarized as

$$\Lambda_{\overline{MS}}^{(5)} = 0.533^{+0.521}_{-0.334}(\text{fitting})^{+0.020}_{-0.029}(\text{systematic}) \pm 0.090(\text{theory})\ \text{GeV}. \tag{7.7}$$

This value is higher than the world average $\Lambda_{\overline{MS}}^{(5)} = 0.175^{+0.041}_{-0.034}$ GeV [47] but consistent within the error. Fig. 7.1 shows the experimental R values together with the theoretical predictions for $\Lambda^{(5)}_{\overline{MS}} = 0.175$ GeV (the world average value) and $\Lambda^{(5)}_{\overline{MS}} = 0.533$ GeV (our best fit value).

Recently, the LEP experimental groups started using another convention for expressing the running of α_s and express all extraction of $\Lambda_{\overline{MS}}$ in terms of α_s at the mass of the Z^0, $\alpha_s(M_Z)$. Our result can be interpreted as

$$\begin{aligned} \alpha_s(M_Z) &= 0.138^{+0.019}_{-0.020}(\text{fitting}) \pm 0.001(\text{systematic}) \pm 0.004(\text{theory}) \quad (7.8) \\ &= 0.138\ ^{+0.019}_{-0.021}\ , \end{aligned}$$

where all errors are added in quadrature. The world average $\Lambda^{(5)}_{\overline{MS}} = 0.175^{+0.041}_{-0.034}$ GeV corresponds to $\alpha_s(M_Z) = 0.1134 \pm 0.0035$ [47]. Our results are compared in Fig. 7.2 with results obtained by various techniques taken from Ref. [63]. We can see that both the result of this analysis and the results from measurements of Γ_{hadron}, the hadronic decay width on Z^0 pole, differ from values determined by other techniques. Although the error for this analysis is larger than that for other techniques, it and measurements of Γ_{hadron} and the τ leptonic branching ratio are independent of non-perturbative QCD processes and are also based on the $O(\alpha_s^3)$ calculations. Γ_{hadron} is proportional to the total hadronic cross section at the Z^0 pole and thus, one can extract α_s using the same formula for the QCD corrections as for the case of R value. This technique has the same disadvantage as the fit of R values, *i.e.*, the lack of much sensitivity, due to the small QCD contributions in Γ_{hadron}. It should be noted that the total hadronic cross section is consistently higher than the standard model predictions for the world average value of $\Lambda^{(5)}_{\overline{MS}}$ in the energy range of 20 GeV $< \sqrt{s} < M_Z$ (e.g. see Ref. [64]).

The α_s values from the measurements of the τ branching ratio, based on the fact that only the numerator has QCD contributions in the ratio

$$R_\tau \equiv \frac{\Gamma(\tau^- \to \nu_\tau + hadrons)}{\Gamma(\tau^- \to \nu_\tau e^- \bar{\nu}_e)}\ ,$$

are consistent with other techniques. This method may have an advantage in that α_s is measured at the energy scale of τ lepton mass and the experimental errors become smaller when the results are interpreted in terms of $\Lambda^{(5)}_{\overline{MS}}$ or $\alpha_s(M_Z)$. However, we note that the τ analysis may be prone to biases from meson resonances, because of the low center-of-mass energies that are accessed in τ decays [65].

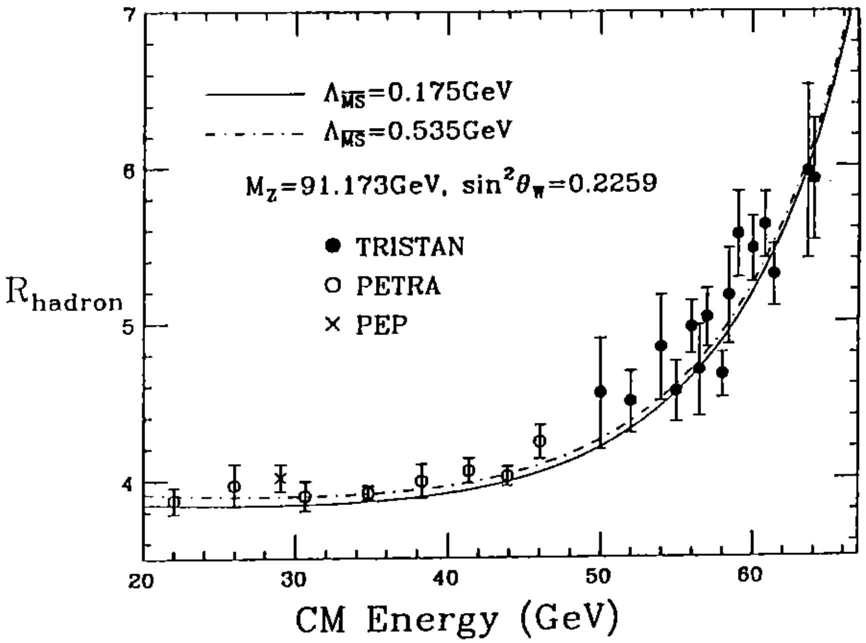

Figure 7.1: Experimental R values together with the standard model predictions for $M_Z = 91.173$ GeV, $\sin^2\theta_W = 0.2259$, and $\Lambda^{(5)}_{\overline{MS}} = 0.175$ GeV (solid curve) or $\Lambda^{(5)}_{\overline{MS}} = 0.533$ GeV (dot-dashed curve).

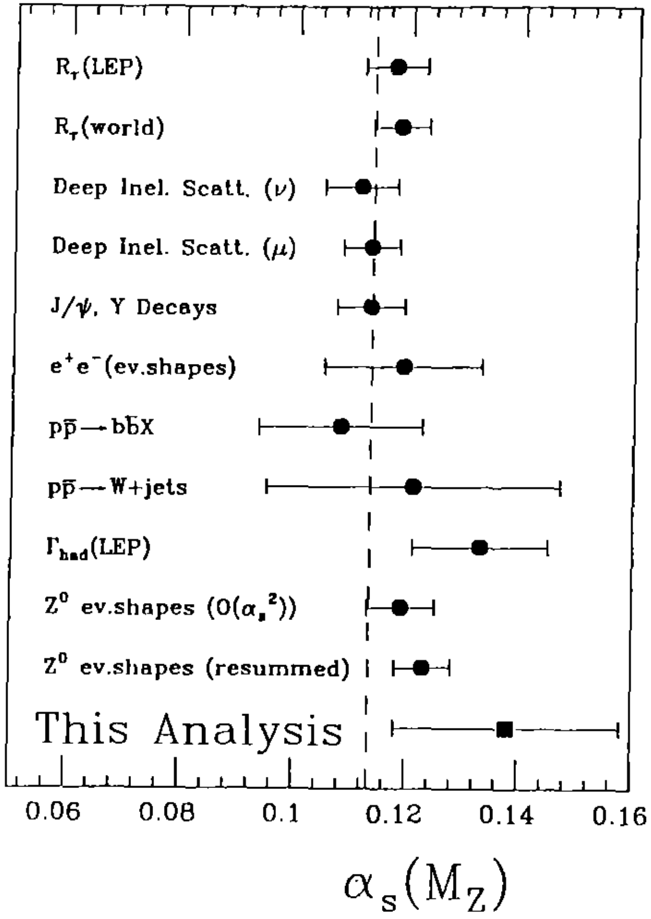

Figure 7.2: Summary of measurements of $\alpha_s(M_Z)$. The dashed line indicates the world average value $\alpha_s(M_Z) = 0.1134$.

Chapter 8

Summary

In this thesis, we have reported on the total cross section for $e^+e^- \rightarrow hadrons$ at 50 GeV $\leq \sqrt{s} \leq$ 64 GeV, and on the total cross sections and forward-backward asymmetries for $e^+e^- \rightarrow \mu^+\mu^-$ and $e^+e^- \rightarrow \tau^+\tau^-$ processes at 52 GeV $\leq \sqrt{s} \leq$ 61.4 GeV, observed in the AMY detector at the TRISTAN e^+e^- collider. All data are consistent with the standard model predictions within errors.

To determine the total cross section for hadronic events, we introduced a new scheme of the radiative corrections using the program ZSHAPE. The ZSHAPE program gives radiative correction factor $(1+\delta)$ which is higher by a few % from that obtained using the FS program, which has been used in our previous analyses. The higher factor is due to the cross term of the QED correction and the electroweak correction, and also due to the higher order diagrams and the "exponentiated" treatment of soft photon processes. Although the difference between the ZSHAPE and the FS becomes smaller in terms of $\epsilon(1+\delta)$, we cannot neglect it for precise measurements.

We looked for the signetures for extra Z bosons by fitting our data, R_{hadron}, $R_{\mu\mu}$, $R_{\tau\tau}$, $A_{\mu\mu}$, and $A_{\tau\tau}$, together with the data from other PEP, PETRA, and TRISTAN experiments, to the theoretical formulae. We tested three different models of Z''s, namely the E_6, $SU(5)_c$, and $SU(2)_q \times SU(2)_l$ models. The confidence levels of the fits are slightly improved over the fit to the standard model. However, the improvement is small and the best fit values of masses of the Z''s are excluded by other experiments.

Within the framework of the standard model, we determined the QCD scale parameter, $\Lambda^{(5)}_{\overline{MS}}$, by fitting the R_{hadron} data to the formula with the $O(\alpha_s^3)$ corrections. We obtained the result of $\Lambda^{(5)}_{\overline{MS}} = 0.533^{+0.521+0.020}_{-0.334-0.029} \pm 0.090$ GeV, which is higher than the world average value $\Lambda^{(5)}_{\overline{MS}} = 0.175^{+0.041}_{-0.034}$ GeV, though consistent within errors. For precise measurement of $\Lambda^{(5)}_{\overline{MS}}$, more studies on the electroweak radiative corrections and a reduction of systematic errors are needed.

Bibliography

[1] S.L. Glashow, Nucl. Phys. **22**, 579 (1961);
S. Weinberg, Phys. Rev. Lett. **19**, 1264 (1967);
A. Salam, *Elementary Particle Theory, Proc. 8th Nobel Symp.*, N. Svartholm, ed., Wiley-Interscience (1968).

[2] M. Gell-Mann, Phys. Rev. **92**, 833 (1953);
K. Nishijima and T. Nakano, Prog. Theor. Phys. **10**, 581 (1953).

[3] L.R. Surguladze and M.A. Samuel, Phys. Rev. Lett. **66**, 560 (1991);
S.G. Gorishny, A.L. Kataev, and S.A. Larin, Phys. Lett. **259B**, 144 (1991).

[4] S.G. Gorishny, A.L. Kataev, and S.A. Larin, Phys. Lett. **212B**, 238 (1988).

[5] W. Celmaster and R.J. Gonsalves, Phys. Rev. Lett. **44**, 560 (1979);
V.G. Chetyrkin, A.L. Kataev, and F.V. Tkachev, Phys. Lett. **85B**, 277 (1979);
M. Dine and J. Sapirstein, Phys. Rev. Lett. **43**, 668 (1979).

[6] R. Bundy, Phys. Lett. **45B**, 340 (1973).

[7] T. Appenlquist and H.D. Politzer, Phys. Rev. **D12**, 1404 (1976);
A. DeRujula and H. Georgi, Phys. Rev. **D13**, 1296 (1976);
J. Jersak, E. Laermann, and P.M. Zerwas, Phys. Lett. **98B**, 363 (1981); Phys. Rev. **D25**, 1218 (1982);
S. Gusken, J.H. Kuhn, and P.M. Zerwas, Phys. Lett. **155B**, 185 (1985).

[8] M.B. Green, J.H. Schwarz, and E. Witten, *Superstring Theory*, Cambridge Univ. Press, Cambridge (1987).

[9] E. Calabi, in: *Algebraic Geometry and Topology*, Princeton Univ. Press, Princeton (1957) p78;
S.T. Yau, Proc. Natl. Acad. Sci. USA **74** (1977) 1798.

[10] R. Slansky, Phys. Rep. **79** (1981) 1.

[11] For detailed review: F. Zwirner, Int. J. Mod. Phys. **A3**, 49 (1988);
J.L. Hewett and T.G. Rizzo, Phys. Reports **183**, 193 (1989).

[12] R. Foot and O.F. Hernandez, Phys. Rev. D **41**, 2283 (1990);
R. Foot, O.F. Hernandez, and T.G. Rizzo, Phys. Lett. **246B**, 183 (1990).

[13] H. Georgi, E.E. Jenkins, and E.H. Simmons, Phys. Rev. Lett. **62**, 2789 (1989).

[14] TRISTAN project group, KEK Report 86-14 (1987).

[15] C. Back *et al.*(AMY collaboration), TRISTAN-EXP-003 (1984).

[16] S.K. Sahu, Masters Thesis, Saga University (1992);
C.L. Kim, Masters Thesis, Korea University (1990);
K.S. Nho, Masters Thesis, Korea University (1991);
J.S. Kim, Masters Thesis, Korea University (1991).

[17] M. Frautschi *et al.*, Nucl. Inst. Meth. A **307**, 52 (1991).

[18] K. Ueno *et al.*, Submitted to Nucl. Inst. Meth.; University of Rochester preprint UR-1050, (1988).

[19] T. Mori, Ph.D. Thesis, Appendix A, University of Rochester, UR-1104, (1988);
Y.H. Ho, Ph.D. Thesis, Appendix B, University of Rochester, UR-1162, (1990).

[20] T. Mori, Ph.D. Thesis, Appendix B, University of Rochester, UR-1104, (1988).

[21] H. Harada *et al.*, Nucl. Inst. Meth. A **265**, 141 (1988);
Y. Fujii *et al.*, Nucl. Inst. Meth. A **283**, 665 (1989).

[22] F. Kajino *et al.*, Nucl. Inst. Meth. A **245**, 507 (1986).

[23] W.R. Nelson *et al.*, SLAC Report No.265 (1985).

[24] Y. Doi *et al.*, Nucl. Inst. Meth. A **274**, 95 (1989).

[25] M. Gyr and C. Iselin, *Poisson Group Programs User's Guide*, CERN (1976).

[26] S.K. Kim, Ph.D. Thesis, Appendix B, Korea University (1988);
H. Asakura *et al.*, Rep. Fac. Sci. Engrg. (Saga University) **16**, 101 (1988).

[27] T. Yasuda, Masters Thesis, Chuo University (1989).

[28] D.G. Cassel and M. Ogg, "DUET – a Track-Finding Program for Cylindrical Geometries", CLEO Internal Report (1983).

[29] Y.K. Kim, Ph.D. thesis Appendix B, Univ. of Rochester, UR-1182, (1990).

[30] J. Fujimoto and Y. Shimizu, Mod. Phys. Lett. A **3**, 581 (1988);
J. Fujimoto, K. Kato, and Y. Shimizu, Prog. Theo. Phys. **79**, 701 (1988).

[31] J.J. Sakurai and D. Schidknecht, Phys. Lett. **40B**, 121 (1972).

[32] T.F. Walsh and P.M. Zerwas, Phys. Lett. **44B**, 195 (1973).

[33] M. Drees and R.H. Godbole, Nucl. Phys. B **339**, 355 (1990);
R. Tanaka *et al.*, AMY collaboration, Phys. Lett. **277B**, 215 (1992).

[34] T. Sjöstrand and M. Bengtsson, CERN-TH-6488-92 (1992);
Comput. Phys. Commun. **43**, 367 (1987).

[35] T. Sjöstrand and M. Bengtsson, Comput. Phys. Commun. **39**, 347 (1986).

[36] G. Altarelli and G. Parisi, Nucl. Phys. B **126**, 298 (1977).

[37] B. Andersson *et al.*, Phys. Rep. **97**, 33 (1983).

[38] Y.K. Li *et al.*, AMY collaboration, Phys. Rev. D **41**, 2675 (1990);
U. K. Yang, M.S. thesis, Korea University (1991).

[39] H. W. Zheng *et al.*, AMY collaboration, Phys. Rev. D **42**, 737 (1990).

[40] H. Fesefeldt, RWTH Aachen Report PITHA 85/02 (1985).

[41] F.F. Field and R.P. Feynmann, Nucl. Phys. B **136**, 1 (1978);
P. Hoyer *et al.*, Nucl. Phys. B **161**, 349 (1979);
A. Ali *et al.*, Phys. Lett. **93B**, 155 (1980).

[42] F.A. Berends *et al.*, Nucl. Phys. B **297**, 429 (1988);
W. Beenakker and W. Hollik, ECFA workshop on LEP 200, CERN 87-09 p.185 (1987);
W. Hollik, DESY preprint 88-188 (1988).

[43] F.A. Berends, R. Kleiss, and S. Jadach, Nucl. Phys. **202**, 63 (1982);
Comput. Phys. Commun. **29**, 185 (1983).

[44] H. Sagawa *et al.*, AMY collaboration, Phys. Rev. Lett. **60**, 93 (1988);
T. Mori *et al.*, AMY collaboration, Phys. Lett. **48B**, 499 (1989);
T. Kumita *et al.*, AMY collaboration, Phys. Rev. D **42**, 1339 (1990).

[45] E.A. Kuraev and V.S. Fadin, Sov. J. Nucl. Phys. **41** 466 (1985);
G. Altarelli and G. Martinelli, CERN 86-02 p47 (1986);
O. Nicrosini and L. Trentadue, Phys. Lett. **196B**, 551 (1987);
V.S. Fadin and V.S. Khoze, Novosibirsk preprint 87-157 (1987).

[46] S. Lusin, Ph.D. Thesis, University of South Carolina (1992).

[47] K. Hikasa *et al.*(Particle Data Group), Phys. Rev. D, **45** Number 11-II (1992).

[48] TOPAZ collaboration, I. Adachi *et al.*, Phys. Lett. **234B**, 525 (1990);
VENUS collaboration, H. Yoshida *et al.*, Phys. Lett. **198B**, 570 (1987);
K. Abe *et al.*, Phys. Lett. **234B**, 382 (1990); Phys. Lett. **246B**, 297 (1990).
PEP and PETRA data are taken from: CELLO collaboration,
H.-J. Behrend *et al.*, Phys. Lett. **183B**, 400 (1987).

[49] HRS collaboration, M. Derrick *et al.*, Phys. Rev. D **31**, 2352 (1985);
MAC collaboration, W.W. Ash *et al.*, Phys. Rev. Lett. **55**, 1831 (1985);
MARK II collaboration, M.E. Levi *et al.*, Phys. Rev. lett. 51, 1941 (1983);
CELLO collaboration, H.J. Behrend *et al.*, Z. Phys. C **14**, 283 (1982);

Phys. Lett. **191B**, 209 (1987);
MARK J collaboration, B. Adeva *et al.*, Phys. Rev. D **38**, 2665 (1988);
JADE collaboration, W. Bartel *et al.*, Z. Phys. C **30**, 371 (1986); S. Hegner *et al.*, Z. Phys. C **46**, 547 (1990);
PLUTO collaboration, Ch. Berger *et al.*, Z. Phys. C **21**, 53 (1983);
TASSO collaboration, W. Braunschweig *et al.*, Z. Phys. C **40**, 163 (1988);
VENUS collaboration, K. Abe *et al.*, Z. Phys. C **48**, 13 (1990); Phys. Lett. **246B**, 297 (1990).
TOPAZ collaboration, B. Howell *et al.*, KEK Preprint 92-49 (1992), submitted to Phys. Lett. B.

[50] HRS collaboration, S. Abachi *et al.*, Phys. Rev. D **40**, 902 (1989);
MAC collaboration, E. Fernandez *et al.*, Phys. Rev. Lett. **54**, 1620 (1985);
MARK II collaboration, M.E. Levi *et al.*, Phys. Rev. lett. **51**, 1941 (1983);
CELLO collaboration, H.J. Behrend *et al.*, Phys. Lett. **222B**, 209 (1989);
MARK J collaboration, B. Adeva *et al.*, Phys. Rev. D **38**, 2665 (1988);
JADE collaboration, W. Bartel *et al.*, Phys. Lett. **161B**, 188 (1985);
S. Hegner *et al.*, Z. Phys. C **46**, 547 (1990);
PLUTO collaboration, Ch. Berger *et al.*, Z. Phys. C **28**, 1 (1985);
TASSO collaboration, M. Althoff *et al.*, Z. Phys. C **26**, 521 (1985);
W. Braunschweig *et al.*, Z. Phys. C **43**, 549 (1989);
VENUS collaboration, K. Abe *et al.*, Z. Phys. C **48**, 13 (1990); Phys. Lett. **246B**, 297 (1990).
TOPAZ collaboration, B. Howell *et al.*, KEK Preprint 92-49 (1992), submitted to Phys. Lett. B.

[51] CDF collaboration, Phys. Rev. D **43**, 2070 (1991); UA2 collaboration, Phys. Lett. **241B**, 150 (1990). The value quoted is the combined value of CDF, $M_W = 79.91 \pm 0.39$ GeV, and UA2,
$M_W = 80.79 \pm 0.31(\text{stat.}) \pm 0.21(\text{sys.}) \pm 0.81(\text{scale})$ GeV.

[52] M.C. Gonzalez-Garcia and J.W.F. Valle, Phys. Lett. **236B**, 360 (1990);
Phys. Rev. D **41**, 2355 (1990); Nucl. Phys. B **345**, 312 (1990).

[53] U. Amaldi *et al.*, Phys. Rev. D **36**, 1385 (1987).

[54] G. Costa *et al.*, Nucl. Phys. B **297**, 244 (1988).

[55] CDF collaboration, F. Abe *et al.*, Phys. Rev. Lett. **68**, 1463 (1992).

[56] Hagiwara *et al.*, Phys. Rev. D **41**, 815 (1990);
VENUS collaboration, K. Abe *et al.*, Phys. Lett. **246B**, 297 (1990).

[57] J.A. Grifols, E. Masso, and T.G. Rizzo, Phys. Rev. D **42**, 3293 (1990).

[58] S.L. Glashow and U. Sarid, Phys. Lett. **246B**, 188 (1990).

[59] R. Foot, O.F. Hernandez, and T.G. Rizzo, Phys. Lett. **261B**, 153 (1991).

[60] UA2 collaboration, J. Alitti *et al.*, Z. Phys. C **49**, 17 (1991).

[61] V. Barger and T. Rizzo, Phys. Rev. D **41** **946** (1990).

[62] H. Cramer, *Mathematical Methods of Statistics*, Princeton Univ. Press, New Jersey (1958);
R.A. Fischer, *Statistical Methods for Research Workers*, 8th edition, Edinburgh and London (1941).

[63] S. Bethke and S. Catani, CERN-TH.6484/92 (1992).

[64] V. Branchina *et al.*, Phys. Rev. Lett. **65**, 3237 (1990).

[65] T.N. Truong, EP-CPTh. A172. 0492 (1992); KEK-Preprint-92-28 (1992).

Appendix A

Summary of Data Used in the Fits

In Appendix A, we present tables of all data on R_{hadron} [48], $R_{\mu\mu}$, $A_{\mu\mu}$ [49], $R_{\tau\tau}$, and $A_{\tau\tau}$ [50], which are used in the fits described in chapters 6 and 7.

For R_{hadron} data, the errors are given as percentage. The systematic errors are split into three categories described in Section 6.1. We have adjusted the published values of R_{hadron} from TOPAZ and VENUS for the effect of the extra diagrams ($\sigma_{QED} \cdot \sigma_{EW}$), the different parameterizations (M_Z, M_t, and M_H), and the consistent treatment of $\epsilon(1+\delta)$ in the radiative corrections.

For the other data on $R_{\mu\mu}$, $R_{\tau\tau}$, $A_{\mu\mu}$, and $A_{\tau\tau}$, a statistical error and a total systematic error are given for each measurement. For measurements for which only total errors are available, we quote them as statistical errors.

Experiment	$\sqrt{s}$ (GeV)	R	σ_{stat} (%)	σ_{ptp} (%)	σ_{norm1} (%)	σ_{norm2} (%)
AMY	50.00	4.60	10.8	2.8	2.5	2.4
	52.00	4.38	4.6	2.2	2.5	2.4
	54.00	4.84	13.0	3.4	2.5	2.4
	55.00	4.62	5.3	1.4	2.5	2.4
	56.00	5.18	3.8	1.1	2.5	2.4
	56.50	5.38	9.1	2.5	2.5	2.4
	57.00	4.96	4.6	1.3	2.5	2.4
	58.00	4.66	1.3	0.2	2.5	1.3
	58.50	5.31	10.7	2.0	2.5	2.4
	59.00	5.41	11.3	2.8	2.5	2.4
	59.05	6.59	12.2	2.6	2.5	2.4
	60.00	5.81	5.0	1.3	2.5	2.4
	60.80	5.53	5.3	1.9	2.5	2.4
	61.40	5.40	4.9	1.4	2.5	2.4
	63.60	5.74	15.8	2.4	2.5	1.3
	64.00	6.11	9.6	1.6	2.5	1.3

Table A.1: Summary of the R_{hadron} data from AMY.

Experiment	$\sqrt{s}$ (GeV)	R	σ_{stat} (%)	σ_{ptp} (%)	σ_{norm1} (%)	σ_{norm2} (%)
TOPAZ	50.00	4.59	13.0	2.3	5.5	0.0
	52.00	4.58	4.6	2.2	5.5	0.0
	54.00	5.02	11.4	3.4	5.5	0.0
	55.00	4.67	5.4	1.4	5.5	0.0
	56.00	5.10	4.3	0.8	5.5	0.0
	56.50	5.14	9.4	2.1	5.5	0.0
	57.00	5.18	4.9	1.1	5.5	0.0
	58.29	5.36	8.2	1.7	5.5	0.0
	59.06	5.76	7.5	2.1	5.5	0.0
	60.00	5.31	5.5	1.3	5.5	0.0
	60.80	5.66	4.9	1.1	5.5	0.0
	61.40	5.86	5.3	1.4	5.5	0.0
VENUS	50.00	4.4	11.4	0.0	3.8	9.6
	52.00	4.7	6.4	0.0	3.8	9.6
	54.00	4.73	9.4	1.8	3.8	0.0
	55.00	4.35	7.0	1.8	3.8	0.0
	56.00	4.68	3.9	1.8	3.8	0.0
	56.50	3.95	10.4	1.8	3.8	0.0
	57.00	5.00	4.4	1.8	3.8	0.0
	58.50	4.92	8.7	1.8	3.8	0.0
	59.00	4.85	9.5	1.8	3.8	0.0
	59.05	6.07	10.7	1.8	3.8	0.0
	60.00	5.27	4.7	1.8	3.8	0.0
	60.80	5.67	4.2	1.8	3.8	0.0
	61.40	4.98	4.2	1.8	3.8	0.0
	63.60	6.09	10.7	1.8	3.8	0.0
	64.00	5.78	7.7	1.8	3.8	0.0

Table A.2: Summary of the R_{hadron} data from TOPAZ and VENUS. Data are adjusted for the radiative corrections.

Experiment	$\sqrt{s}$ (GeV)	R	σ_{stat} (%)	σ_{ptp} (%)	σ_{norm1} (%)	σ_{norm2} (%)
HRS	29.00	4.20	0.8	0.0	7.0	0.0
MAC	29.00	4.00	0.8	0.0	2.1	0.0
CELLO	22.00	3.86	3.0	2.1	1.7	0.0
	33.80	3.74	2.6	1.9	1.7	0.0
	38.28	3.89	2.6	1.7	1.7	0.0
	41.50	4.03	4.1	1.8	1.7	0.0
	43.60	3.97	2.0	1.4	1.7	0.0
	44.20	4.01	2.5	1.2	1.7	0.0
	46.00	4.09	5.1	1.9	1.7	0.0
	46.60	4.20	8.5	1.7	1.7	0.0
JADE	22.00	4.11	3.2	0.0	2.4	0.0
	25.01	4.24	6.8	0.0	2.4	0.0
	27.66	3.85	12.5	0.0	2.4	0.0
	29.93	3.55	11.3	0.0	2.4	0.0
	30.38	3.85	4.9	0.0	2.4	0.0
	31.29	3.84	7.3	0.0	2.4	0.0
	34.89	4.17	2.4	0.0	2.4	0.0
	34.50	3.94	5.1	0.0	2.4	0.0
	35.01	3.94	2.5	0.0	2.4	0.0
	35.45	3.94	4.6	0.0	2.4	0.0
	36.38	3.72	5.7	0.0	2.4	0.0
	40.32	4.07	4.7	0.0	2.4	0.9
	41.18	4.24	5.2	0.0	2.4	0.9
	42.55	4.24	5.2	0.0	2.4	0.9
	43.53	4.05	5.0	0.0	2.4	0.9
	44.41	4.04	5.0	0.0	2.4	0.9
	45.59	4.47	5.0	0.0	2.4	0.9
	46.47	4.11	5.9	0.0	2.4	0.9

Table A.3: Summary of the R_{hadron} data from PEP and PETRA (continued to the next page).

Experiment	$\sqrt{s}$ (GeV)	R	σ_{stat} (%)	σ_{ptp} (%)	σ_{norm1} (%)	σ_{norm2} (%)
MARK J	22.00	3.66	2.2	3.0	2.1	0.0
	25.00	3.89	5.4	3.0	2.1	0.0
	30.60	4.09	3.4	3.0	2.1	0.0
	33.82	3.71	1.6	3.0	2.1	0.0
	34.63	3.74	0.8	3.0	2.1	0.0
	35.11	3.85	1.6	3.0	2.1	0.0
	36.36	3.78	4.0	3.0	2.1	0.0
	37.40	3.97	9.3	3.0	2.1	0.0
	38.30	4.16	2.2	3.0	2.1	0.0
	40.36	3.75	4.0	3.0	2.1	0.0
	41.50	4.32	4.6	3.0	2.1	0.0
	42.50	3.85	5.2	3.0	2.1	0.0
	43.58	3.91	1.5	3.0	2.1	0.0
	44.23	4.14	1.9	3.0	2.1	0.0
	45.48	4.17	4.8	3.0	2.1	0.0
	46.47	4.35	3.9	3.0	2.1	0.0
PLUTO	27.60	4.07	7.1	0.0	6.0	0.0
	30.80	4.11	3.2	0.0	6.0	0.0
TASSO	22.00	3.89	4.4	0.0	3.5	2.0
	25.00	3.72	10.2	0.0	3.5	2.0
	33.00	3.74	7.2	0.0	3.5	2.0
	34.00	4.14	3.1	0.0	3.5	2.0
	35.00	4.23	2.1	0.0	3.5	2.0
	27.50	3.91	8.2	0.0	3.5	2.0
	30.10	3.94	4.6	0.0	3.5	2.0
	31.10	3.67	4.9	0.0	3.5	2.0
	33.20	4.49	6.3	0.0	3.5	2.0
	34.00	4.10	4.9	0.0	3.5	2.0
	35.00	4.04	4.2	0.0	3.5	2.0
	36.10	3.94	4.3	0.0	3.5	2.0
	41.50	4.11	2.9	0.0	3.5	3.0
	44.20	4.28	3.8	0.0	3.5	3.0

Table A.3: (continuing from the previous page)

Experiment	$\sqrt{s}$ (GeV)	$R_{\mu\mu}$	σ_{stat}	σ_{sys}
AMY	52.00	1.11	0.13	0.03
	55.00	0.88	0.13	0.02
	56.00	1.11	0.11	0.02
	56.50	1.70	0.35	0.04
	57.00	1.11	0.14	0.02
	58.73	1.05	0.17	0.02
	60.00	0.99	0.15	0.02
	60.80	1.21	0.17	0.03
	61.40	0.91	0.14	0.02
TOPAZ	57.87	0.979	0.035	0.046
VENUS	50.00	1.78	0.38	0.12
	52.00	1.11	0.14	0.04
	55.00	1.09	0.16	0.05
	56.00	1.06	0.11	0.04
	56.50	1.09	0.28	0.07
	57.00	1.03	0.13	0.04
	58.00	1.00	0.04	0.00
	58.30	1.17	0.22	0.06
	59.06	0.70	0.17	0.04
	60.00	1.04	0.15	0.04
	60.80	1.00	0.17	0.04
	61.40	1.11	0.15	0.05
	63.60	0.93	0.33	0.07
	64.00	1.29	0.27	0.07

Table A.4: Summary of the $R_{\mu\mu}$ data from TRISTAN.

Experiment	$\sqrt{s}$ (GeV)	$R_{\mu\mu}$	σ_{stat}	σ_{sys}
HRS	29.00	0.990	0.017	0.030
MAC	29.00	1.010	0.010	0.030
Mark II	29.00	1.002	0.013	0.016
CELLO	14.00	1.164	0.093	0.059
	22.00	1.000	0.080	0.051
	25.00	0.948	0.273	0.047
	33.30	1.037	0.151	0.052
	34.00	0.860	0.063	0.043
	34.70	1.108	0.215	0.055
	36.40	0.809	0.281	0.040
	38.30	0.970	0.070	0.040
	41.30	1.060	0.170	0.040
	43.60	0.970	0.070	0.040
	44.20	1.010	0.090	0.040
	46.20	0.950	0.220	0.040
JADE	13.90	1.000	0.050	0.050
	22.00	1.020	0.060	0.050
	25.06	1.150	0.170	0.050
	31.55	1.010	0.080	0.050
	33.84	0.970	0.050	0.050
	34.61	0.970	0.020	0.050
	34.89	1.030	0.030	0.050
	35.00	0.984	0.019	0.020
	37.60	1.120	0.120	0.050
	41.28	0.970	0.060	0.050
	44.17	0.980	0.050	0.050
	46.00	1.030	0.090	0.050

Table A.5: Summary of the $R_{\mu\mu}$ data from PEP and PETRA (continued to the next page).

Experiment	$\sqrt{s}$ (GeV)	$R_{\mu\mu}$	σ_{stat}	σ_{sys}
Mark J	14.00	1.040	0.050	0.030
	22.50	1.020	0.050	0.030
	34.60	0.980	0.016	0.030
	35.00	1.000	0.018	0.030
	36.40	1.080	0.130	0.030
	38.30	1.070	0.050	0.030
	40.40	0.930	0.100	0.030
	42.00	1.040	0.090	0.030
	43.80	0.990	0.030	0.030
	46.10	0.960	0.080	0.030
PLUTO	34.70	0.944	0.026	0.040
TASSO	13.90	1.050	0.080	0.
	22.30	1.060	0.090	0.
	34.50	1.002	0.020	0.035
	35.00	0.932	0.018	0.044
	38.30	0.951	0.072	0.060
	43.60	0.921	0.037	0.055

Table A.5: (continuing from the previous page)

Experiment	$\sqrt{s}$ (GeV)	$R_{\tau\tau}$	σ_{stat}	σ_{sys}
AMY	52.00	1.36	0.17	0.04
	55.00	1.15	0.20	0.03
	56.00	1.11	0.14	0.03
	56.50	0.75	0.25	0.02
	57.00	1.27	0.18	0.03
	58.73	1.13	0.22	0.03
	60.00	1.14	0.20	0.03
	60.80	1.35	0.22	0.03
	61.40	1.06	0.18	0.03
TOPAZ	57.87	1.045	0.042	0.046
VENUS	50.00	0.98	0.36	0.07
	52.00	1.24	0.19	0.06
	55.00	1.06	0.21	0.05
	56.00	1.04	0.14	0.04
	56.50	1.59	0.44	0.11
	57.00	0.82	0.16	0.04
	58.00	1.00	0.05	0.00
	58.30	0.67	0.22	0.04
	59.06	1.30	0.30	0.07
	60.00	0.94	0.19	0.04
	60.80	0.98	0.21	0.05
	61.40	1.21	0.20	0.05
	63.60	0.71	0.38	0.06
	64.00	1.19	0.33	0.07

Table A.6: Summary of the $R_{\tau\tau}$ data from TRISTAN.

Experiment	$\sqrt{s}$ (GeV)	$R_{\tau\tau}$	σ_{stat}	σ_{sys}
HRS	29.00	1.044	0.014	0.030
MAC	29.00	0.980	0.010	0.034
Mark II	29.00	0.996	0.016	0.028
CELLO	14.00	1.090	0.070	0.060
	22.00	1.020	0.080	0.040
	34.20	1.030	0.050	0.070
	35.00	0.980	0.020	0.020
	38.10	0.990	0.060	0.040
	41.10	0.970	0.110	0.050
	43.60	0.960	0.050	0.040
	44.20	0.970	0.060	0.040
	46.10	1.170	0.130	0.050
JADE	12.00	1.290	0.240	0.200
	25.60	1.160	0.160	0.110
	30.60	1.060	0.100	0.080
	34.57	0.959	0.019	0.033
	35.00	1.012	0.021	0.023
	43.05	0.980	0.037	0.041
Mark J	14.00	1.130	0.140	0.070
	22.40	1.020	0.120	0.060
	34.70	1.000	0.030	0.050
	39.40	0.980	0.080	0.050
	43.80	0.970	0.060	0.050
	46.10	1.020	0.160	0.050
PLUTO	34.60	0.890	0.050	0.080
TASSO	13.90	1.050	0.140	0.090
	22.30	1.010	0.150	0.090
	34.50	1.030	0.050	0.090
	35.00	1.036	0.050	0.068
	42.40	1.011	0.097	0.079
	43.10	1.05	0.17	0.

Table A.7: Summary of the $R_{\tau\tau}$ data from PEP and PETRA.

Experiment	$\sqrt{s}$ (GeV)	$A_{\mu\mu}$	σ_{stat}	σ_{sys}
AMY	52.00	−0.4652	0.0832	0.0035
	55.00	−0.1494	0.1662	0.0011
	56.00	−0.3907	0.0902	0.0029
	56.50	+0.0345	0.2724	0.0003
	57.00	−0.4030	0.0927	0.0030
	58.73	−0.1769	0.1645	0.0013
	60.00	−0.4476	0.1027	0.0034
	60.80	−0.5213	0.0814	0.0039
	61.40	−0.2172	0.1695	0.0016
TOPAZ	57.87	−0.322	0.031	0.011
VENUS	50.00	−0.345	0.209	0.0
	52.00	−0.291	0.134	0.0
	55.00	−0.359	0.143	0.0
	56.00	−0.308	0.109	0.0
	56.50	−0.443	0.211	0.0
	57.00	−0.121	0.152	0.0
	58.00	−0.290	0.030	0.0
	58.30	−0.163	0.185	0.0
	59.06	−0.667	0.230	0.0
	60.00	−0.238	0.143	0.0
	60.80	−0.077	0.178	0.0
	61.40	−0.350	0.140	0.0
	63.60	−0.090	0.450	0.0
	64.00	+0.110	0.230	0.0

Table A.8: Summary of the $A_{\mu\mu}$ data from TRISTAN.

Experiment	$\sqrt{s}$ (GeV)	$A_{\mu\mu}$	σ_{stat}	σ_{sys}
HRS	29.00	−0.049	0.015	0.005
MAC	29.00	−0.063	0.008	0.002
Mark II	29.00	−0.071	0.017	0.
CELL	34.20	−0.064	0.064	0.
	39.00	−0.048	0.065	0.010
	44.00	−0.188	0.045	0.010
JADE	13.90	+0.027	0.049	0.
	22.00	−0.106	0.064	0.
	34.40	−0.111	0.018	0.010
	35.00	−0.099	0.015	0.005
	38.00	−0.097	0.050	0.010
	43.70	−0.191	0.028	0.010
Mark J	14.00	+0.053	0.050	0.005
	22.50	−0.043	0.061	0.005
	34.80	−0.104	0.013	0.005
	36.40	−0.136	0.135	0.005
	38.30	−0.123	0.053	0.005
	40.40	+0.050	0.105	0.005
	42.00	−0.159	0.093	0.005
	43.80	−0.156	0.030	0.005
	46.10	−0.176	0.083	0.005
PLUTO	34.70	−0.134	0.031	0.010
TASSO	13.90	−0.010	0.060	0.
	22.30	−0.130	0.070	0.
	34.50	−0.091	0.023	0.005
	35.00	−0.106	0.023	0.005
	38.30	+0.017	0.086	0.005
	43.60	−0.176	0.044	0.005

Table A.9: Summary of the $A_{\mu\mu}$ data from PEP and PETRA.

Experiment	$\sqrt{s}$ (GeV)	$A_{\tau\tau}$	σ_{stat}	σ_{sys}
AMY	52.00	−0.179	0.130	0.002
	55.00	−0.108	0.184	0.002
	56.00	−0.263	0.127	0.003
	56.50	−0.917	0.545	0.011
	57.00	−0.562	0.063	0.007
	58.73	−0.113	0.209	0.002
	60.00	−0.517	0.130	0.006
	60.80	+0.029	0.190	0.001
	61.40	−0.411	0.140	0.005
TOPAZ	57.87	−0.339	0.049	0.010
VENUS	50.00	−0.555	0.280	0.0
	52.00	−0.256	0.157	0.0
	55.00	−0.089	0.211	0.0
	56.00	−0.276	0.147	0.0
	56.50	−0.038	0.324	0.0
	57.00	−0.473	0.172	0.0
	58.00	−0.270	0.040	0.0
	58.30	−0.025	0.322	0.0
	59.06	−0.744	0.119	0.0
	60.00	−0.023	0.228	0.0
	60.80	−0.520	0.174	0.0
	61.40	−0.670	0.100	0.0
	63.60	−0.050	0.475	0.0
	64.00	−0.090	0.350	0.0

Table A.10: Summary of the $A_{\tau\tau}$ data from TRISTAN.

Experiment	$\sqrt{s}$ (GeV)	$A_{\tau\tau}$	σ_{stat}	σ_{sys}
HRS	29.00	−0.061	0.023	0.005
MAC	29.00	−0.055	0.012	0.005
Mark II	29.00	−0.042	0.020	0.
CELLO	14.00	+0.100	0.070	0.
	22.00	+0.011	0.078	0.
	34.20	−0.103	0.052	0.
	35.00	−0.070	0.019	0.009
	38.10	−0.118	0.062	0.027
	43.80	−0.163	0.035	0.013
JADE	34.60	−0.067	0.025	0.010
	35.00	−0.081	0.020	0.006
	38.00	+0.068	0.063	0.010
	43.70	−0.177	0.036	0.010
Mark J	34.70	−0.106	0.031	0.015
	43.80	−0.085	0.066	0.015
PLUTO	34.60	−0.059	0.068	0.013
TASSO	34.50	−0.049	0.053	0.013
	35.00	−0.092	0.052	0.010
	42.40	−0.066	0.095	0.010

Table A.11: Summary of the $A_{\tau\tau}$ data from PEP and PETRA.

Appendix B

List of the AMY Collaborators

The AMY Collaboration

A. Bodek,[a] L.M. Chinitz,[a,j] S. Kanda,[a] B.J. Kim,[a] T. Kumita,[a] Y.K. Li,[a] M.L. Olsson,[a] A. Sill,[a] K. Ueno,[a] C. Velissarris,[a] S.K. Kim,[o] A. Bacala,[o,p] M.H. Lee,[o] F. Sannes,[o] S. Schnetzer,[o] R. Stone,[o] J. Vinson,[o] P. Kirk,[b] J. Lim,[b] S.S. Myung,[b] C.P. Cheng,[c] A. Abashian,[d] K. Gotow,[d] K.P. Hu,[d] A.Z. Lai,[d] M.E. Mattson,[d] L. Piilonen,[d] K.L. Sterner,[d] S. Lusin,[e] C. Rosenfeld,[e] A.T.M. Wang,[e] S. Wilson,[e] L.Y. Zheng,[e] M. Frautschi,[f] H. Kagan,[f] R. Kass,[f] C.A. Fry,[g] R.E. Breedon,[h,j] Winston Ko,[h] R.L. Lander,[h] J. Rowe,[h] J.R. Smith,[h] D. Stuart,[h] S.L. Olsen,[i] K. Abe,[j] Y. Fujii,[j] Y. Higashi,[j] Y. Kurihara,[j] F. Liu,[j] A. Maki,[j] T. Nozaki,[j] T. Omori,[j] H. Sagawa,[j] Y. Sakai,[j] T. Sasaki,[j] Y. Sugimoto,[j] Y. Takaiwa,[j] S. Terada,[j] R. Walker,[j,a] F. Kajino,[k] T.L. Thomas,[l] R. Poling,[l] T. Aso,[m] Y. Ishi,[m] K. Miyano,[m] H. Miyata,[m] Y. Yamashita,[n] J.J. Canete,[p] A.J. Devera,[p] S. Kobayashi,[q] A. Murakami,[q] S.K. Sahu,[q] M.E. Zommorodian,[q] J.S. Kang,[r] S.K. Choi,[s] D. Son,[s] S. Matsumoto,[t] R. Tanaka,[t] T. Ishizuka[u]

[a] *University of Rochester, Rochester, NY 14627*
[b] *Louisiana State University, Baton Rouge, LA 70803*
[c] *Institute of High Energy Physics, Beijing 100039*
[d] *Virginia Polytechnic Institute and State University, Blacksburg, VA 24061*
[e] *University of South Carolina, Columbia, SC 29208*
[f] *Ohio State University, Columbus, OH 43210*
[g] *SSC Laboratory, Dallas, TX 75237*
[h] *University of California, Davis, CA 95616*
[i] *University of Hawaii, Honolulu, HI 96822*
[j] *KEK, National Laboratory for High Energy Physics, Ibaraki 305*
[k] *Konan University, Kobe 658*
[l] *University of Minnesota, Minneapolis, MN 55455*
[m] *Niigata University, Niigata 950-21*
[n] *Nihon Dental College, Niigata 951*
[o] *Rutgers University, Piscataway, NJ 08854*
[p] *University of the Philippines, Quezon City, 3004*
[q] *Saga University, Saga 840,* [r] *Korea University, Seoul 136-701*
[s] *Kyungpook National University, Taegu 702-701*
[t] *Chuo University, Tokyo 112*
[u] *Saitama University, Urawa 338*